

ABSTRACT

Title of Dissertation: PLASMA-BASED ATOMIC SCALE
ETCHING APPROACHES USING EITHER
ION OR ELECTRON BEAM ACTIVATION

Kang-Yi Lin, Doctor of Philosophy, 2022

Dissertation directed by: Professor Gottlieb S. Oehrlein, Department of
Physics, Department of Material Science and
Engineering and Institute
for Research in Electronics and Applied Physics

Plasma dry etching has been extensively employed in semiconductor manufacturing processes for anisotropic pattern transfer. With device miniaturization, the conventional approach utilizing continuous wave plasma etching does not meet the requirement for sub-nanometer processing nodes, including profile control and atomic-scale etching selectivity. Additionally, the direct plasma exposure of a substrate raises the concern of plasma damage and undesired material removal. We describe improvements of plasma-based etching techniques and identified novel ways for enabling material removal. We have systematically studied different precursor chemistries for atomic layer etching on etching selectivity of SiO_2 to Si_3N_4 and SiO_2 to Si and obtained an understanding of the surface chemistry evolution. Compared to the conventional approach that mixes fluorocarbon and hydrogen precursors, selected hydrofluorocarbon can deliver optimal plasma chemistry that produces a reduced F/C film in the

deposition step and realizes atomic-scale etching selectivity. We also report a new approach for establishing etching selectivity of HfO_2 over Si by integrating substrate-selective deposition into an atomic layer etching sequence. The optimal precursor chemistry can selectively deposit on the Si surface as a passivation layer and convert HfO_2 to metal-organic compounds for desorption. Finally, we designed and built a system that consists of an electron flood gun and a remote plasma source to demonstrate the concept of a new etching approach by exploiting electron-neutral synergistic effects. This configuration achieves precisely controlled SiO_2 or Si_3N_4 etching by co-introducing an electron beam and Ar/ CF_4 / O_2 remote plasma. This approach also addresses the issue of limited precursor chemistries in electron beam-induced etching.

PLASMA-BASED ATOMIC SCALE ETCHING APPROACHES USING EITHER
ION OR ELECTRON BEAM ACTIVATION

by

Kang-Yi Lin

Dissertation submitted to the Faculty of the Graduate School of the
University of Maryland, College Park, in partial fulfillment
of the requirements for the degree of
Doctor of Philosophy
2022

Advisory Committee:

Professor Gottlieb S. Oehrlein, Chair

Professor John Cumings

Dr. Klaus Edinger

Professor Lourdes G. Salamanca-Riba

Professor Thomas Antonsen

© Copyright by
Kang-Yi Lin
2022

Acknowledgements

Many people helped me get enrolled in the doctoral program at the Department of Materials Science and Engineering, University of Maryland. I would like to start by thanking my co-op mentor at Momentive Performance Materials, Dr. Anand Murugaiah, for inspiring me to pursue an advanced degree and teaching me many valuable research skillsets. Your mentoring made me think of transforming an innovative manufacturing process into intellectual property. I truly enjoyed the time staying at Momentive where I always had your support to explore and validate every possibility of the new ideas.

I would also like to thank my principal investigator at Academia Sinica, Professor Shyue. Without your guideline, I could not understand the material characterization and instrument operation, including SEM, FIB, TEM, XPS, ToF-SIMS, and AFM. Every discussion we had during the commute from National Taiwan University to our office made me understand better what I cannot figure out in a textbook or preventative maintenance. Thank you for offering the possibility to gain theoretical knowledge and practical experience on material characterization instruments.

I would also like to thank my manager at Hitachi High-Tech, Michikazu Morimoto, for educating me on developing a dry etching recipe and interpreting the plasma-surface interaction. Your publication and patent are fascinating training materials. Whenever we discussed these materials, such as pulsed-time modulated plasma technologies, you always brought up the essential concepts and exemplified how to apply them to a real-world etching process. Without your help, I could not participate in the world's leading plasma processing laboratories and research ALE topics.

Thank my advisor, Professor Oehrlein, for helping me become a productive researcher through my doctoral period. Your ideas and insights catalyzed the development of advanced plasma etching technologies. I feel fortunate to join your research lab and learn philosophy you approach and address scientific questions. I also thank you for the opportunity of collaborating with experts in semiconductor companies and presenting our research findings at a prestigious conference.

I would like to thank my dissertation committee for showing interest in my work and taking the time to support my dissertation. I hope this is good reading material before bed. Thank you, Dr. Edinger, Professor Salamanca-Riba, Professor Cumings, and Professor Antonsen.

Also, I would like to thank my collaborators at IBM, TSMC, Global Foundries, Intel, Tokyo Electron Limited, and Carl Zeiss SMT GmbH. The projects were challenging but nicely fitted my research interest for influencing the future development of semiconductor processes. Your fruitful and insightful feedback stimulated me to think of fundamental questions behind the challenges.

Thank you to my former and current colleagues and friends – Dr. Andrew Knoll, Dr. Pingshan Luan, Dr. Chen Li, Dr. Adam Pranda, Thomas Weimar, Nolan Ballew, Yudong Li, Michael Hinshelwood, and David Chung – for your support to complete my research.

Last but not least, I would like to thank my parents, Ching-Rong Lin and Chiou-Chen Huang, and my wife, Dr. Hao Chiang. Mom, thank you for taking the burden of caring for Dad while he experienced a fatal car accident resulting in paralysis. Your support lets me continue pursuing the dream. You always are my role model and encourage me to face every challenge no

matter how difficult life is. I could not complete the graduate program without your support and encouragement.

Table of Contents

Kang-Yi Lin, Doctor of Philosophy, 2022	1
Acknowledgements	ii
Table of Contents	v
List of Tables	viii
List of Figures	ix
Chapter 1: Introduction	1
1.1 Technical Challenges	2
1.2 Collaborative Research	5
1.3 Processing Apparatus	6
1.3.1 Inductively Coupled Plasma Reactor	6
1.3.2 Flood Gun Integrated with Remote Plasma	7
1.4 Characterization Methods	9
1.4.1 <i>In Situ</i> Ellipsometry	9
1.4.2 X-Ray Photoelectron Spectroscopy (XPS)	9
1.5 Processing Materials	9
1.6 Thesis Outlines	10
Chapter 2: Achieving Ultrahigh Etching Selectivity of SiO ₂ over Si ₃ N ₄ and Si in Atomic Layer Etching by Exploiting Chemistry of Complex Hydrofluorocarbon Precursors	12
2.1 Introduction	14
2.2 Experimental	16
2.3 Results	18
2.3.1 SiO ₂ and Si ₃ N ₄ ALE	18
2.3.2 SiO ₂ and Si ALE	29
2.4 Discussion	31
2.5 Summary and Conclusions	32
2.6 Acknowledgments	33
Chapter 3: Selective atomic layer etching of HfO ₂ over silicon by precursor and substrate-dependent selective deposition	34
3.1 Introduction	36

3.2 Technical Motivation Review	38
3.2.1 Achieving Material Etching Selectivity in ALE.	39
3.2.2 Area Selective Deposition	42
3.2.3 Substrate Selective Deposit-Based ALE	44
3.2 Experimental	46
3.3 Results and Discussion	50
3.3.1 Comparison of CH ₄ /C ₄ F ₈ And CH ₄ /CHF ₃ on Si And HfO ₂	50
3.3.1.1 Deposition Behavior	50
3.3.1.2 Model of Non-Selective and Selective Deposition Precursors	56
3.3.2 CH ₄ /CHF ₃ -Based ALE of HfO ₂ with Selectivity to Si	61
3.3.3 Discussion	68
3.4 Summary and Conclusions	75
3.5 Acknowledgments	76
Chapter 4: SiO ₂ Surface Evolution under CF ₄ /O ₂ Remote Plasma and Co-Introduction of Remote Plasma and Electron Beam	77
4.1 Introduction	79
4.2 Experimental	82
4.3 Results and Discussion	85
4.3.1 Remote Plasma on SiO ₂ and Poly-Si	85
4.3.2 Co-introduction of Electron Beam and Remote Plasma for SiO ₂ Etching	87
4.3.3 Prototypical Processing Development	93
4.3.4 Process Characterization	98
EB and Untreated SiO ₂ Interactions	99
Sequential Treatment Consisting of Remote Plasma and Subsequent EB Exposure	104
Co-introduction of Remote Plasma and EB on SiO ₂	109
4.4 Summary and Conclusions	115
4.5 Acknowledgments	117
Chapter 5: Electron beam-induced etching of SiO ₂ , Si ₃ N ₄ , and poly-Si assisted by CF ₄ /O ₂ remote plasma	118
5.1 Introduction	120
5.2 Experimental	121
5.3 Results and Discussion	124

5.3.1 Remote Plasma on SiO ₂ , Si ₃ N ₄ , and Poly-Si	124
5.3.2 Simultaneous Exposure of Surfaces to Electron Beam and Remote Plasma Fluxes for SiO ₂ , Si ₃ N ₄ , and Poly-Si Etching	127
5.3.3 Etching Selectivity Development	135
5.3.4 Process Characterization	138
5.4 Summary and Conclusions	148
5.5 Acknowledgments	149
Chapter 6: Conclusions and Future Work	150
Bibliography	154

List of Tables

Table 1.1 Organization of collaborations in this dissertation

Table 2.1 Molecular formula, name and structure of precursors used in Chapter 2

Table 3.1 Molecular formula, name and structure of precursors used in Chapter 3

List of Figures

Fig. 1.1 Schematic diagram of the reactor for plasma-enhanced atomic layer etching

FIG. 1.2 Schematic diagram of the reactor for studying electron beam-induced etching with the assistance of remote plasma

Fig. 2.2 (Color online) (a) Ellipsometry modeling for SiO₂-Si₃N₄-SiO₂ stack sample with top SiO₂ etching (gold, bottom SiO₂ layer is not shown) and underlayer Si₃N₄ etching (dark red dotted line). The dark cyan dashed line describes the formation of a FC passivation layer with 4 and 7 nm Si₃N₄ loss before etch stop. (b) The experimental *in-situ* ellipsometry data of ALE with C₄F₈, C₄F₈/H₂ and C₃H₃F₃ superimposed on the ellipsometry model. The figure shows various Si₃N₄ losses by using different precursors and essentially negligible Si₃N₄ loss in the case of C₃H₃F₃.

Fig. 2.2 (Color online) (a) SiO₂ and Si₃N₄ layer thickness at the end of each ALE cycle using C₄F₈, C₄F₈/H₂ and C₃H₃F₃, respectively. Si₃N₄ etching stops at various thicknesses. (b) The amount of Si₃N₄ thickness loss before etch stop for three conditions.

Fig. 2.3 (Color online) Si₃N₄ XPS spectra obtained at a take-off angle of 20° that compare surfaces after ALE using (a-c) C₄F₈, (d-f) C₄F₈/H₂ and (g-i) C₃H₃F₃ precursors at the end of deposition and etching steps, respectively. XPS difference spectra formed by subtracting XPS data after the etching step from the data after the deposition step are also shown for the three chemistries (C₄F₈ (black), C₄F₈/H₂ (red) and C₃H₃F₃ (blue)). The spectra include (j) Si2p, (k) C1s and (l) F1s.

Fig. 2.4 (Color online) (a) A comparison of the F/C ratios from the C1s and F1s/C1s spectra with ALE using C₄F₈, C₄F₈/H₂ and C₃H₃F₃ at the end of deposition and etching steps, respectively. (b) The thickness of the HFC film remained on the Si₃N₄ surface at the end of etching step for the three precursors.

Fig. 2.5 (Color online) (a) SiO₂ and Si thicknesses at the end of each ALE cycle using C₄F₈, C₄F₈/H₂ and C₃H₃F₃ precursors. (b) Precursor chemistry dependence of Si thickness loss prior to Si etch stop as the result of formation of a passivation layer.

Fig. 3.1 (Color online) (a) Ion-enhanced etching of amorphous-Si using XeF₂ gas and a 450 eV Ar⁺ beam, from Coburn and Winters. (b) Schematic illustrating a typical ALE sequence that is similar to the concept of the early work published by Coburn and Winters.

Fig. 3.2 (Color online) is a schematic illustrating ODPA SAMs that deactivate the ALD processing on Cu oxide, enabling a dielectric film deposited on SiO₂. The sequential treatment of the acid solution selectively removes the SAMs.

Fig. 3.3 (Color online) the selectivity of AS-ALD is improved by introducing super-cycles of a selective etching step.

Fig. 3.4 (Color online) is a schematic diagram of the atomic layer etching (ALE) cyclic process. The deposition step employs reactant injection and deposition on the substrate followed by a 12 s purge step to remove the residual reactants from the processing chamber. The etching step introduces a substrate bias for ion-assisted chemical etching of the FC deposition film and reacted layer. The experiment was designed to study the deposition behaviors on HfO₂ and Si, so the deposition parameter was set to obtain a 10 Å thick deposition on Si at the end of the injection step in the beginning cycles and apply the same injection amount of the reactant to HfO₂ to observe any differences in the deposition yield.

Fig. 3.5 (Color online) The evolution of the deposition film using the CH₄/C₄F₈ mixture on (a) Si and (b) HfO₂, respectively. Process parameters were selected to yield a 10 Å HFC film thickness on Si during each cycle, where were then applied to HfO₂ to study substrate-dependent deposition.

Fig. 3.6 (Color online) The evolution of deposited HFC film on (a) Si and (b) HfO₂, respectively when using CH₄/CHF₃. Process parameters were selected to yield 10 Å HFC film thickness on Si during the initial cycles and were then applied to HfO₂.

Fig. 3.7 (Color online) (a) A comparison of the deposition thickness at the end of the deposition step on HfO₂ and Si using CH₄/CHF₃ and CH₄/C₄F₈, respectively. (b) Deposition thickness differences between Si and HfO₂ with CH₄/CHF₃ and CH₄/C₄F₈, respectively. (c) The thickness evolution of the deposited FC and HfO₂ film with the selected set of precursors.

Fig.3.8 (Color online) XPS analyses on the HfO₂ and Si films treated by CH₄/C₄F₈ after the purge and etching steps, respectively, in the 4th cycle. The (a) Hf4f, (b) C1s, (c) O1s and (d) F1s spectra present the surface chemistry during each step on HfO₂. In comparison, the (e) Si2p, (f) C1s and (g) F1s spectra show the surface chemistry evolution on Si.

Fig. 3.9 (Color online) XPS analyses on the HfO₂ and Si films treated by CH₄/CHF₃ after the purge and etching steps, respectively, in the 4th cycle. The (a) Hf4f, (b) C1s, (c) O1s and (d) F1s spectra present the surface chemistry during each step on HfO₂. In comparison, the (e) Si2p, (f) C1s and (g) F1s spectra show the surface chemistry evolution on Si.

Fig. 3.10 (Color online) (a) Hf4f, (b) Si2p, (c) C1s, (d) O1s and (e) F1s XPS spectra of the sample (with the film scheme of a 3 nm ALD-HfO₂/5 nm Si/30 nm SiO₂ on a Si substrate) processed by CH₄/CHF₃ after four and eight cycles, respectively.

Fig. 3.11 (Color online) (a) The *in situ* ellipsometry data of Ar/CF₄ etchback on a sample (with a film scheme of 3 nm annealed HfO₂/5 nm Si/30 nm SiO₂ on a Si substrate) and a CH₄/CHF₃-based ALE process with the optimal processing parameters on the identical scheme sample. (b) Ellipsometric modeling of the etching of the top HfO₂ and underlying Si films. The dashed line describes the formation of a FC passivation layer with a corresponding 1.5 nm Si loss before a Si etching stop occurs.

Fig. 3.12 (Color online) (a) HfO₂ and Si thickness at the end of each ALE cycle using a CH₄/CHF₃-based ALE process. (b) The profile of the HfO₂ and FC thickness in the 4th to 6th cycles of the HfO₂ etching region was superimposed on the profile of the FC and Si thickness in the 17th to 21st cycles of the Si etching region.

Fig. 3.13 (Color online) (Color online) XPS spectra comparing a pristine sample with a treated sample by a CH₄/CHF₃-based ALE process after 13 cycles at the end of the HfO₂ etching region (no over-etching). The spectra include (a) Hf4f, (b) Si2p, (c) C1s, (d) O1s and (f) F1s.

Fig. 3.14 (Color online) illustrates the surface reaction using CH₄/CHF₃ and CH₄/C₄F₈, respectively, on HfO₂ and Si, which is consistent with the XPS data shown in Figure 8 and 9. (a) A CH₄/CHF₃ mixture during the deposition step generates a high flux of fluorine, resulting in a

highly fluorinated HfO₂ surface which temporarily suppresses the FC deposition. The following step utilizing low energy Ar⁺ ion bombardment facilitates the etching of fluorinated HfO₂. (b) For Si, a mixture of CH₄/CHF₃ is able to deposit a ~10 Å film due to silicon functioning as a reducing agent to remove excess reactive fluorine. In the etching step, the deposited film buffers Si layers from the ion bombardment, with some H, C, and F remaining on top of the Si. (c) and (d) A CH₄/C₄F₈ mixture deposits a comparable thickness (~10 Å) on both HfO₂ and Si surfaces due to a high flux of FC and HC species carrying a similar reactivity to both materials. In the etching step, low energy Ar⁺ ion bombardment sputters the deposited film and prompts the ion-enhanced fluorination of underlying materials. As a result, a CH₄/CHF₃ mixture on HfO₂ and Si is able to provide a substrate-dependent deposition.

FIG. 4.1. (Color online) Schematic diagram of the concept of co-introduction of radicals and electrons onto a SiO₂ surface to enable a novel etching process.

FIG. 4.2. (Color online) (a) Schematic diagram of the apparatus integrated an electron source and a radical source. Picture of the calibration phosphor screen under (b) a 1000 eV electron beam with the control grid voltage of 100 V and (c) the electron beam and *in situ* ellipsometry laser.

FIG. 4.3. (Color online) The etching rate of SiO₂ and poly-Si using remote plasma with various CF₄/O₂ flow rates.

Fig. 4.4. (Color online) The SiO₂ etch rate as a function of (a) emission current and (b) electron energy.

FIG. 4.5. (Color online) The etching rate of SiO₂ as a function of (a) RF power and (b) CF₄/O₂ flow rate.

FIG. 4.6. (Color online) (a) Schematic diagram of the surface reaction for different exposure conditions. (b) The measured SiO₂ etching rate for these exposures using standard conditions.

FIG. 4.7. (Color online) (a) A two-layer ellipsometric model that describes SiO₂ etching and subsequent electron beam-induced build-up and the experimental result of a procedure consisting of remote plasma and an electron beam. (b) Corresponding thickness change profile of SiO₂ and build-up.

FIG. 4.8. (Color online) (a) *In situ* ellipsometry results after 1000 eV focused electron beam irradiates SiO₂ with the duration of 200 seconds and an ellipsometric model that describes the reduction of SiO₂ thickness. (b) Overall thickness change profile.

FIG. 4.9. (Color online) XPS spectra of (a) O1s and (b) F1s with various EB exposure times on SiO₂.

FIG. 4.10. (Color online) Summary of XPS spectra with various EB exposure times on SiO₂.

FIG. 4.11. (Color online) XPS spectra of using a 20° take-off angle for (a) O1s and (b) F1s photoelectrons and using a 90° take-off angle for (c) O1s and (d) F1s photoelectrons for the procedure of Fig.8(a), respectively.

FIG. 4.12. (Color online) Summary of the characteristic spectra (Si2p, C1s, O1s, and F1s) of SiO₂ in the procedure of Fig. 4.7(c). Two take-off angles are used including (a) 20° and (b) 90°.

FIG. 4.13. (Color online) XPS spectra of SiO₂ at the end of remote plasma and simultaneous remote plasma/EB process for the procedure shown in of Fig. 4.6(b), respectively. The O1s (a) and F1s (b) photoelectron spectra were taken at a 20° take-off angle, whereas the O1s (c) and F1s (d) spectra were taken at a 90° take-off angle.

FIG. 4.14. (Color online) Summary of the characteristic spectra for the procedure shown in Fig. 6(b). Photoelectron take-off angles of (a) 20° and (b) 90° were used.

FIG. 4.15. (Color online) A schematic diagram that describes surface reaction under three different processing modes including (a) EB irradiation on SiO₂, (b) EB irradiation on modified SiO₂, and (c) the co-introduction of electrons and radicals.

FIG. 5.1. (Color online) The etching rate of (a) SiO₂, (b) Si₃N₄, and (c) poly-Si using remote plasma with various relative CF₄/O₂ flow rates and RF powers.

Fig. 5.2. (Color online) The etching rate of (a) SiO₂, (b) Si₃N₄, and (c) poly-Si as a function of electron emission current.

FIG. 5.3. (Color online) The etching rate of SiO₂, Si₃N₄, and poly-Si as a function of electron energy

FIG. 5.4. (Color online) The etch rate of (a) SiO₂, (b) Si₃N₄, and (c) poly-Si as a function of emission current and RF power.

FIG. 5.5. (Color online) The etch rate of (a) SiO₂, (b) Si₃N₄, and (c) poly-Si as a function of emission current and relative CF₄/O₂ flow rate.

FIG. 5.6. (Color online) The etching selectivity of (a) Si₃N₄ to SiO₂ and (b) poly-Si to SiO₂ as a function of emission current and relative CF₄/O₂ flow rate.

FIG. 5.7. (Color online) XPS spectra for treated poly-Si using 20° take-off angle for (a) O1s and (b) F1s photoelectrons and using 90° take-off angle for (c) O1s and (d) F1s photoelectrons. The operating conditions are 20% O₂ remote plasma and 1000 eV focused EB using emission currents of 0 mA, 0.01 mA, and 0.5 mA, respectively.

FIG. 5.8. (Color online) XPS spectra for treated poly-Si of using 20° take-off angle for (a) O1s and (b) F1s photoelectrons and using 90° take-off angle for (c) O1s and (d) F1s photoelectrons. The operating condition is combined remote plasma/EB exposure using a CF₄/80% O₂ remote plasma and 1000 eV focused electrons at emission currents of 0 mA, 0.01 mA, and 0.5 mA, respectively.

FIG. 5.9. (Color online) Integrated O1s and F1s peak areas obtained with poly-Si after combined remote plasma/EB source treatments using various electron emission currents and CF₄/O₂ ratios. Photoelectrons were collected at (a) 20° and (b) 90° take-off angles.

FIG. 5.10. (Color online) Integrated O1s and F1s peak areas obtained with Si₃N₄ after combined remote plasma/EB source treatments using various electron emission currents and CF₄/O₂ ratios. Photoelectrons were collected at (a) 20° and (b) 90° take-off angles.

FIG. 5.11. (Color online) Integrated O1s and F1s peak areas obtained with SiO₂ after combined remote plasma/EB source treatments using various electron emission currents and CF₄/O₂ ratios. Photoelectrons were collected at (a) 20° and (b) 90° take-off angles.

Chapter 1: Introduction

Selective material removal through plasma-surface interactions enables pattern transfer on semiconductor devices. As device scaling shrinks below 10 nm, plasma dry etching needs to achieve atomistic removal with ultra-high etching selectivity. An etching technique realizing atomic-scale layer-by-layer removal called atomic layer etching (ALE) has been extensively developed because of many advantages, including precise etching depth control, simplified processing steps, etching uniformity, and potentially ultra-high materials etching selectivity. Plasma-enhanced ALE typically consists of two steps: surface modification and etching. The surface modification step uses dissociated species to tailor the surface of a substrate; the sequential etching step introduces low-energy ions that sputter and remove the modified layer. Once all modified layers are depleted, the etching stops and it is known as self-limited etching. By iterating these two steps, the etch depth is determined by the number of process cycles.

Etching selectivity can be achieved utilizing the chemical affinity between the constituent of the precursor and substrate. For ALE of Si with selectivity to SiO₂, the surface modification step uses gaseous Cl₂ that only chlorinates Si but not SiO₂, since the energy of chlorinating Si (-159 kJ/mol) is lower than SiO₂ (230 kJ/mol).¹ In the etching step, the Ar⁺ ions have enough kinetic energy to sputter away the chlorinated Si, but not SiO₂ and untreated Si. A cycle consisting of a Cl₂ injection step and then an Ar⁺ ion bombardment step realizes ALE of Si with selectivity to SiO₂.²⁻⁴ However, the use of chlorine cannot meet a process that requires the reverse etching selectivity, i.e. SiO₂ over Si. To accomplish such etching selectivity, it is important to leverage the plasma and surface interactions for identifying a precursor that favors functionalizing SiO₂ but simultaneously passivates poly-Si. Fluorocarbon (FC)-based ALE of

SiO₂ with selectivity to Si has been studied using the feature that SiO₂ consumes FC faster than Si under a certain condition.⁵⁻⁸ C₄F₈ precursor was used in the surface modification step to form a FC layer on both SiO₂ and Si, and sequentially 30 eV Ar⁺ ions were used in the etching step. The etching selectivity is achieved by optimizing the ratio between the FC deposition thicknesses and etching step length (ESL) to the condition where the FC film is fully depleted by SiO₂ while some remain on Si. As more processing cycles have proceeded, the build-up FC on Si is thick enough as a passivation layer to prevent the underlying Si loss from ion bombardment; SiO₂ meanwhile keeps a constant ER. This manner also applies to other applications, e.g. those requiring etching selectivity of SiO₂ over Si₃N₄ and SiGe.

1.1 Technical Challenges

In plasma etching, the step of introducing reactants and ions on a substrate in a continuous wave (CW) process is different from an ALE sequence. A CW process co-introduces reactants and ions to a substrate for maximizing ER through the synergistic effect, whereas an ALE process introduces reactants and ions in separate steps to optimize etching selectivity. To improve the etching selectivity in a CW process, a mixture of etchants and additives is often employed. For example, C₄F₈ mixed with H₂ is used to reduce the fluorine to carbon ratio in the deposited film by hydrogen scavenging fluorine atoms.^{9, 10} As a result, H₂ additives in a C₄F₈ plasma promote a higher etching selectivity of SiO₂ over Si. A combination of etchants and additives is well developed to establish an etching selectivity of different materials.¹¹ However, limited studies have evaluated the effect of mixed reactants in an ALE sequence, especially whether the knowledge of additives in the CW process for enhancing etching selectivity applies

to an ALE sequence. The characteristic of precursors, including the structure and composition, in an ALE sequence also needs further investigation for etching performance.¹²

With device miniaturization, processing materials are no longer limited to Si-based materials. New emerging materials, including metal oxides, are implemented for less leakage current.¹³ For example, a high dielectric (high-*k*) material HfO₂ replaces a SiO₂ gate dielectric to reduce the tunneling effect. Only a few studies have discussed ALE of metal oxides with selectivity to Si-based materials.^{12, 14-16} There raises a need to study the surface reaction between emerging materials and precursors for improving etching selectivity, such as HfO₂ over Si. The above-mentioned ALE approaches, including Cl₂ and FC, do not apply to HfO₂, because the bonding strength of Si-Si (327 kJ/mol) is weaker than of Hf-O (791 kJ/mol).¹ Chlorine or fluorine-based precursors tend to break the Si-Si bond rather than the Hf-O bond, resulting in the volatility of Si products that is much higher than Hf products. The boiling point of SiF₄, SiCl₄, HfF₄, and HfCl₄ at atmospheric pressure is -86 °C, 58 °C, N/A, and 432 °C, respectively.^{17, 18} These lead to a higher ER on Si than HfO₂, so we need to develop a novel ALE approach that can reverse the etching selectivity.

Direct plasma exposure of a substrate often raises the concern of plasma damage. Plasma inherently creates a sheath potential on a substrate, where ions constantly impinge the surface. Ion bombardment produces material defects and undesired removal. Ar plasma, for example, under a 10 mTorr pressure can form a self-bias to -15 V that may lead to etching of Si and SiO₂, especially during a surface modification step in the FC-based ALE sequences.^{7, 8} Therefore, it is crucial to develop a new etching method that eliminates plasma damage.

Electron beam-induced etching (EBIE) shows promising results to eliminate plasma-induced damage because the mass of electrons is orders of magnitude smaller than the mass of ions. EBIE is based on electron beam (EB) irradiation of the surface that has physically or chemically adsorbed chemical etchants to promote electron-stimulated desorption (ESD).¹⁹ However, the combination of precursor chemistries available to functionalize materials in EBIE is still limited as compared to the number of available etchants in plasma etching. Two limiting factors are considered, 1) few precursors can adsorb and cover the substrate surface,²⁰ and 2) the adsorbates can form volatile etch products under EB irradiation.²¹⁻²³ To expand the available precursor chemistries in EBIE, we will leverage a new concept that integrates a remote plasma with an EB source: a remote plasma is used to selectively functionalize the surface of a substrate, and an EB is used to stimulate the removal of the modified layer.

A remote plasma source comprises a plasma source and a neutralization plate. Plasma is used to energize the admitted gas precursors for the production of ions, radicals, and neutrals through electron-gas collision. A neutralization plate at the outlet of a plasma source is used to filter ions and allow only radicals and neutrals to diffuse to the reactor for functionalization of the specimen surface. Different from the conventional EBIE approach that relies on the inherent adsorption of gas-phase precursors on the substrate surface, the advantage of exploiting remote plasma is able to efficiently excite the precursor gases, which greatly increases the probability of radicals and neutrals adsorbed on the substrate surface. Remote plasma, additionally, can be used to functionalize the surface of a specimen. CF_4/O_2 remote plasma, for example, with an O_2 -rich recipe can produce an oxyfluoride layer on Si-based materials. This new experimental configuration consists of an electron flood gun and a remote plasma source and is used to

develop a remote plasma-assisted and EB-activated etching approach for the realization of damage-free pattern transfer.

1.2 Collaborative Research

This research collaborated with several groups of experts in the world’s leading semiconductor companies. A brief description is listed in Table 1.1.

Table 1.1: Organization of collaborations in this dissertation

Project Collaborator	Member	Project
Taiwan Semiconductor Manufacturing Company	H.C. Chen	Atomic layer etching of dielectric materials with high selectivity
Tokyo Electron Limited	H. Cottle	
Intel	J. Tan	
IBM	D. Metzler, S. Engelmann, R. Bruce, E.A. Joseph	
GLOBALFOUNDRIES	C. Labelle, C. Park	
Carl Zeiss, SMS GmbH	C. Preischl, C. F. Hermanns, D. Rhinow, H.-M. Solowan, T. Hofmann, B Michael, K. Edinger	Electron beam-induced process with the assistance of remote plasma

Working with industrial collaborators provides several benefits. The collaborators have excellent experiences that guide research direction. We held monthly phone conferences to discuss the research progress and challenge. Their strategy and professional feedback maximized the importance of research outcomes. Several special wafers, including stacked thin film structures, were prepared by the collaborators to ensure the highest research quality.

1.3 Processing Apparatus

1.3.1 Inductively Coupled Plasma Reactor

The plasma-enhanced ALE experiments were conducted in an inductively coupled plasma (ICP) reactor (Fig. 1.1). The reactor consists of a spiral antenna on a quartz dielectric that is located 13 cm above an electrode. The top antenna is operated at a radiofrequency (RF) of 13.56 MHz to generate plasma, whereas the substrate bias is operated at an RF of 3.7 MHz to control the ion energy of the plasma. The substrate backside was cooled using a chuck held at a temperature of 10 °C to mitigate any thermal effects on the samples. Mass flow controllers (MFCs) were used to precisely control the flow rate of precursors into the reactor. For plasma-enhanced ALE processes, a computer-controlled gas injection system was used to introduce precursors into the chamber at specified intervals.

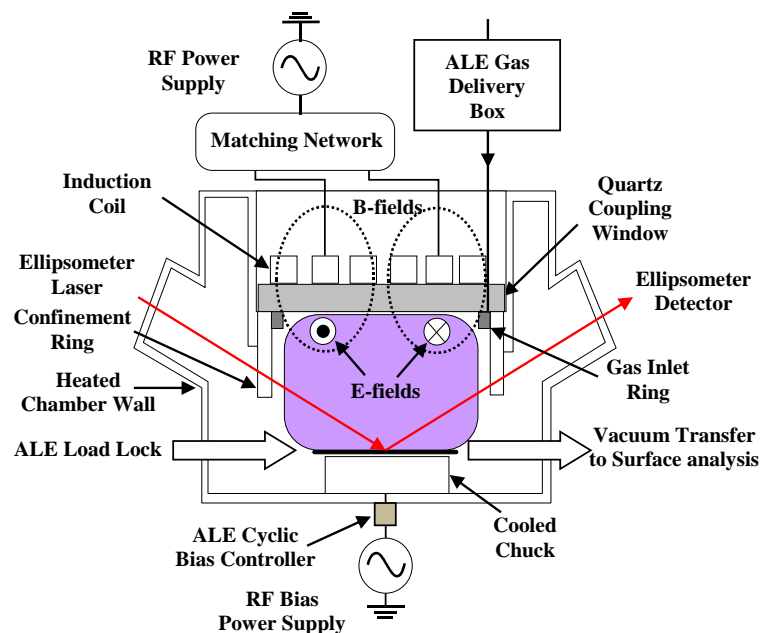


Fig. 1.1. Schematic diagram of the reactor for plasma-enhanced atomic layer etching

1.3.2 Flood Gun Integrated with Remote Plasma

The experiments for electron beam-induced etching (EBIE) with the assistance of remote plasma were performed in a reactor equipped with an electron flood gun that is located 38.3 mm above the sample and a remote plasma source that is installed at the side port of the reactor (Fig. 1.2). The gun provides landing energy of electrons that ranges from 5 eV to 1000 eV with a maximum emission current of 1.5 mA. The grid voltage of the flood gun is used to control the beam spot size. 1000 eV EB with the maximum grid voltage of 100 V produces a ~5.5 mm diameter beam on a substrate. The remote plasma source consists of an electron cyclotron wave resonance (ECWR) at a radiofrequency (RF) of 13.56 MHz. The ECWR effect requires an additional static transverse magnetic field, exploiting the interaction of an electromagnetic field with plasma.²⁴ The magnetic field splits a linearly polarized wave into a left hand and a right hand circularly polarized wave. The right hand circularly polarized wave can propagate in a frequency range between the electron cyclotron frequency and the plasma frequency. This frequency window allows the RF source power to efficiently deposit energy into the plasma and enable the formation of a higher plasma density than in a capacitively coupled plasma. A quartz plate at the outlet of the plasma source is used as a neutralization plate to prevent plasma-generated ions from reaching the sample, only allowing neutrals to diffuse to the reactor.

The operation of the electron flood gun used is not compatible with the pressure of a remote plasma source. The flood gun during operation heats the filament to a temperature of 1800 K or higher to emit electrons and requires a vacuum level of at least 1×10^{-5} Torr to avoid filament burnout. Remote plasma operates in a low-end mTorr pressure range to introduce reactive neutrals to the reactor. The direct assembly of an electron flood gun and a remote

plasma source leads to an engineering concern where the reactive neutrals from remote plasma greatly erode the filament of the flood gun with the suppression of emission current. To prolong the lifetime of the electron flood gun, a differential pumping unit (DPU) with a pressure-limited aperture (PLA) was designed and installed onto the top flange of the reactor. The purpose of the DPU separates the flood gun from the reactor and pumps out gases near the filament through an exclusive pump, whereas the PLA limits the number of gases transported into the DPU. The assembly of the DPU and PLA provides a pressure ratio between the reactor (1×10^{-3} Torr) and the flood gun chamber (1×10^{-6} Torr) of about 1000. The sample holder regulates specimen bias and temperature. Most experiments did not apply substrate bias. The substrate temperature keeps at a temperature of 10°C to mitigate any thermal effect on the samples. Mass flow controllers (MFCs) were used to control the flow rate of precursors into the remote plasma source.

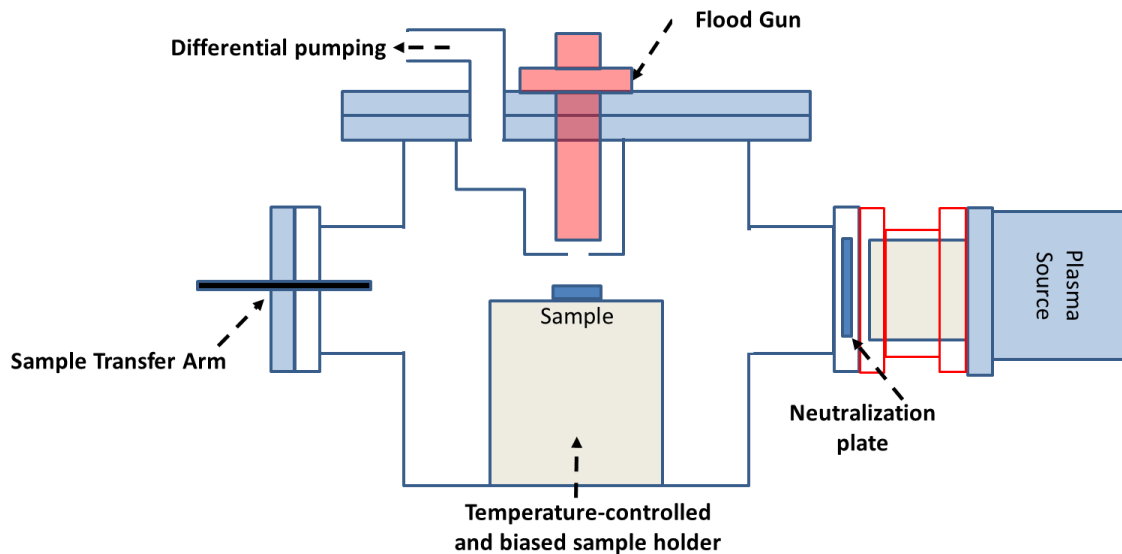


Fig. 1.2. Schematic diagram of the reactor for studying electron beam-induced etching with the assistance of remote plasma

1.4 Characterization Methods

1.4.1 *In Situ* Ellipsometry

In situ ellipsometry was used to collect psi and delta values with a sampling rate of 5 Hz, for evaluating surface modification and etching during a processing step. The wavelength of the ellipsometry laser is 632.8 nm (He-Ne laser). Applying an ellipsometric model to the collected data allows for interpreting the surface modification and calculating the thickness change rate, including etching rate (ER) and deposition rate.

1.4.2 X-Ray Photoelectron Spectroscopy (XPS)

A Vacuum Generators ESCA Mark II surface analysis chamber with a non-monochromatic Al K α X-ray source (1486.6 eV) was used to analyze the surface chemistry of the processed material. The analysis was operated in a constant-energy analyzer mode with a 20 eV pass energy. Two emission angles at 20° and 90° were used to probe the surface and near-surface regions to differentiate the compositional variation with probe depth. The diameter of the analysis area was kept at 5-6 mm. The processed materials were delivered to XPS analysis through a vacuum transfer system to prevent any atmosphere contamination.

1.5 Processing Materials

Thin material films on a Si substrate were used to evaluate the material ER or reactant deposition rate. The film material included Si₃N₄, poly-Si, SiO₂, SiGe, and HfO₂. Multilayer stacked samples were used to study etching selectivity. A SiO₂-Si stack on a Si substrate can

enable the evaluation of etching selectivity of SiO_2 over Si , where the same approach also applies to the SiO_2 - Si_3N_4 , SiO_2 - SiGe , and HfO_2 - Si stacks.

1.6 Thesis Outlines

This work is to explore the reaction mechanism of utilizing complex plasma chemistries for surface modification, so ions or electrons facilitate material desorption. These findings benefit the development of advanced plasma etching methods to address the technical challenges.

In Chapter 2, we investigated the effect of FCs, HFCs, and a mixture of FCs and H_2 in an ALE process toward the etching selectivity of SiO_2 over Si_3N_4 and SiO_2 over poly-Si, respectively. We show that the conventional approach using a mixture of precursors does not improve ALE performance but seriously degrades the etching selectivity. Selecting optimal precursor chemistry that directly functionalizes the surface property enables atomic-scale etching selectivity.

In Chapter 3, we evaluated an approach that integrates substrate-selective deposition into an ALE sequence as a new approach of selective removal. The collected data show that the deposition yield is strongly related to the chemical affinity between the constituents of the precursors and substrate materials. Exploiting this feature facilitates the formation of a passivation layer on Si and the fluorination in HfO_2 , so a sequential etching step can enhance material removal and establish etching selectivity of HfO_2 over Si .

Chapter 4 focuses on an electron beam that activates SiO_2 removal on the area tailored by $\text{Ar}/\text{CF}_4/\text{O}_2$ remote plasma. The previous two chapters discussed the ion-driven material removal

in a plasma reactor where the sheath potential causes material defects. The electron-neutral synergistic effect has been studied on SiO_2 to understand the etching mechanism by differentiating the effect of electrons and neutrals.

Chapter 5 investigated the new experimental configuration that consists of a remote plasma source and an electron flood gun for EBIE of SiO_2 , Si_3N_4 , and poly-Si with the assistance of Ar/ CF_4 / O_2 precursors. A study of the processing parameters of the remote plasma and EB sources on the etching result allowed us to explore a processing window to enable selective material removal, including Si_3N_4 over SiO_2 and poly-Si over SiO_2 .

Chapter 6 summarizes the main findings and discusses future development.

Chapter 2: Achieving Ultrahigh Etching Selectivity of SiO₂ over Si₃N₄ and Si in Atomic Layer Etching by Exploiting Chemistry of Complex Hydrofluorocarbon Precursors

Journal of Vacuum Science & Technology A 36, 040601 (2018)

K. Y. Lin, C. Li, S. Engelmann, R. L. Bruce, E. A. Joseph, D. Metzler, and G. S. Oehrlein

K.Y. Lin contributed to the design and conduction of the research, to the analysis of the experimental results, and to the writing of the manuscript.

All authors discussed the results, commented on and made changes to the manuscript.

ABSTRACT

We demonstrate that complex hydrofluorocarbon (HFC) precursors offer significant advantages relative to gas mixtures of comparable elemental ratios for plasma-based selective atomic layer etching (ALE). This work compares mixtures of a fluorocarbon (FC) precursor and H₂ with a HFC precursor, i.e. mixtures of octafluorocyclobutane (C₄F₈) with H₂ and 3,3,3-trifluoropropene (C₃H₃F₃), for SiO₂ ALE and etching of SiO₂ selective to Si₃N₄ or Si. For continuous plasma etching, process gas mixtures, e.g. C₄F₈/H₂, have been employed and enable highly selective material removal based on reduction of the fluorine content of deposited steady-state HFC films; however this approach is not successful for ALE since hydrogen-induced

etching reduces the thickness of the ultra-thin HFC passivation layer which is required for both etching of SiO_2 and passivation of the Si_3N_4 and Si underlayers, leading to lower materials etching selectivity. Conversely, our results show that $\text{C}_3\text{H}_3\text{F}_3$ -based ALE enables ultra-high ALE selectivity of SiO_2 over Si_3N_4 and Si. The hydrogen in the precursor structure allows to reduce the fluorine content of the deposited HFC film without suppressing the formation of the passivation layer on the surface. Gas pulsing of complex reactive precursors in ALE provides the prospect of utilizing the precursor chemical structure for achieving high materials selectivity in ALE.

2.1 Introduction

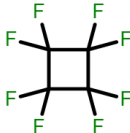
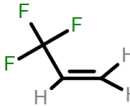
The development of atomic layer etching (ALE) approaches has many promising performance characteristics, including simple process steps, self-limited etching, improved uniformity, and potentially ultra-high materials selectivity required for advanced semiconductor manufacturing.^{25,12} Previously, we pointed out that utilization of the chemical nature of precursors may have significantly greater potential for ALE than conventional steady-state plasma etching, enabling greater control over surface reactions.¹² Manipulating the chemical nature of precursors in an ALE process may open up a novel processing margin for Angstrom-level etch controllability not yet attainable.

The interaction between plasma dissociated reactive gas and substrate significantly affects etching results, including etching selectivity and pattern transfer fidelity. In continuous wave (CW) plasma, the effect of leveraging the chemical structure of the precursor has comparable results as the effect of the precursor mixture. Li *et al* showed that the correlation between the CF₂ fraction in the precursor gas and in the deposited film surface chemistry is less than the correlation between the CF₂ fraction in the precursor gas and in the plasma gas phase obtained from optical emission spectroscopy (OES).²⁶ Other studies also show that the effect of leveraging the content or molecular structure in hydrofluorocarbon (HFC) precursor is similar to the effect of fluorocarbon (FC) precursor gas mixing with hydrogen additives.^{27, 28} The recent publications in the FC-assisted ALE by Metzler *et al*^{5, 7, 8, 29}, using C₄F₈ and CHF₃ on SiO₂ and Si etching, and Li *et al*³⁰, using C₄F₈ and CHF₃ on Si₃N₄ etching, demonstrates that the chemical structure of a precursor has a profound influence on the fluorine and carbon content deposited on the surface. The CHF₃-based ALE resulted in a higher fluorination level on the Si₃N₄ surface

than C_4F_8 , which is different from the observations in CW plasma.³⁰ CH_3F -based ALE of Si_3N_4 has been investigated and established ALE selectivity of Si_3N_4 over Si.^{31, 32} However, to our best knowledge, the study of comparing a HFC precursor to a FC precursor mixed with H_2 in ALE has not been explored as yet.

This article compares the ALE selectivity of SiO_2 over Si_3N_4 and SiO_2 over Si using a) a FC precursor, C_4F_8 , b) a mixture of a FC precursor and H_2 , C_4F_8/H_2 , and c) a HFC precursor, $C_3H_3F_3$. The detailed information regarding the chemical structure of the precursors used for this study is shown in Table 2.1. The experimental tests targeted ALE selectivity of SiO_2 over Si_3N_4 and SiO_2 over Si.^{7, 30} The precursor deposited film thickness per cycle is designed to be thick enough to form a passivating layer on Si_3N_4 or Si, whereas the relatively higher carbon consumption rate of SiO_2 leads to negligible film thickness on SiO_2 .^{33, 34} Stacked SiO_2 - Si_3N_4 - SiO_2 and SiO_2 -Si- SiO_2 on Si substrates were used. The material thickness loss after fully etching the top SiO_2 layer before forming a passivation layer and stopping etch was used to evaluate the ALE selectivity for different precursors. The first part discusses the ALE behavior of SiO_2 and Si_3N_4 and the corresponding Si_3N_4 thickness loss before the formation of an etch-stopping FC passivation layer. To study the correlation between the chemical structure of the precursor and the surface chemistry evolution, X-ray photoelectron spectroscopy (XPS) analysis of the materials at the end of two ALE process steps in one cycle, i.e. the FC deposition step and the etching step, was performed.^{5, 8} In the second part, SiO_2 and Si etching were studied using an identical set of precursors and Si thickness loss before etch stop was determined.

Table 2.2 Molecular formula, name and structure of precursors used in this work.

Molecular Formula	Name	Structure
C ₄ F ₈	Octafluorocyclobutane	
C ₃ H ₃ F ₃	3,3,3-trifluoropropene	

2.2 Experimental

The experimental setup closely matches our previous publications^{8,30} and is briefly described here. We used an inductively coupled plasma (ICP) reactor excited at 13.56 MHz. The substrate was biased at the radiofrequency (RF) of 3.7 MHz. The plasma was confined within a 195 mm diameter anodized Al confinement ring. A 125 mm diameter Si substrate was located 150 mm below the top electrode on an electrostatic chuck. The base pressure before processing was in the 1×10^{-7} Torr range, and the temperature of the 25×25 mm² sample was stabilized by a cooled chuck at 10 °C during plasma processing. A load lock and vacuum transfer were used for all experiments in order to minimize environmental impacts during the sample exchange. The detailed configuration of the plasma system can be found in references 15 and 16.^{35,36} Before each experiment, an O₂ plasma based cleaning process and Ar plasma based conditioning process were employed to ensure that the condition of the reaction chamber remained consistent.³⁷ Two sets of multi-layer stacked samples: a) SiO₂-Si-SiO₂ and b) SiO₂-Si₃N₄-SiO₂ deposited on a Si substrate enabled evaluation of etching selectivity of SiO₂ over Si and SiO₂ over Si₃N₄. The *in-*

situ ellipsometry with a He-Ne laser on the ICP reactor allowed for studying material thickness changes in real time.³⁸

The ALE experiments were performed following the FC-assisted ALE procedure that is based on the use of a steady-state Ar plasma in conjunction with periodic injections of a defined number of precursor gases and synchronized plasma based Ar ion bombardment. The process sequence is similar to our previous work.^{7,30} All plasma processes presented in this work operate with a source power of 200 W and a processing pressure of 10 mTorr along with a 50 sccm Ar carrier gas flow rate. The ALE process is comprised of a deposition step and an etching step. In the deposition step, a selected precursor was introduced with an injection length of 2 seconds to deposit a 10 Å thick FC film on the substrate. This step was followed by a 12 second purge step to pump out the residual reactive gas. In the etching step, a -15 V RF bias voltage was employed with an etching step length (ESL) of 18 seconds, accelerating energetic Ar ions with a maximum kinetic energy of 30 eV to sputter the deposited FC film and reacted layer. Since the deposition yield may be different for each material, the experiment was set to deposit a 10 Å thick FC film on SiO₂ at the beginning cycles and keep a fixed amount of precursor injection during the following cycles. Three sets of precursor were explored, i.e. a) 2 sccm C₄F₈, b) 2 sccm C₄F₈ mixing with 3 sccm H₂ and c) 2 sccm C₃H₃F₃.

To establish surface chemistry modification with regard to precursor chemistry and structure, XPS analyses have been performed at the end of the deposition and etching steps. The samples were transferred under vacuum to a Vacuum Generators ESCALAB MK II surface analysis system for XPS measurements. High resolution scans of the Si2p, C1s, O1s, N1s and F1s spectra were obtained at 20 eV pass energy at an electron take-off angle of 20° (shallow

probing depth $\approx 20\text{-}30 \text{ \AA}$) and 90° (deep probing depth $\approx 80 \text{ \AA}$) with respect to the sample surface. The spectra were calibrated by the binding energy position of the C-C peak to 284.5 eV and fitted using a least square fitting after Shirley background subtraction.^{39, 40}

2.3 Results

2.3.1 SiO₂ and Si₃N₄ ALE

An *in-situ* ellipsometry model in the Delta-Psi space was formulated to simulate the top SiO₂ and Si₃N₄ etching with corresponding accumulated FC film on the surface. This is shown in Figure 2.1(a). The gold solid arrow describes top SiO₂ etching, and the dark red dotted line describes etching of the Si₃N₄ underlayer. The process condition is designed for etching top SiO₂ followed by etch stop on Si₃N₄ by formation of a FC passivation layer on the surface. The dark cyan dashed lines in Figure 2.1(a) simulate the formation of the FC film with a given Si₃N₄ loss, such as 4 and 7 nm, which is used for evaluating the ALE selectivity.

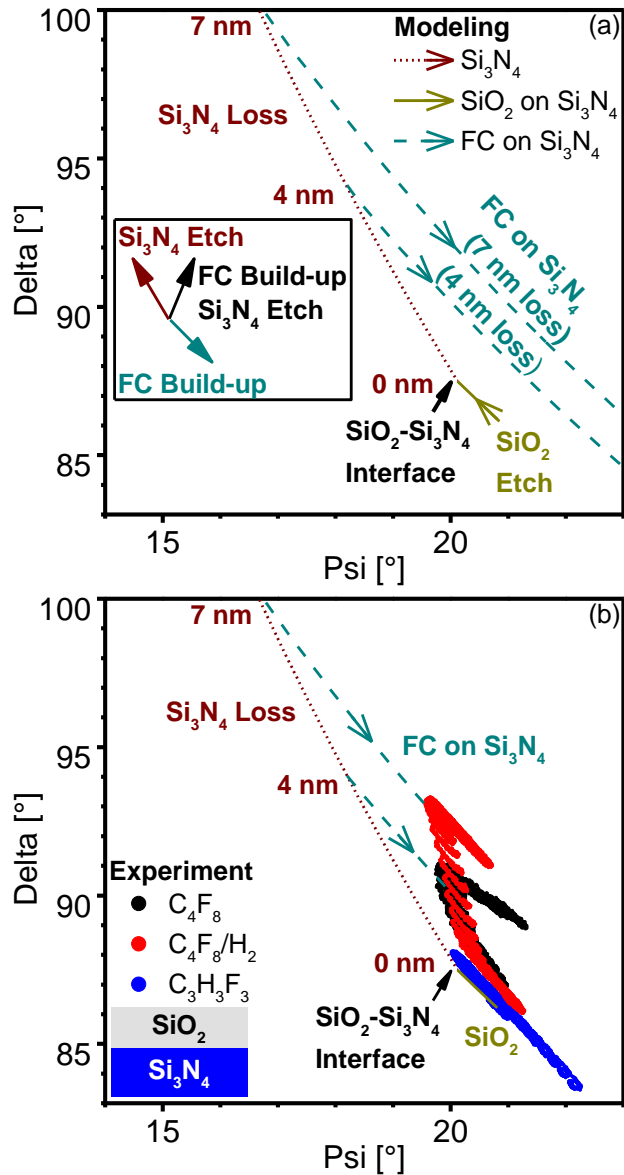


FIG. 2.1. (Color online) (a) Ellipsometry modeling for SiO₂-Si₃N₄-SiO₂ stack sample with top SiO₂ etching (gold, bottom SiO₂ layer is not shown) and underlayer Si₃N₄ etching (dark red dotted line). The dark cyan dashed line describes the formation of a FC passivation layer with 4 and 7 nm Si₃N₄ loss before etch stop. (b) The experimental *in-situ* ellipsometry data of ALE with C₄F₈, C₄F₈/H₂ and C₃H₃F₃ superimposed on the ellipsometry model. The figure shows various

Si₃N₄ losses by using different precursors and essentially negligible Si₃N₄ loss in the case of C₃H₃F₃.

The *in-situ* ellipsometry data of ALE using C₄F₈, C₄F₈/H₂ and C₃H₃F₃ of SiO₂-Si₃N₄-SiO₂ stack sample were superimposed on the modeling results (Figure 2.1(b)). The ALE process conditions were the same as described in the beginning of this section, i.e. ~10 Å FC deposition thickness per cycle on SiO₂, 18 second ESL, and -15 V RF bias voltage that creates Ar ions with a maximum energy of 30 eV. The black dots describe the C₄F₈-based ALE that removes the top SiO₂ layer and gradually accumulates a FC film during the Si₃N₄ etching region. Etching of Si₃N₄ stops once the accumulated film is thick enough to prevent further erosion of the Si₃N₄ underlayer. The corresponding Si₃N₄ loss is used to represent ALE selectivity using C₄F₈. The C₄F₈/H₂ ALE data (red dots) show that the top SiO₂ layer is also completely removed and a FC passivation layer forms with more Si₃N₄ consumption in comparison to C₄F₈ ALE. On the other hand, C₃H₃F₃-based ALE (blue dots) shows a quick formation of a FC passivation layer with negligible Si₃N₄ thickness loss after top SiO₂ etching. Each of these three precursors enabled continuous ALE of SiO₂ and accumulated FC passivation on the Si₃N₄ surface that prevents further Si₃N₄ loss.

The SiO₂ and Si₃N₄ layer thickness at the end of each cycle using C₄F₈, C₄F₈/H₂ and C₃H₃F₃ ALE is shown in Figure 2.2(a). The ellipsometry model shown in Figure 2.1(a) was applied to fit the experimental *in-situ* ellipsometry data and measure the SiO₂ and Si₃N₄ thickness change. For SiO₂ etching, C₄F₈ and C₄F₈/H₂-based ALE gave higher SiO₂ thickness etched per cycle (EPC) than C₃H₃F₃. Si₃N₄ EPC showed a strong dependence on the gaseous

precursor used for ALE. C_4F_8 mixing with H_2 exhibited the highest Si_3N_4 EPC, followed by C_4F_8 and $C_3H_3F_3$. The use of a $C_3H_3F_3$ -based ALE process shows minimum Si_3N_4 loss by rapid formation of a FC passivation layer, whereas the C_4F_8/H_2 mixture using identical process condition increases Si_3N_4 material loss. A comparison of the amounts of net Si_3N_4 loss for C_4F_8 , C_4F_8/H_2 and $C_3H_3F_3$ -based ALE at the end of the 28th cycle, when $C_3H_3F_3$ -based ALE obtained a full etch stop, is shown in Figure 2.2(b).

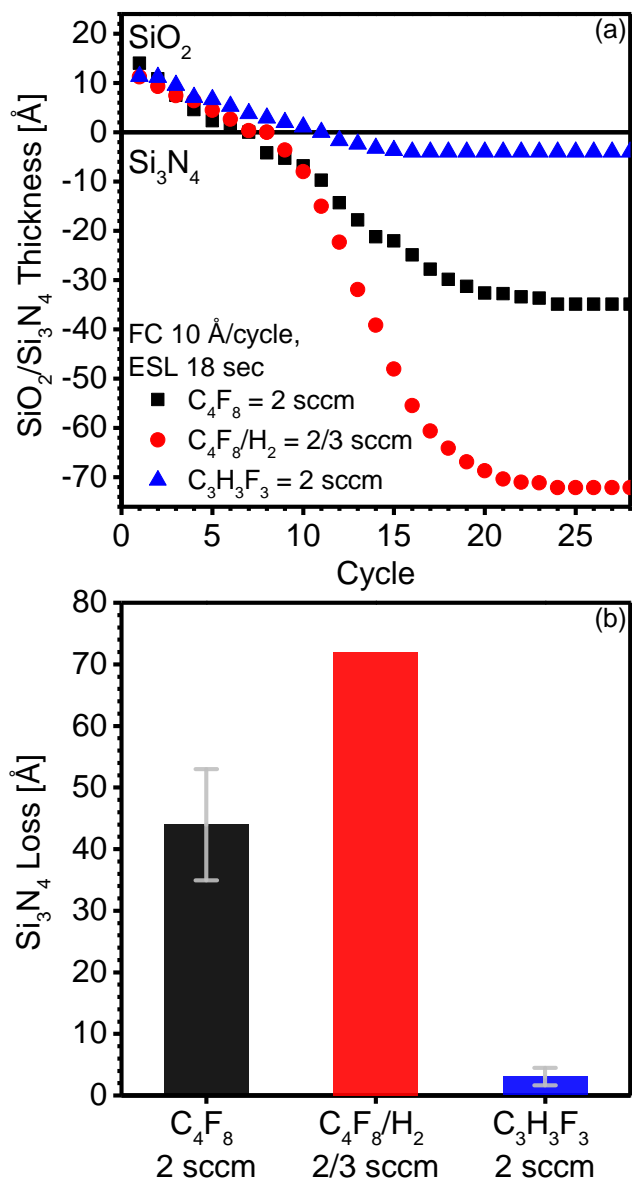


FIG. 2.2. (Color online) (a) SiO₂ and Si₃N₄ layer thickness at the end of each ALE cycle using C₄F₈, C₄F₈/H₂ and C₃H₃F₃, respectively. Si₃N₄ etching stops at various thicknesses. (b) The amount of Si₃N₄ thickness loss before etch stop for three conditions.

To evaluate surface chemical aspects of these processes, XPS spectra for Si₃N₄ ALE using C₄F₈, C₄F₈/H₂ and C₃H₃F₃ at the end of the deposition and etching steps were obtained.

Scans were performed at the beginning of Si₃N₄ etching after the removal of the top SiO₂ layer, for example, the 8th cycle for C₄F₈, the 9th cycle for C₄F₈/H₂ and the 12th cycle for C₃H₃F₃ in Figure 2.2(a). The data shown in Figure 2.3 summarizes the Si2p, C1s and F1s spectra for the set of precursors. XPS intensity difference spectra corresponding to XPS data after etching and deposition steps, respectively, are shown. The Si2p spectra were fitted using fluorinated silicon nitride (Si-NF) and fluorinated silicon oxide (Si-OF) at 102.4 eV and 104.2 eV, respectively.⁴¹ The C1s spectra were fitted using C-C/C-H, C-CF_x, C-F/C-O, C-F₂ and C-F₃ at 284.5 eV, 286.2 eV, 287.9 eV, 290.2 eV and 292.6 eV, respectively.⁵ The F1s spectra were decomposed into F-SiON and F-C at 686.8 eV and 687.8 eV, respectively.^{39, 42-44} XPS intensity differences⁴⁵ between after etching and deposition data for C₄F₈, C₄F₈/H₂ and C₃H₃F₃ were evaluated to clarify the extent of surface reaction by Ar ion bombardment. The spectra were normalized by the total areal intensity of all elements corrected with the relative sensitivity factors on the surface, including Si2p, C1s, N1s, O1s and F1s.⁴⁶

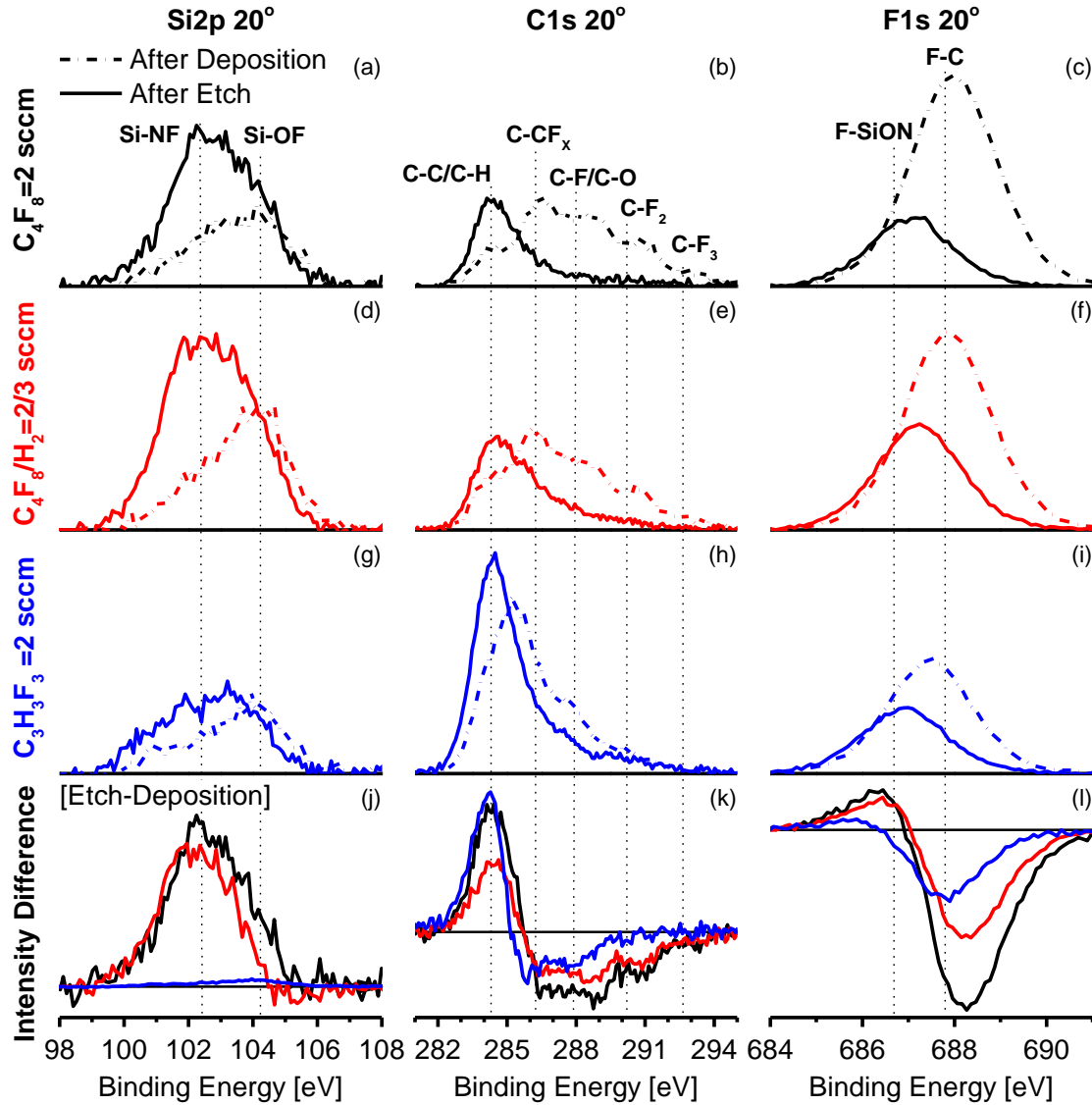


FIG. 2.3. (Color online) Si_3N_4 XPS spectra obtained at a take-off angle of 20° that compare surfaces after ALE using (a-c) C_4F_8 , (d-f) $\text{C}_4\text{F}_8/\text{H}_2$ and (g-i) $\text{C}_3\text{H}_3\text{F}_3$ precursors at the end of deposition and etching steps, respectively. XPS difference spectra formed by subtracting XPS data after the etching step from the data after the deposition step are also shown for the three chemistries (C_4F_8 (black), $\text{C}_4\text{F}_8/\text{H}_2$ (red) and $\text{C}_3\text{H}_3\text{F}_3$ (blue)). The spectra include (j) Si2p, (k) C1s and (l) F1s.

A comparison of the F/C ratios calculated from the C1s and F1s/C1s spectra at a take-off angle of 20° with C₄F₈, C₄F₈/H₂ and C₃H₃F₃-based ALE at the end of deposition and etching steps, respectively, is shown in Figure 2.4(a). The F/C ratios from the C1s spectra measures the fluorine content in the deposited FC layer by calculating the area percentage of weighted C-F, C-F₂ and C-F₃ peaks in the spectra.^{30, 41} The ratio of F1s/C1s spectra measures the fluorine content in both FC layer and underlying Si₃N₄.^{5, 41} By observing the difference between the F/C ratios from the C1s spectra and F1s/C1s spectra, the fluorine reacted with the underlying Si₃N₄ was evaluated. Figure 2.4(b) measures the thickness of the HFC film remained on the Si₃N₄ surface after the Ar ion bombardment by angle-resolved XPS (AR-XPS) using the Si2p signal attenuation obtained from 20° and 90° take-off angles.^{30, 41}

The C1s spectra after FC deposition in Figure 2.3(b) show that C₄F₈ leads to strong C-F/C-O, C-F₂ and C-F₃ peak intensity, whereas mixing H₂ with C₄F₈ in Figure 2.3(e) produce surfaces that exhibit relatively low C-F_x peak intensity. Importantly, C₃H₃F₃ overall minimizes the C-F_x peak intensities, i.e. fluorine content, for the deposited HFC film shown in Figure 2.3(h). The comparison of the F/C ratios from the C1s spectra after deposition step also shows that C₄F₈-based FC film has the highest fluorine content, followed by C₄F₈/H₂ and C₃H₃F₃ (see Figure 2.4(a)). Since the ratio of F1s/C1s spectra is almost identical to the F/C ratios from the C1s spectra, most of the fluorine measured is from the deposited film, and has not reacted with the underlying Si₃N₄. The C1s spectra and F/C ratios confirm that the precursor chemistry used for ALE controls the fluorine content in the deposited film. The results also agree with the study by Li *et al*, suggesting that gaseous precursors with same degree of unsaturation or high F/C ratio can lead to fluorine-rich deposited FC films.²⁶

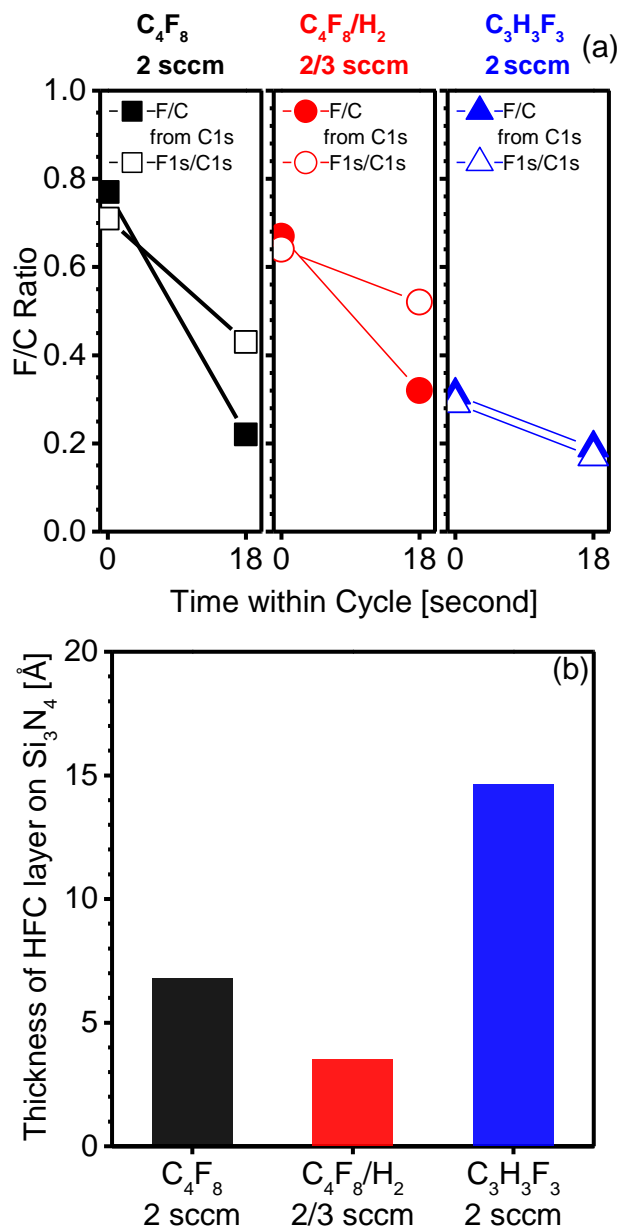


FIG. 2.4. (Color online) (a) A comparison of the F/C ratios from the C1s and F1s/C1s spectra with ALE using C_4F_8 , C_4F_8/H_2 and $C_3H_3F_3$ at the end of deposition and etching steps, respectively. (b) The thickness of the HFC film remained on the Si_3N_4 surface at the end of etching step for the three precursors.

FC film defluorination and reacted material removal take place for C_4F_8 , C_4F_8/H_2 and $C_3H_3F_3$ -based ALE during the etch step. The C1s spectra show the intensity reduction of the C-F_x peaks in Figure 2.3(b), (e) and (h). The intensity of the C-C/C-H peak increase is connected with the FC film defluorination during etching, since the release of fluorine from the film contributes to the formation of a carbon rich layer.^{5, 47, 48} $C_3H_3F_3$ showed a stronger C-C/C-H peak intensity after the etching step, implying that a carbon rich passivating layer remains on the surface in comparison to C_4F_8 and C_4F_8/H_2 . The F/C ratio from the C1s spectra after etching step (see Figure 2.4(a)) also shows the reduction of the fluorine content in the deposited HFC film. At the same time, the etching step also reduces the deposited FC film thickness, so the underlying Si_3N_4 will be exposed more to the fluorine etchant, introducing fluorination and etching of the reacted Si_3N_4 .⁵ The Si2p and F1s spectra after C_4F_8 -based ALE (see Figure 2.3(a) and (c)) exhibit increased Si-NF and Si-OF peak intensities after the etching step. The F/C ratios from the F1s/C1s spectra is relatively higher than the ratios from the C1s spectra after etching step (see Figure 2.4(a)) supports that the fluorine etchant reacts with the underlying Si_3N_4 and results in Si_3N_4 fluorination. With the confirmation from the AR-XPS FC thickness measurements (Figure 2.4(b)), we could conclude that etching of the FC film and fluorination of the Si_3N_4 underneath takes place. Comparison of C_4F_8 , C_4F_8/H_2 shows less remained HFC film and higher fluorination of the underlying Si_3N_4 . Surfaces after $C_3H_3F_3$ -based ALE show least etching of the FC layer and negligible fluorination of the underlying Si_3N_4 .

The XPS difference spectra⁴⁵ after FC film deposition and etching for C_4F_8 , C_4F_8/H_2 and $C_3H_3F_3$ were used to clarify the extent of surface reactions and are shown in Figure 2.3(j-l). The spectra were normalized to the sum of the Si2p, C1s, N1s, O1s and F1s areal intensities corrected

with the relative sensitivity factors.⁴⁶ The C1s difference spectra in Figure 2.3(k) confirms that C₃H₃F₃-based ALE deposits contain the minimum amount of fluorine in the HFC film, whereas the use of H₂ reduces both the F/C ratio of the deposited film and overall amount of the FC layer as compared to C₄F₈. The fact that H₂ enhances the removal of the remaining FC film for the Si₃N₄ surface and causes less FC film coverage can be seen from the lowered intensity of the C-C/C-H peak.

The fluorination level of the underlying Si₃N₄ due to the fluorine etchant released from the deposited FC film as a result of Ar ion bombardment is mirrored by the areas of the Si-NF, Si-OF and F-SiON peaks in the Si2p and F1s intensity difference spectra shown in Figs. 2.3(j) and 2.3(l). In the F1s intensity difference spectra, C₄F₈ and C₄F₈/H₂ shows strong fluorination on the underlying Si₃N₄, which is the reacted layer that will be etched in the etching step, whereas C₃H₃F₃ shows little SiON-F peak formation. The formation of the F-SiON peak in the F1s spectra may be correlated with the Si₃N₄ loss before formation of a FC passivation layer and etch stop. Since Ar ion bombardment during the etching step causes removal of fluorinated products, the Si₃N₄ loss is positively correlated to the F-SiON peak area of the material. The XPS difference spectra qualitatively agree with the SiO₂ and Si₃N₄ thickness changes measured by ellipsometry. For C₄F₈ and C₄F₈/H₂-based ALE, more Si₃N₄ loss is required before a sufficiently thick FC passivating layer is established. The classical concept of gas mixing by combining C₄F₈ and H₂ does not reduce the material loss for FC-assisted ALE because of the strong loss of the surface passivation layer as a result of hydrogen induced etching of the FC film.

2.3.2 SiO₂ and Si ALE

Selective ALE of SiO₂ over a Si underlayer was examined using the identical set of precursors just discussed for SiO₂-Si₃N₄-SiO₂ stacks. Results for SiO₂-Si-SiO₂ stacks are shown in Figure 2.5(a). For the FC assisted ALE based on C₄F₈, the Si thickness loss before establishing a sufficiently thick FC film to stop Si removal is about 9 Å. When C₄F₈ was mixed with H₂, a higher thickness EPC of SiO₂ and Si is observed and the Si thickness loss increases to ~40 Å at the 30th cycle. For C₃H₃F₃-based ALE, a comparable SiO₂ EPC to that when using C₄F₈ is observed. However, in this case a reduced Si EPC is seen for C₃H₃F₃ once the process starts to etch Si. No more Si loss or Si EPC reduced to a negligible amount of less than 1 Å is observed after the 19th cycle. This shows that for a C₃H₃F₃ ALE precursor a HFC passivation layer can rapidly build up and prevent Si loss.

For a selective SiO₂ ALE process, the Si thickness loss should be minimal. The precursor dependence of Si thickness loss before Si etching stop is shown in Figure 2.5(b). C₃H₃F₃ has the minimum Si thickness loss (~2 Å) as compared to the other precursors examined (C₄F₈ ~10 Å and C₄F₈/H₂ ~40 Å). This result reveals that high ALE selectivity can be achieved by optimizing the chemical structure and composition of the reactive film using different precursors. Our result also suggest that the concept of precursor mixing used in continuous plasma etching for improving SiO₂ over Si ALE selectivity is ineffective for FC-assisted ALE since the times required for suppressing substrate etching are impractically long.

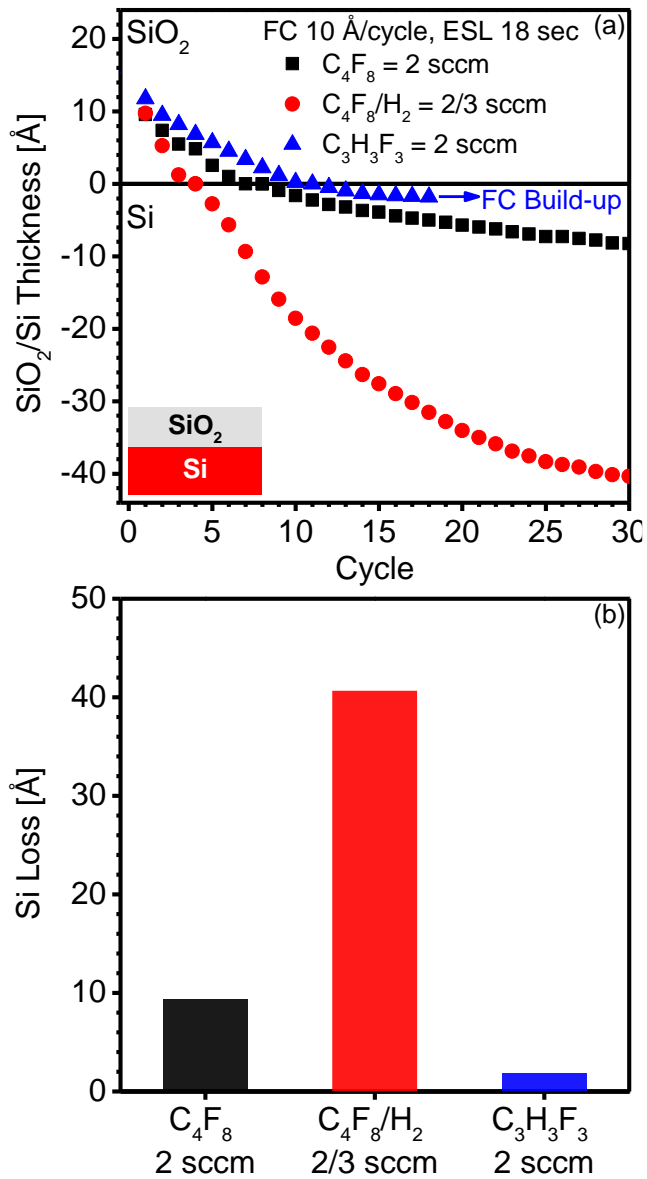


FIG. 2.5. (Color online) (a) SiO₂ and Si thicknesses at the end of each ALE cycle using C₄F₈, C₄F₈/H₂ and C₃H₃F₃ precursors. (b) Precursor chemistry dependence of Si thickness loss prior to Si etch stop as the result of formation of a passivation layer.

2.4 Discussion

The chemical nature of the precursors in ALE has a more profound influence than that in a CW plasma to form a passivation layer with appropriate chemical makeup and achieve etching selectivity of materials. In CW plasma, etching selectivity is frequently achieved by mixing etching precursors and gas additives to control the thickness and chemistry of the deposited film and thus regulate etching behavior of selected materials.^{40, 49-54} Since reactive gases are continuously supplied into the chamber, the films formed on the surface are constantly being reformed and a steady-state surface film thickness forms.⁴⁰ For C_4F_8/H_2 CW plasma, the etching selectivity of SiO_2 over Si can be achieved, since the H_2 reduces the fluorine content of the steady-state passivation film formed on the surface by fluorine abstraction.^{50, 54-56} This can also lead to an enhancement of the FC film thickness on the Si surface which reduces penetration of etchant to the substrate.^{35, 40, 41} Our results show that the concept of mixing FC precursors with H_2 in ALE does not enhance materials etching selectivity and increases substrate material losses. In an ALE approach, the injection of H_2 can reduce the fluorine content of the FC layer on the surface but also decreases the overall thickness of the FC passivation layer, thus reducing etching selectivity. The XPS C1s difference spectra (see Figure 2.3(k)) show that the C-C/C-H peak intensity with C_4F_8/H_2 is significantly lower than the intensity with C_4F_8 , implying less FC film remaining on the surface after the etching step, which can be confirmed from the difference of F/C ratios and AR-XPS thickness. For the $C_3H_3F_3$ precursor, we observed enhanced fluorine reduction of the deposited HFC layer on the surface without excessive thinning of the HFC passivation layer thickness as seen in the case of C_4F_8/H_2 mixtures. For instance, the intensity of the C-C/C-H peaks of films deposited using $C_3H_3F_3$ is comparable or slightly higher than the

intensity of the same peaks for C_4F_8 (see Figure 2.3(k)). Simultaneously, the use of $C_3H_3F_3$ enables ALE of SiO_2 and Si_3N_4 or Si underlayer material losses at the Angstrom level.

2.5 Summary and Conclusions

In this work, the potential of utilizing a complex molecular precursor for achieving ultra-high etching selectivity in ALE of SiO_2 over Si_3N_4 or Si was studied by comparing its performance with gas mixtures, i.e. $C_3H_3F_3$ relative to C_4F_8/H_2 . In contrast to CW plasma etching where use of gas mixtures is common and can be used for highly selective material removal, we find that this approach fails for ALE. In the case of CW plasma, the tailoring of the chemistry of a constantly refreshed steady-state surface passivation is required. This approach fails for the case of C_4F_8/H_2 -based ALE. H_2 addition to C_4F_8 does not enhance materials etching selectivity and instead leads to more Si_3N_4 or Si loss. Our surface characterization data show that H_2 not only reduces the $C-F_x$ group content of the HFC deposited film, but also reduces the thickness of this reaction layer and leaves a greater amount of unbonded fluorine (F1s) which can readily react with the Si_3N_4 or Si surfaces during Ar bombardment. On the other hand, $C_3H_3F_3$ -based ALE enables reduced fluorine content of the deposited film without suppressing the formation of a HFC passivation film on the substrate, and results in ultra-high ALE selectivity with Angstrom level material loss. This work suggests that utilizing the molecular structure of HFC precursors in ALE offers significant advantages for achieving materials selective ALE.

2.6 Acknowledgments

Substrates were produced in the Microelectronics Research Laboratory (MRL) at the T. J. Watson Research Center in Yorktown Heights, NY. The authors gratefully acknowledge the financial support of this work by the Semiconductor Research Corporation (2017-NM-2726). The authors thank A. Knoll, P. Luan and A. Pranda for helpful discussions and collaboration. We also thank H.C. Chen from Taiwan Semiconductor Manufacturing Company, H. Cottle from Tokyo Electron Limited, J. Tan from Intel, and C. Labelle and C. Park from GLOBALFOUNDRIES for valuable suggestions on this work.

Chapter 3: Selective atomic layer etching of HfO₂ over silicon by precursor and substrate-dependent selective deposition

Journal of Vacuum Science & Technology A 38, 032601 (2020)

K. Y. Lin, C. Li, S. Engelmann, R. L. Bruce, E. A. Joseph, D. Metzler, and G. S. Oehrlein

K.Y. Lin contributed to the design and conduction of the research, to the analysis of the experimental results, and to the writing of the manuscript.

All authors discussed the results, commented on and made changes to the manuscript.

ABSTRACT

The early work of John Coburn and Harold Winters revealed a synergistic effect in ion-enhanced Si etching by the concurrent irradiation of Ar⁺ and XeF₂. This finding provided an important foundation for the development of plasma dry etching processes. The experimental results of Coburn and Winters also found effects that are useful for the development of atomic layer etching (ALE) processes characterized by a self-limited etch rate. ALE approaches are widely established and can be utilized in either directional or isotropic etching by employing proper surface modification and product removal steps. Nevertheless, the development of material selective ALE processes is still limited. An approach that combines substrate-selective deposition with etching opens a new processing window for selective ALE. We studied the

deposition behavior of mixtures of methane (CH_4) with trifluoromethane (CHF_3) and mixtures of methane with octafluorocyclobutane (C_4F_8), on HfO_2 and Si surfaces. The experimental results show that a $\text{CH}_4/\text{C}_4\text{F}_8$ mixture produces a comparable FC deposition thickness on both HfO_2 and Si during the deposition step. In contrast, a CH_4/CHF_3 mixture deposits a FC film on Si, whereas it fluorinates the HfO_2 surface with negligible FC deposition. Utilizing these behaviors allows for an ALE process based on CH_4/CHF_3 for selective removal of HfO_2 over Si. Surface characterization data that provide mechanistic insights on these processes are also provided and discussed.

3.1 Introduction

The work of John Coburn - to whom this special issue is dedicated - and his colleague Harold Winters has provided a foundation for the understanding of radiation-enhanced etching reactions.⁵⁷⁻⁵⁹ In Figure, 3.1(a) we reproduce the classic plot of ion-neutral synergy in ion-enhanced steady-state etching published by Coburn and Winters⁵⁷ and discuss how their quintessential experiment teaches how to perform atomic layer etching (ALE) based on ion stimulation. They studied the etch rate (ER) of amorphous Si subjected to fluxes of XeF₂ gas alone, a 450 eV Ar⁺ beam and XeF₂ together, and the 450 eV Ar⁺ beam alone. When both the XeF₂ and Ar⁺ are simultaneously incident on the Si surface, the synergistic effect leads to a high ER of Si that exceeds the sum of the ERs obtained with each beam separately. Light mass ions, such as Ne⁺ and He⁺, with a different modification reactant, Cl₂, also show a synergistic effect in the ER on Si.⁶⁰ These findings show that using surface modification and ion bombardment concurrently on the surface enhances the ER, and provides an important foundation for directional plasma-based dry etching processes.⁶¹

Self-limited ALE is based on a temporally decaying neutral-ion synergy effect that vanishes as the neutral surface coverage disappears. This process is also evident in the original result of Coburn and Winters. In addition to the synergistic effect during simultaneous neutral-ion exposures, the original plot of Coburn and Winters in Figure 3.1(a) also shows the influence of changes in neutral coverage and evidence of how self-limited etching may be achieved during the transitions. The excess fluorination of the amorphous Si formed during the XeF₂ gas-only experiments results in an initial increase of the Si ER as both the Ar⁺ and XeF₂ interact with the

Si surface as compared to the steady-state. One possible interpretation is that a steady-state ER of Si is only established once the rate of surface fluorination and Si removal reaches a stable situation. Another example is the transition from having both the Ar⁺ and XeF₂ present to just Ar⁺ beam bombardment only. The temporal data show how the Si ER is significantly reduced with processing time until finally a removal rate of Si solely corresponding to physical sputtering is reached. The reduction of the Si ER is due to the removal of residual fluorination of the Si surface during the period when Ar⁺ ion beam irradiation is performed. Such etching behavior is similar to a typical ALE process as shown in Figure 3.1(b), where the surface with precursor exposure undergoes chemical modification and the subsequent Ar⁺ bombardment removes one or multiple reacted layers. In fact, a combination of XeF₂ gas injection in step 1, followed by Ar⁺ beam irradiation in step 2, is consistent with the ALE method, as shown in Figure 3.1(a) and 3.1(b). The experimental result published by Coburn and Winters uncovers not only the synergistic effect but also contains information on how self-limited ion-based ALE may be achieved. Clearly, this requires reducing the Si ER to a diminished value during the surface functionalization step, e.g. by lowering temperature in the case of F-based Si etching or using Cl₂ or other halogens to suppress spontaneous Si etching. Secondly, low energy ion bombardment is helpful to reduce the physical sputtering rate. Nevertheless, this rate is small relative to the initial ER seen during step 2.

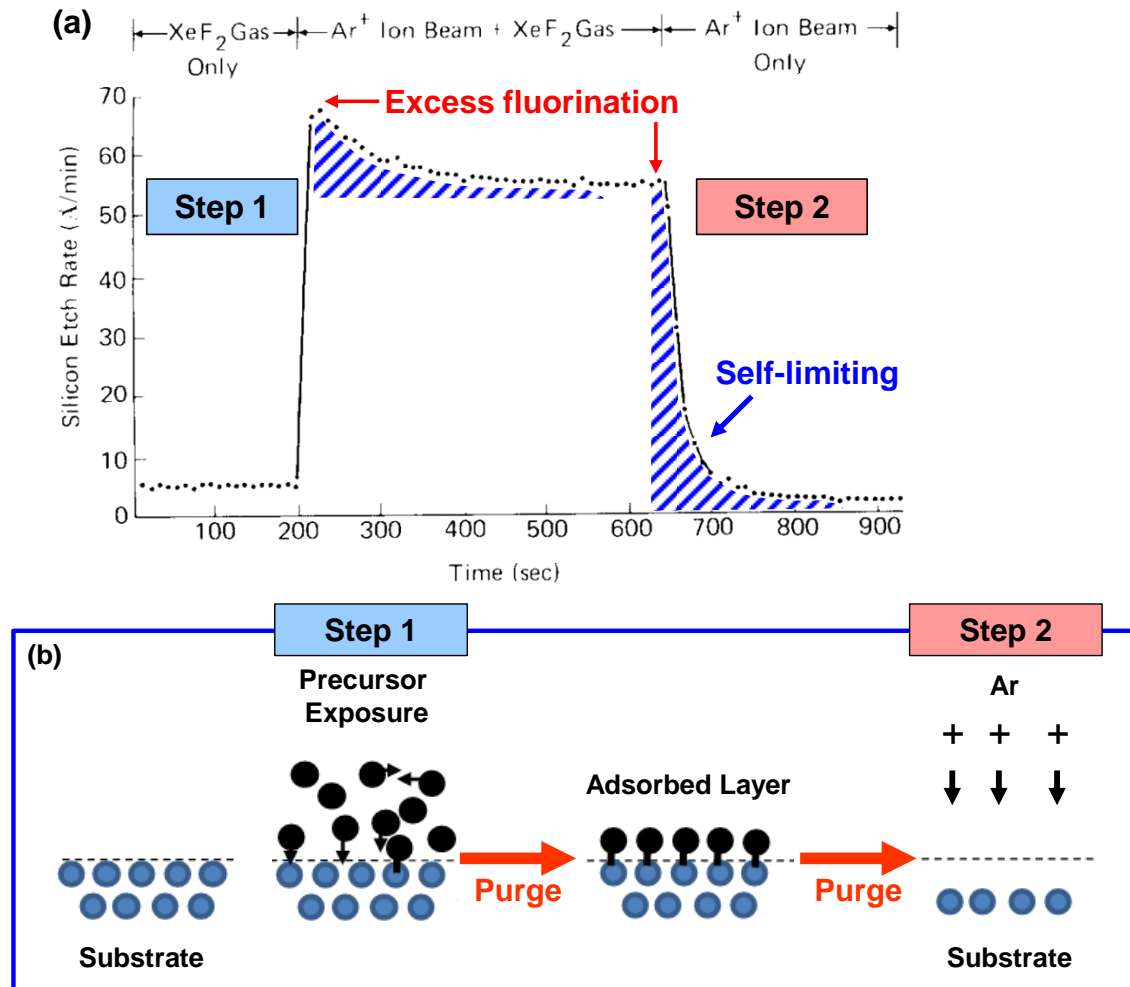


Fig. 3.1 (Color online) (a) Ion-enhanced etching of amorphous-Si using XeF₂ gas and a 450 eV Ar⁺ beam, from Coburn and Winters. Reprinted with permission from ref (⁵⁷). Copyright 1979 American Institute of Physics. (b) Schematic illustrating a typical ALE sequence that is similar to the concept of the early work published by Coburn and Winters (redrawn after Oehrlein *et al*¹²).

3.2 Technical Motivation Review

ALE approaches offer advantages that include simplified process steps, self-limited etching, pattern transfer fidelity, and potentially ultra-high etching selectivity for the future

development of integrated circuits (ICs).^{12, 14, 15, 62, 63} This approach is now widely established. In addition to ions^{4, 8, 33}, light^{64, 65}, electrons^{21-23, 57, 66}, or heating⁶⁷⁻⁷⁰ is used as an alternative for product removal. For example, Athavale and Economou demonstrated Si ALE using chlorine gas that chemisorbs on the Si surface. The sequential Ar⁺ beam sputters away a monolayer of the chlorinated Si.⁴ Additionally, it is possible to perform the surface modification step using ions to change the material in a directional fashion, and then apply thermal techniques for product removal. Isotropic ALE can be conducted in a manner where precursor gases and/or radicals are used for surface modification to modify the material followed by a ligand exchange or heating process to remove the product.^{71, 72}

All of these ALE approaches need to fulfill the processing requirement of selective removal. The following section will discuss the mechanism of establishing selective ALE and its limitations. Since the integration of substrate-selective deposition and etching potentially opens a new window for selective ALE, a brief summary of recent studies in area selective deposition (ASD) is included as well. In the last section, we will investigate the selective ALE based on the substrate-selective deposition.

3.2.1 Achieving Material Etching Selectivity in ALE.

Material etching selectivity in ALE can be based on different mechanisms. For instance, Cl₂-based ALE of Si uses the thermodynamically favorable chlorination of Si, so a sequential low energy Ar⁺ bombardment step allows for the selective removal of the chlorinated Si layers but not SiO₂ or unreacted Si.²⁻⁴ Consistent with this concept, Kanarik *et al* suggested that when reactants chemically modify an etching material, the modified material has lower bond energy

than the non-etching material. The energy difference provides a processing window to achieve material selective ALE.⁷³ If this approach is feasible for every etching process, the selectivity of ALE should be easily obtainable.

Silicon-to-SiO₂ etching selectivity is easily achieved due to a higher energy threshold of chlorinating SiO₂ (230 kJ/mol), compared with that of chlorinating Si (-159 kJ/mol).¹

Nevertheless, using a Cl₂-based precursor to weaken the binding energy of the etching material has limitations, for example, etching SiO₂ with selectivity to Si is not feasible. Metzler *et al* developed a fluorocarbon (FC)-based ALE process, composed of a cyclic sequence of FC deposition and etching steps, to realize as self-limited layer-by-layer etching of SiO₂.^{8, 33, 74} In the deposition step, an injected FC reactant is dissociated and then deposits a thin FC layer on the SiO₂ surface, fluorinating the underlying material. The subsequent etching step employing low energy Ar⁺ ion bombardment induces further mixing and enables removal of the fluorinated layer.⁷⁵

FC-based ALE processes are capable of achieving the etching selectivity of SiO₂ over Si⁶⁻⁸ based on a much higher FC consumption rate of SiO₂ as compared to Si. By optimizing the processing parameters, including deposition thickness, substrate bias power and etching step length (ESL), it enables a steady etch amount per cycle (EPC) of SiO₂ while simultaneously building up a thick FC passivation layer on top of Si to mitigate material loss. Many papers discussed the processing parameters in FC-based ALE regarding the selectivity of SiO₂/Si^{5, 7, 76, 77}, SiO₂/Si₃N₄^{30, 77, 78}, and Si₃N₄/Si^{31, 32}.

However, FC-based ALE requires a transition for building up a passivation layer on the non-etching area, which naturally causes some degree of material loss. Huard *et al* modeled this

transient behavior for ALE of SiO₂ and Si₃N₄ by varying the deposition thickness and ESL.⁷⁷ Under the optimal ratio of the deposition thickness and ESL, a FC-based ALE can quickly develop a passivation layer on Si₃N₄ while maintaining a steady-state EPC of SiO₂. In addition to parameter optimization, surface pretreatment can be used to minimize this transient duration or to control etching selectivity. Gasvoda *et al* investigated a selective organic functionalization on SiO₂, but not on Si₃N₄, for controlling the EPC.⁷⁹ The SiO₂ surface is functionalized using bis(dimethylamino)dimethyl silane in the gas phase, which reacts with the surface –SiOH groups in a self-limiting manner. After this reaction, the SiO₂ surface is formed with Si-CH₃ groups, whereas Si₃N₄ is not functionalized. Since the Si-CH₃ groups on SiO₂ prompt the formation of a passivation layer, such surface functionalization demonstrates hydrofluorocarbon (HFC)-based ALE of Si₃N₄ with selectivity to SiO₂. Fundamentally, selectivity can be obtained for material systems that have also demonstrated selectivity in continuous wave (CW) plasmas.

The above-mentioned approaches do not work well for etching high dielectric (high-*k*) materials, such as HfO₂, with selectivity to Si because of the low volatility of halogen-terminated etching products, e.g. fluorinated HfO₂.⁸⁰ Even with Cl₂ or BCl₃ etchants, HfO₂ etching still requires a certain level of ion energy⁸¹⁻⁸³ or an elevated substrate temperature^{84, 85} to facilitate the removal of etching byproducts. These methods inevitably cause extra Si losses, deteriorating the etching selectivity of HfO₂ to Si. Moreover, emerging non-volatile memory (NVM) applications increasingly adapt HfO₂ in resistive random-access-memory (ReRAM), where the etching recipe containing Cl₂-based chemistries potentially induces a serious concern for corrosion.⁸⁶ Thus, there is a need to develop a new selective ALE approach. Some pioneering studies^{73, 87} showed a concept that integrates area selective deposition with etching to achieve etching selectivity. The

selective deposition step builds up a passivation layer on the non-etching area, allowing the subsequent etching step to remove the material in the etching area. We will briefly summarize the recent progress in area selective deposition (ASD) before discussing an ALE approach that utilizes substrate-selective deposition.

3.2.2 Area Selective Deposition

ASD is a bottom-up approach that features self-aligned patterning by selective deposition on the surface of specific materials. The selectivity of ASD is based on the seeding energy difference between the growth and the non-growth area. Film deposition takes place immediately when the surface is favorable for the nucleation and growth of precursor, whereas the non-growth area has an energy barrier for formation of nuclei.

The deposition selectivity, however, is incrementally degraded as precursor begins to arrive at the substrate surface, so an approach to reinforce the selectivity is required. These approaches include, but are not limited to a) sample pretreatment to prolong the incubation time⁸⁸⁻⁹¹, b) non-growth area deactivation⁹²⁻⁹⁹ by self-assembled monolayers (SAMs), c) ASD by surface activation^{100, 101}, d) ALD super-cycles with an inhibitor step⁹⁰, e) super-cycles consisted of an etching step to restore an incubation time on the non-growth area¹⁰²⁻¹⁰⁷, among others.

One of the examples for non-growth area deactivation by SAMs is shown in Figure 3.2. The SAM comprises a head group and tail, where the head group selectively deposits on the non-growth area and the tail is chemically inert to ALD precursors. F. Hashemi *et al* used octadecylphosphonic acid self-assembled monolayers (ODPA SAMs) to form a blocking layer on the surface of copper, including CuO, Cu₂O and Cu, but the SAMs did not chemically adsorb

on SiO₂. The sequential ALD process is allowed to deposit a dielectric film on the patterns. An etchant, then, is applied for selectively removing the SAMs and any residual deposited dielectric film on the Cu surface, without the interference of the dielectric film on SiO₂.

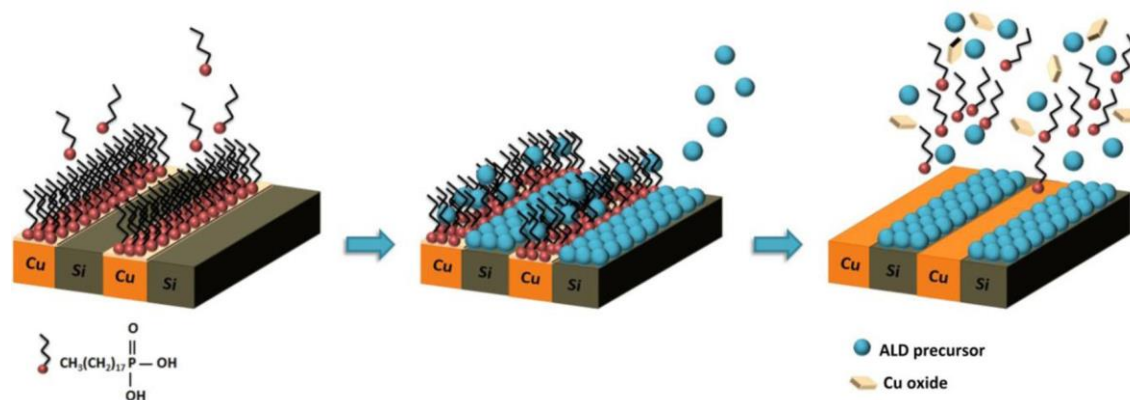


Fig. 3.2 (Color online) is a schematic illustrating ODPA SAMs that deactivate the ALD processing on Cu oxide, enabling a dielectric film deposited on SiO₂. The sequential treatment of the acid solution selectively removes the SAMs. Reprinted with permission from ref (⁹⁶). Copyright 2015 American Chemical Society.

Besides surface deactivation by SAMs, area selective ALD (AS-ALD) by super-cycles that combine with a selective etching step has been extensively studied. The processing schematic is shown in Figure 3.3. For example, Vallat *et al* introduced a super-cycle of the NF₃/O₂/Ar etching step in the Ta₂O₅ ALD process to remove an undesired Ta₂O₅ layer on the Si non-growth areas and reestablish selective deposition.¹⁰⁸ Furthermore, the non-growth area can be chemically deactivated by an inhibitor prior to ALD steps to prolong an incubation time. Mameli *et al* demonstrated the use of an acetylacetone inhibitor suppressing the seeding of the SiO₂ ALD precursor, bis(diethylamino)silane, on the Al₂O₃ surface.⁹⁰ A combination of an inhibitor step prior to an ALD process and super-cycles with an etching step potentially can

maximize the deposition selectivity. Several literatures^{104, 109-112} have detailed and thoroughly reviewed the recent developments in AS-ALD.

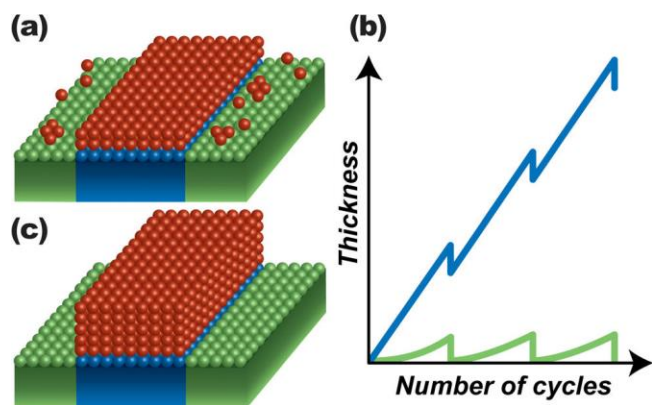


Fig. 3.3 (Color online) the selectivity of AS-ALD is improved by introducing super-cycles of a selective etching step. Reprinted with permission from ref (¹⁰⁴),

<https://doi.org/10.1021/acs.chemmater.8b03454> . Copyright 2018 American Chemical Society.

3.2.3 Substrate Selective Deposit-Based ALE

Once ASD and/or AS-ALD can precisely cover a given area, it enables substrate selective deposit-based ALE. The deposited film can be used for coating a passivation layer on the non-etching area for the improvement of etching resistance. A sequential etching step easily removes the material in the etching area where there is no deposition film. A novel way of selective ALE utilizing selective deposition and etching steps is potentially feasible. (To clarify the terminology used in this section, ASD can be used for describing the deposition selectivity that is derived from the different substrate materials or positions, e.g. the sidewall relative to the top of a fin structure. In substrate-selective deposition, the selectivity is achieved between different substrate materials. For the evaluation of selective ALE, the approach of substrate-selective deposition is

more favorable.) Exploiting the phenomenon of material selective deposition to achieve selective ALE has not yet been demonstrated. In this work, we study a FC-based ALE approach that involves material selective deposition^{73,87} for etching HfO₂ with selectivity to Si.

FC-based continuous wave (CW) plasma hardly etches HfO₂ due to the low volatility of etching byproducts. Hafnium tetrafluoride (HfF₄) has a boiling point of 970 °C under one atmosphere, whereas the boiling point of fluorinated Si (SiF₄) is -86 °C.^{18, 113, 114} The nature of FC-based CW plasma restricts the processing window to achieve etching selectivity of HfO₂ over Si, even with H₂ additives to enhance fluorine abstraction and increase the HFC deposition yield on Si.^{18, 80, 115} ALE based on sequential processing steps, i.e. cyclic deposition and etching steps, involves non-steady state plasma-surface interactions, since the reactants are not constantly supplied to the substrate surface. The chemical structure of precursors significantly affects the plasma surface interaction.^{12, 16, 76, 116} Takahashi and Ono studied etching products of HfO₂ using Ar/C₄F₈ and Ar/C₄F₈/H₂ CW plasmas by quadrupole mass spectroscopy (QMS).^{113, 115} Their results suggested that H₂ additives in a FC plasma prompt the evaporation of fluorinated HfO₂ products by forming HfCH_x⁺ (x = 0-4) and HfH_xF⁺ (x = 0-2) organometallic volatile products and enhance the deposition yield on Si. CHF₃-based ALE delivers a higher deposition yield on Si than SiO₂.⁵ These results indicate that evaluating the surface interactions of HFC/FC precursors on HfO₂ during an ALE process may be promising with regard to exploiting differences in HFC film formation on HfO₂ as compared to Si towards establishing HfO₂/Si etching selectivity.

The first part of this work evaluates the deposition behavior of HFC/FC mixtures on HfO₂ and Si for ALE sequences. The experiments are mainly focused on the thickness evolution

of the deposited HFC films. X-ray photoelectron spectroscopy (XPS) analysis is also used to understand the surface chemistry evolution related to the chemical structure of the studied precursors at each step. The second part of this work focuses on applying FC-based ALE to achieve selective ALE of HfO₂ relative to Si-based on the phenomenon of substrate selective deposition. A brief summary discusses the relation between the major reactive species generated from the HFC/FC plasmas and surface interactions at the conclusion of this paper.

3.2 Experimental

The experimental setup closely matches that used in our previous publications^{8, 30, 76} and is briefly described. This work was conducted using an inductively coupled plasma (ICP) reactor. A stovetop-like, water-cooled coil with a diameter of 16 cm above a 19-mm-thick quartz coupling window was powered by a 13.56 MHz power supply with an L-type matching network. The plasma was confined within an anodized Al confinement ring with a 195 mm diameter. A Si substrate with a 125 mm diameter was located 150 mm below the top electrode on an electrostatic chuck and can be independently biased at the radiofrequency (RF) of 3.7 MHz. The base pressure achieved before processing was in the 1×10^{-7} Torr range. The temperature of the $25 \times 25 \text{ mm}^2$ sample was stabilized by substrate backside cooling at 10 °C during plasma processing. To minimize environmental impacts during the sample exchange, a load lock and vacuum transfer system was used for all experiments. The detailed configuration of the plasma reactor can be found in the references^{35, 36}. Before each experiment, O₂ plasma-based cleaning and Ar plasma-based conditioning processes were employed to ensure that the condition of the reaction chamber remained consistent.^{37, 117} An *in situ* ellipsometer with a He-Ne laser operating

at a wavelength of 632.8 nm mounted on the plasma reactor allowed us to study material thickness changes in real-time.³⁸ The sampling rate of the ellipsometer was set to 5 Hz (0.2 seconds per point) for all experiments.

Two sets of multi-layer stacked samples: a) ALD-HfO₂/Si/SiO₂ with a thickness of 3/10/30 nm and b) Si/SiO₂ with a thickness of 5/30 nm deposited on a Si substrate were used to evaluate the deposition behavior on HfO₂ and Si surfaces. Annealed HfO₂, which exhibits higher etching resistance compared to ALD-HfO₂ due to its higher degree of crystallinity, was also employed.^{118, 119} The material is widely used as gate material because of the high thermal stability and better electrical characteristics, compared to those of SiO₂ and ALD-HfO₂.¹²⁰ In order to study the etching performance, including the ability to etch annealed HfO₂ and etching selectivity of annealed HfO₂ relative to Si, we also prepared annealed HfO₂/Si/SiO₂ by rapid thermal annealing (RTA) in a furnace at 700 °C in N₂ flow at 2 Torr for 30 seconds.

The ALE experiments were conducted using a FC-assisted ALE procedure, where a steady-state Ar plasma is utilized in conjunction with a periodic injection of a defined amount of precursor gases and synchronized plasma-based Ar⁺ ion bombardment. The detailed process sequence is shown in Figure 3.4, and is similar to our previous work.^{7, 30, 76} All plasma processes presented in this work operate with a source power of 200 W and a 50 standard cubic centimeters per minute (sccm) Ar carrier gas flow at a processing pressure of 10 mTorr. The ALE process consists of a deposition step and an etching step. In the deposition step, a selected set of precursors was injected with a duration of 2 seconds to deposit a 10 Å thick FC/HFC film on the substrate. This step was followed by a 12-second purge step to pump out the residual precursor gas. The precursors studied include a) mixtures of methane (CH₄) with octafluorocyclobutane

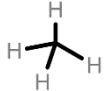
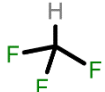
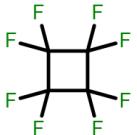
(C₄F₈) and b) mixtures of methane with trifluoromethane (CHF₃). Information on the precursor gases is listed in Table 3.1. The mixing ratio of the studied precursors were a) a 1:1 mixture of CH₄/C₄F₈ and b) a 1:1 mixture of CH₄/CHF₃.

For the etching step, a -15 V RF bias voltage was applied with an etching step length (ESL) of 18 seconds, accelerating Ar⁺ ions to a maximum kinetic energy of 30 eV to react the deposited film and substrate. Since the film thickness deposited by the selected set of precursors may be different on HfO₂ and Si surfaces, the experiment was set to deposit a 10 Å thick film on Si at the beginning cycles by fine-tuning the mass flow controller to control the amount of injected precursor gases. The same amount of precursor injection was applied for HfO₂.

Surface chemistry modification with regard to precursor chemistry was obtained by XPS analysis of processed samples at the end of the deposition and etching steps. The samples were transferred under ultrahigh vacuum (UHV) to a Vacuum Generators ESCALAB MK II surface analysis system for XPS measurements. Photoelectrons were emitted using a non-monochromated Al K α x-ray source (1486.6 eV). High-resolution scans of the Hf4f, Si2p, C1s, O1s, and F1s spectra were obtained at 20 eV pass energy at two takeoff angles, 20° (shallow probing depth \approx 20-30 Å) and 90° (deep probing depth \approx 80 Å), with respect to the sample surface. The spectra were calibrated by the binding energy position of the C-C peak to 285 eV and fitted using least square fitting after Shirley background subtraction.^{39, 40} The Hf4f spectra were fitted using hafnium dioxide (HfO₂)^{121, 122}, at 16.7 eV and 18.2 eV for Hf4f_{7/2} and Hf4f_{5/2}, and fluorinated hafnium oxide (HfO_xF_y)¹⁸, at 18.6 eV and 20.3 eV for Hf4f_{7/2} and Hf4f_{5/2}. The Si2p spectra were fitted using elemental Si, Si-F, Si-F₂, Si-F₃, Si-O₂ and Si-O_xF_y at 99.3 eV, 100.5 eV, 101.5 eV, 103 eV, 103.4 eV and 104.2 eV, respectively.^{5, 39, 41, 121} The FC deposition film in the

C1s spectra was fitted using C-C/C-H, C-CF_x, C-F/C-O, C-F₂ and C-F₃ at 285 eV, 286.2 eV, 287.9 eV, 290.2 eV and 292.6 eV, respectively.^{5, 41, 80, 121, 123} The adventitious carbon contamination on a pristine sample in the C1s spectra was fitted using C-C, C-O-C and O-C=O for 285 eV, 286 eV and 288.5 eV, respectively.¹²¹ The O1s spectra were fitted using Hf-O, -OH, and Hf-O_xF_y at 530.4 eV, 531.7 eV and 532.2 eV, respectively.^{121, 122, 124} The F1s spectra were decomposed into Hf-O_xF_y and F-C at 685.5 eV and 688.5 eV, respectively.^{18, 44, 80}

Table 3.1. Molecular formula, name and structure of precursors used in this work.

Molecular Formula	Name	Structure
CH ₄	Methane	
CHF ₃	Trifluoromethane	
C ₄ F ₈	Octafluorocyclobutane	

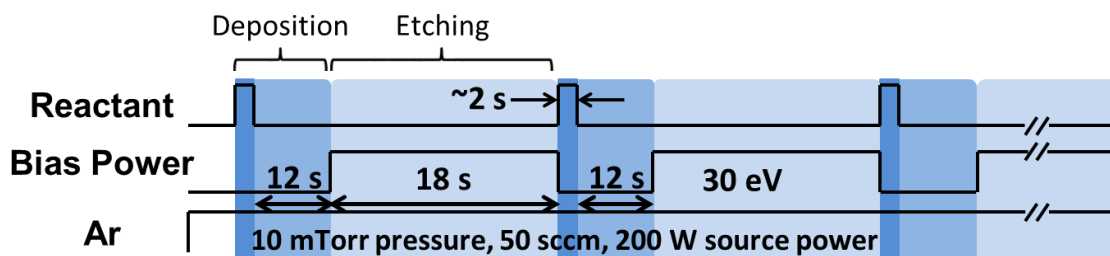


Fig. 3.4 (Color online) is a schematic diagram of the atomic layer etching (ALE) cyclic process. The deposition step employs reactant injection and deposition on the substrate followed by a 12 s purge step to remove the residual reactants from the processing chamber. The etching step introduces a substrate bias for ion-assisted chemical etching of the FC deposition film and reacted layer. The experiment was designed to study the deposition behaviors on HfO₂ and Si, so the deposition parameter was set to obtain a 10 Å thick deposition on Si at the end of the injection step in the beginning cycles and apply the same injection amount of the reactant to HfO₂ to observe any differences in the deposition yield.

3.3 Results and Discussion

3.3.1 Comparison of CH₄/C₄F₈ And CH₄/CHF₃ on Si And HfO₂

3.3.1.1 Deposition Behavior

The thickness change of the deposited HFC film for the CH₄/C₄F₈-based ALE sequence on Si and HfO₂, respectively, is shown in Figure 3.5(a) and (b). Figure 3.5(a) shows that some deposited FC remains on the Si surface at the end of the etching step and gradually builds up with the number of process cycles. The FC buildup is due to the combination of a low FC consumption rate by Si and the use of a short ESL of 18 s and -15 V bias power for the etching step.^{5, 30, 40, 77, 125} Figure 3.5(b) shows that the CH₄/C₄F₈ mixture also deposits a ~10 Å thick film at the end of the precursor injection step on the HfO₂ surface, and leads to FC accumulation after a few processing cycles. Overall, the use of the CH₄/C₄F₈ mixture for ALE process cycles produces comparable deposition film thickness on Si and HfO₂.

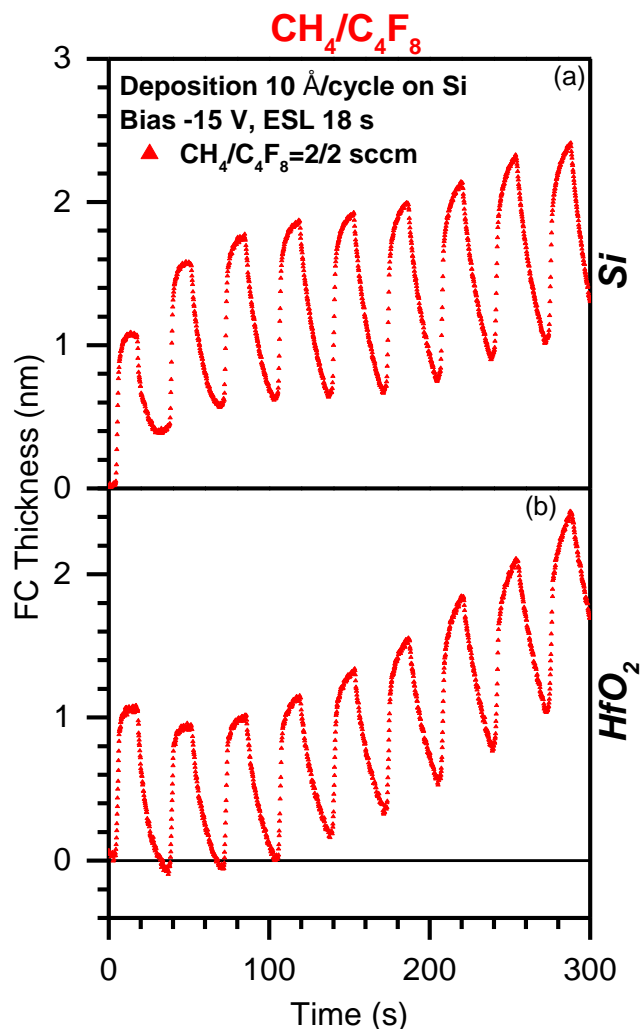


Fig. 3.5 (Color online) The evolution of the deposition film using the $\text{CH}_4/\text{C}_4\text{F}_8$ mixture on (a) Si and (b) HfO_2 , respectively. Process parameters were selected to yield a 10 \AA HFC film thickness on Si during each cycle, where were then applied to HfO_2 to study substrate-dependent deposition.

For comparison, the profiles of the deposited HFC thickness on Si and HfO_2 obtained with a CH_4/CHF_3 ALE sequence are summarized in Figs. 3.6(a) and (b). As in the previous experiments, the deposition parameters were designed to obtain $\sim 10 \text{ \AA}$ thick film on Si during initial cycles and then these conditions were applied to HfO_2 . Figure 3.6(a) shows $\sim 10 \text{ \AA}$

deposited HFC film on Si at the end of the CH₄/CHF₃ precursor injection step along with some desorption of the deposited film for the first two cycles, possibly related to changes in the chamber wall conditions.^{37, 75} The subsequent etching step resulted in a partial removal of the deposited film and some deposition accumulating on top of Si. Using the CH₄/CHF₃ mixture produced similar FC accumulation on Si as seen for the CH₄/C₄F₈ mixture.

The deposited HFC film for the CH₄/CHF₃ mixture on HfO₂ behaved differently from that seen on Si. During the first few cycles, the deposited HFC film thickness at the end of the precursor injection step was less than 2 Å. Furthermore, the deposited film underwent a desorption reaction during the purge step, as shown in Figure 3.6(b). The subsequent step applied a -15 V RF bias voltage on the substrate, which removed the residual FC film and some underlying HfO₂ layers. At the 7th and 8th cycles, the thickness of the deposited film at the end of the injection step increased to ~6 Å, and the removed deposition thickness during the purge step became less significant. During these nine cycles, a CH₄/CHF₃ mixture in the ALE sequence did not lead to the buildup of a deposited film on HfO₂ and, contrarily, resulted in a steady ER on the underlying HfO₂. We used *in situ* ellipsometry to observe a deposition yield difference on HfO₂ and Si surfaces with a 1:1 mixture of CH₄/CHF₃ in the ALE sequence.

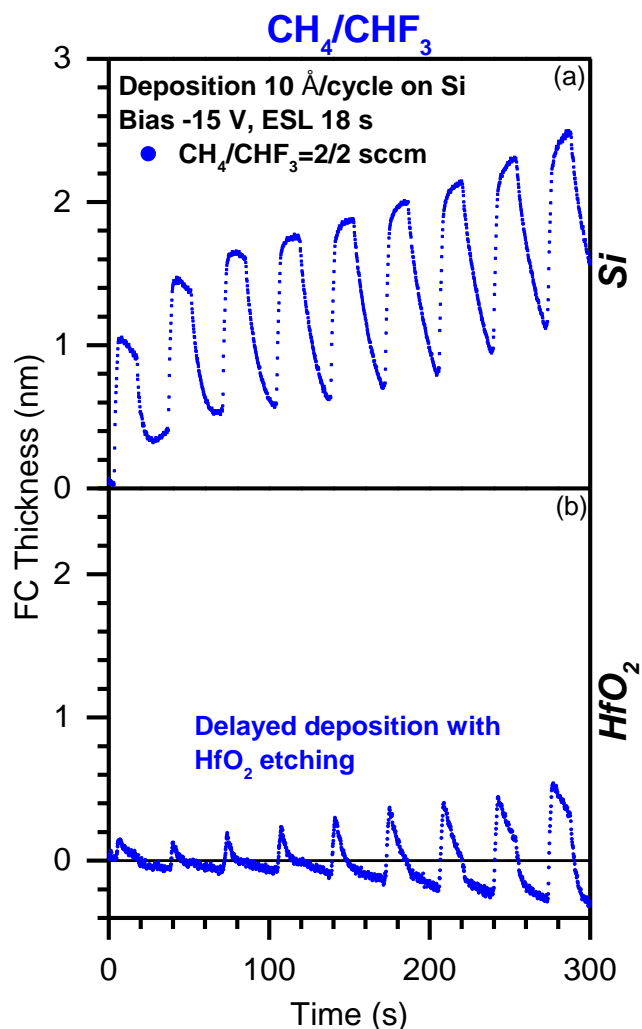


Fig. 3.6. (Color online) The evolution of deposited HFC film on (a) Si and (b) HfO₂, respectively when using CH₄/CHF₃. Process parameters were selected to yield 10 Å HFC film thickness on Si during the initial cycles and were then applied to HfO₂.

To differentiate the evolution of the deposition thickness, Figure 3.7(a) depicts the FC deposition thickness formed by the CH₄/C₄F₈ and CH₄/CHF₃ mixtures on Si and HfO₂ surfaces at the end of each deposition step. The CH₄/C₄F₈ mixture deposited a comparable film thickness of ~10 Å or more on both HfO₂ and Si surfaces in the observed twelve cycles. The CH₄/CHF₃ mixture, in comparison, did not deliver more than a 2 Å thick film on HfO₂ in the first seven

cycles. On Si, however, the same set of precursors steadily deposited more than a 9 Å thick film from the second cycle onwards. We also evaluated the deposition thickness difference between HfO₂ and Si surfaces by subtracting the HFC thickness on HfO₂ from that on Si. The evaluation shows the evolution of substrate-dependent deposition. The result is shown in Figure 3.7(b). A CH₄/C₄F₈ mixture obtained a deposition thickness difference between HfO₂ and Si of less than 1 Å within the studied twelve cycles. On the other hand, a CH₄/CHF₃ mixture revealed more than a 7 Å thickness difference between the deposited HFC film thickness on HfO₂ and Si surfaces in the first seven cycles. The difference in deposited thickness decreased over subsequent cycles, reaching 5 Å at the twelfth cycle.

Additionally, the amount of HfO₂ removed or deposition built up on HfO₂ within a cycle was measured by subtracting the film thickness at the beginning of the deposition step from the thickness at the end of the etching step. Figure 3.7(c) summarizes the thickness evolution of the deposited film and HfO₂ with CH₄/CHF₃ and CH₄/C₄F₈ mixtures, respectively. A reduction of the overall film thickness in a cycle was interpreted as an absence in the buildup of the deposited film, which corresponds to the removal of the underlying HfO₂. At the same time, a thickness increase was attributed to a deposition buildup on the HfO₂ surface. A CH₄/C₄F₈ mixture in the ALE sequence resulted in negligible HfO₂ etching in the 1st cycle and then an incremental buildup of deposition from the 2nd to 12th cycle. It is important to note that a CH₄/CHF₃ mixture in the same sequence produced an EPC corresponding to ~0.5 Å per cycle for HfO₂.

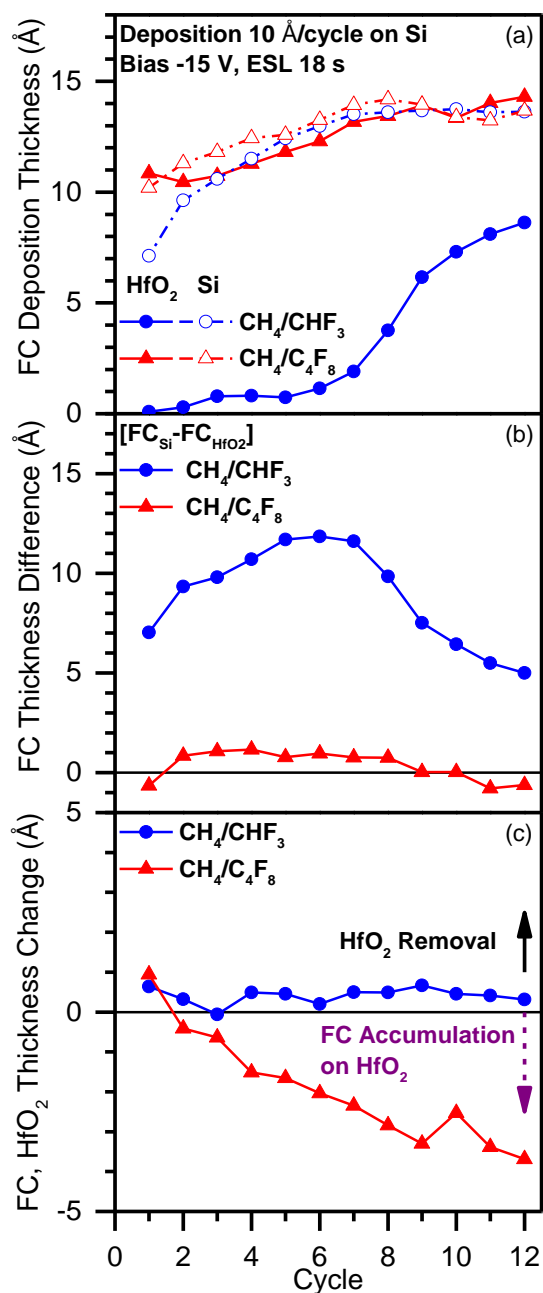


Fig. 3.7. (Color online) (a) A comparison of the deposition thickness at the end of the deposition step on HfO₂ and Si using CH₄/CHF₃ and CH₄/C₄F₈, respectively. (b) Deposition thickness differences between Si and HfO₂ with CH₄/CHF₃ and CH₄/C₄F₈, respectively. (c) The thickness evolution of the deposited FC and HfO₂ film with the selected set of precursors.

3.3.1.2 Model of Non-Selective and Selective Deposition Precursors

In situ ellipsometry showed that the selection of the precursor controls the HFC deposition behavior difference for HfO₂ and Si. The CH₄/C₄F₈ mixture deposited a similar thickness on both materials, but the CH₄/CHF₃ mixture produced a deposition thickness difference of more than 7 Å during the first nine cycles. The deposited film formed by CH₄/CHF₃ on HfO₂ desorbed, suggesting that the precursor chemistry determines substrate-dependent deposition.

XPS spectra for processed HfO₂ and Si samples by the CH₄/C₄F₈ mixture at the end of the deposition and etching steps in the 4th cycle were collected. The data of Figures 3.8(a)-(d), depict the Hf4f, C1s, O1s and F1s spectra for the HfO₂ sample with a takeoff angle of 90°. The data of Figures 8(e)-(g) show the Si2p, C1s and F1s spectra for Si at an electron takeoff angle of 90°.

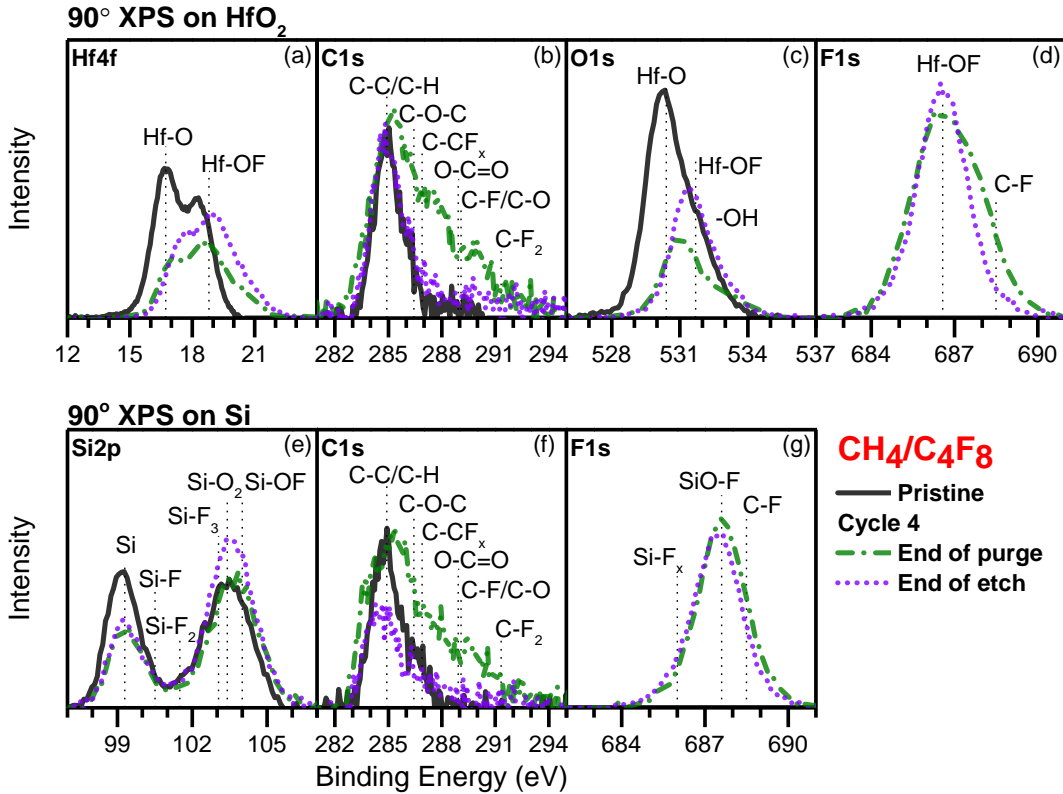


Fig.3.8 (Color online) XPS analyses on the HfO₂ and Si films treated by CH₄/C₄F₈ after the purge and etching steps, respectively, in the 4th cycle. The (a) Hf4f, (b) C1s, (c) O1s and (d) F1s spectra present the surface chemistry during each step on HfO₂. In comparison, the (e) Si2p, (f) C1s and (g) F1s spectra show the surface chemistry evolution on Si.

The XPS results are consistent with the ellipsometric data. The appearance of the C-CF_x, C-F and C-F₂ peaks in the C1s spectra in Figure 3.8(b) and (f) suggest the formation of a FC (and/or HFC) film on both HfO₂ and Si in the 4th cycle at the end of the purge step. The intensities of the C-F and C-F₂ peaks in Figures 3.8(b) and (f) had only a negligible difference, indicating that the CH₄/C₄F₈ mixture deposits a similar F/C ratio of the film on HfO₂ and Si. The following etching step shows that Ar⁺ ion bombardment contributes to an intensity reduction of the C-F peak with an intensity increase of the HfO_xF_y and SiOF peaks. This result suggests that

ion bombardment removes some deposited FC and simultaneously provides fluorine etchants from the FC film reacting with the underlying material. The C_4F_8 and C_4F_8/H_2 precursors in an ALE sequence also provide a similar reaction during the etching step, where the ion bombardment drives the underlying layer fluorination.^{5, 8, 75, 76} Importantly, the XPS spectra in Figure 8 imply that the main reactants dissociated from the CH_4/C_4F_8 mixture behave in a similar manner on HfO_2 and Si during ALE sequences.

The surface chemistry evolution of HfO_2 and Si after the CH_4/CHF_3 mixture processed at the end of the deposition and etching step of the 4th cycle was investigated by XPS analysis as well. Figures 3.9(a)-(d) present the Hf4f, C1s, O1s and F1s spectra for the HfO_2 sample at an electron takeoff angle of 90° . Figures 3.9(e)-(g) show the Si2p, C1s and F1s spectra for Si at an electron takeoff angle of 90° . The C1s spectra for the processed HfO_2 in Figure 3.9(b) show a negligible intensity of C-F peaks, indicating that no deposited film remains on the surface at the end of purge step in the 4th cycle. The etching step followed by low energy Ar^+ ion bombardment does not result in an intensity reduction of the C-C/C-H peak. Only the existence of the C-C/C-H peak provides evidence of residual ALD precursors of the initial HfO_2 .¹²² In comparison, the Si sample processed by a CH_4/CHF_3 mixture at the end of the purge step retains the C-F peaks. This result agrees with the adsorption of FC film on Si as observed by *in situ* ellipsometry. The subsequent etching step reduces the intensity of the C-C/C-H and C-F peaks, revealing a partial removal of the deposition on the Si surface. XPS spectra confirm the CH_4/CHF_3 mixture in ALE sequences that exhibits substrate-dependent deposition.

The changes in the Hf4f spectra from a pristine sample to the processed samples at the end of the purge step in Figure 3.9(a) show that the injection of a CH_4/CHF_3 mixture leads to a

fluorination reaction on HfO_2 layers. The appearance of the $\text{Hf-O}_x\text{F}_y$ peak but no intensity of the Hf-O peak in both O1s and F1s spectra at the end of the purge step, as shown in Figure 3.9(c) and (d), indicates that HfO_2 layers undergo a high degree of fluorination. The subsequent etching step with Ar^+ ion bombardment does not increase the fluorination level of the HfO_2 layers. In contrast, the Si2p and F1s spectra in Figure 3.9(e) and (g) show that Si undergoes a lower degree of fluorination at the end of the purge step. The subsequent etching step sputters the deposited FC film, which leads to the underlying Si having a higher degree of fluorination. The CH_4/CHF_3 mixture results in different surface reactions on HfO_2 and Si during the deposition step. The main dissociated reactant in plasma potentially is an important factor for the precursor deposition behavior.

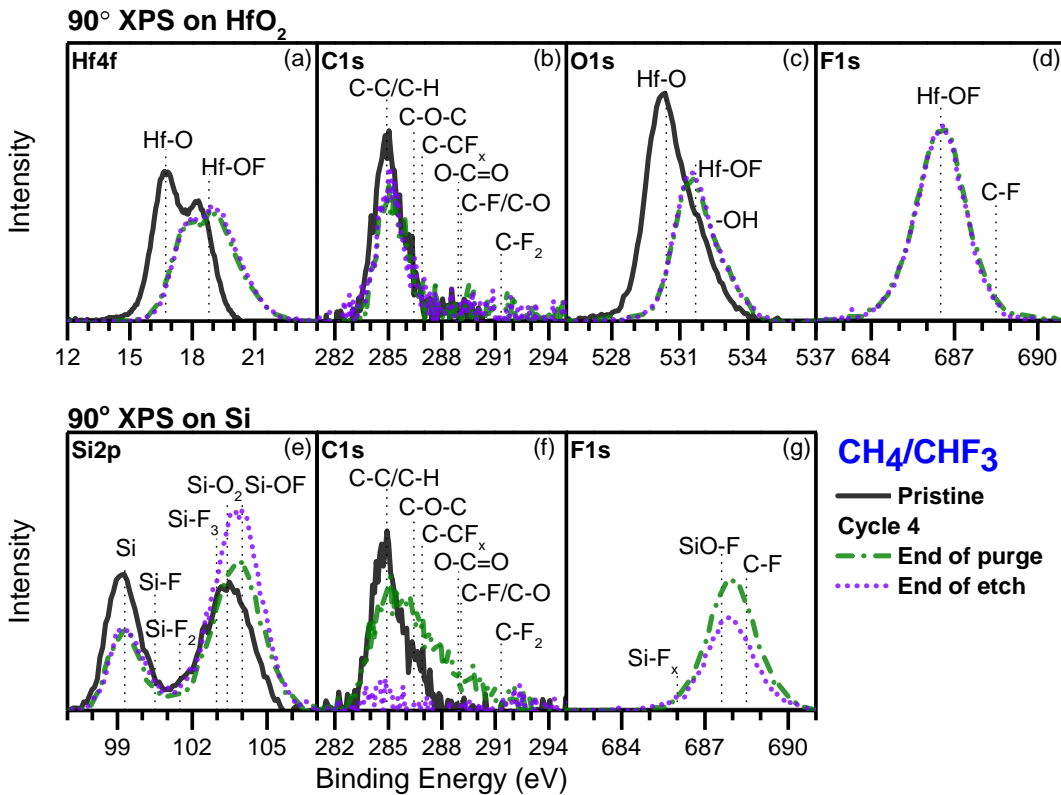


Fig. 3.9. (Color online) XPS analyses on the HfO₂ and Si films treated by CH₄/CHF₃ after the purge and etching steps, respectively, in the 4th cycle. The (a) Hf4f, (b) C1s, (c) O1s and (d) F1s spectra present the surface chemistry during each step on HfO₂. In comparison, the (e) Si2p, (f) C1s and (g) F1s spectra show the surface chemistry evolution on Si.

The removal of HfO₂ and degradation of the substrate-dependent deposition with the CH₄/CHF₃ mixture was also studied using the Hf4f, Si2p, C1s, O1s and F1s spectra, as shown in Figure 3.10. The Hf4f, O1s and F1s spectra shown in Figure 3.10(a), (d) and (e) display an intensity reduction of the Hf-O_xF_y peaks at the end of the etching step for the 4th to 8th processing cycle, indicating the removal of fluorinated HfO₂ layers. An intensity increase of the Si elemental peaks also is consistent with the removal of the top HfO₂ layers and more exposure of underlying Si layers. The C1s spectra of Figure 3.10(c) show a deposited film at the end of the deposition step of the 8th cycle, suggesting that the CH₄/CHF₃ mixture gradually loses its inherent selectivity with a deposition delay on HfO₂. Another possible cause for losing selectivity is the formation of an intermixing layer between HfO₂ and Si during the process, likely during the etching step. Overall, selective deposition is observed on Si but not on HfO₂ if a CH₄/CHF₃ mixture is used during an ALE sequence. Integrating this feature with proper etching parameters is promising with regard to achieving selective ALE of HfO₂ over Si by forming a passivation layer on Si.

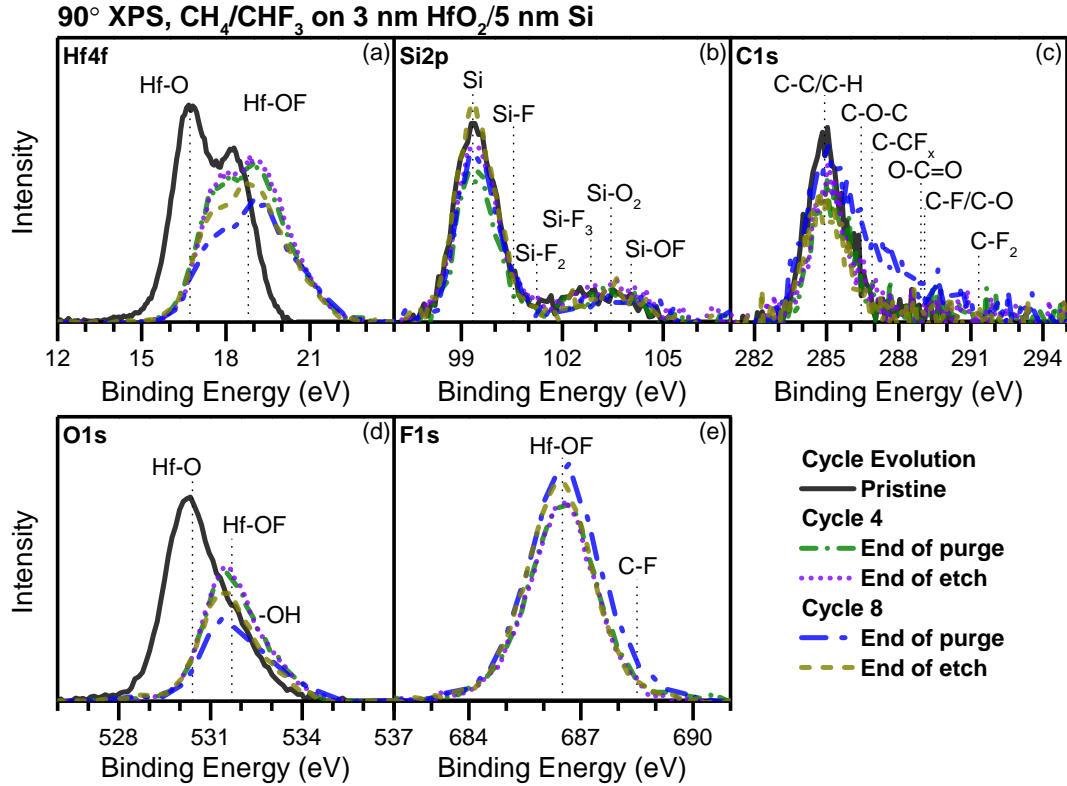


Fig. 3.10. (Color online) (a) Hf4f, (b) Si2p, (c) C1s, (d) O1s and (e) F1s XPS spectra of the sample (with the film scheme of a 3 nm ALD-HfO₂/5 nm Si/30 nm SiO₂ on a Si substrate) processed by CH₄/CHF₃ after four and eight cycles, respectively.

3.3.2 CH₄/CHF₃-Based ALE of HfO₂ with Selectivity to Si

To evaluate the etching performance of an actual material stack using substrate-selective deposition, an annealed multi-layer sample consisting of 3 nm HfO₂/10 nm Si/30 nm SiO₂ on a Si substrate was used. The purpose was to study whether the CH₄/CHF₃-based ALE process is capable of removing the top annealed HfO₂ layer with a thickness of 3 nm. The process also needed to selectively deposit a thick FC film to prevent Si etching and minimize underlying Si loss. The psi-delta map obtained by *in situ* ellipsometry using an Ar/CF₄ CW plasma with a high

substrate bias to etch back the annealed sample is shown in Figure 3.11(a). The layers were labeled top (HfO_2), intermediate (Si) and bottom (SiO_2). The ALE experiment focused on the top two layers. The experimental result is previously shown in Figure 3.7(c) suggests that the set of etching parameters applied can deliver a low EPC of HfO_2 . To improve the EPC of HfO_2 and minimize the amount of Si loss before the formation of a passivation layer, several processing parameters were optimized. These included the ratio of the CH_4/CHF_3 precursor gases to a 1:2 ratio, a -20 V RF bias voltage, and a 13 s ESL. The other parameters were the same as those given in Figure 3.4. The approach of fine-tuning the processing recipe was based on a) an increase in halogen species in the injection step, and b) a slightly higher RF bias voltage in the etching step. These changes prompted a greater EPC of etching materials, but a tradeoff was more material loss in the non-etching area before the development of a thick passivation layer. A reduced ESL, then, was utilized to accelerate the buildup rate of a deposition film on the non-etching area without having a substantial impact on the EPC of the etching area. A detailed discussion on tuning the FC-based ALE processing parameters for optimizing a passivation layer can be found in the references.^{6, 7, 30}

The psi-delta map of the optimized ALE processing for the annealed HfO_2 sample was superimposed on the etchback data and is shown in Figure 3.11(a). The ALE processing began with the etching of the top annealed HfO_2 layer. As the depletion of the top layers continued, the trajectory moved along the path corresponding to Si etching with some buildup of deposited FC. For measured trajectories along the path denoted “FC buildup on Si,” formation of a sufficiently thick HFC passivation layer on the Si surface takes place that stops the etching of underlying Si layers. In contrast to the conventional method of calculating an etching selectivity by the ER

differences of two materials within a given period, ALE selectivity can be evaluated by the amount of non-etching material loss before etching is stopped. In this work, the amount of Si loss can be used to measure the selectivity of the CH₄/CHF₃-based ALE process. In the ellipsometric model shown in Figure 3.11(b), the dense dotted line indicates the extent of Si loss after the full removal of the top annealed HfO₂ layer. The dashed line represents no further Si loss with the formation of FC deposition, while the thickness loss of the underlying Si reaches 15 Å. The results confirm that a CH₄/CHF₃-based ALE process which utilizes substrate-dependent deposition is capable of etching annealed HfO₂ with selectivity relative to Si.

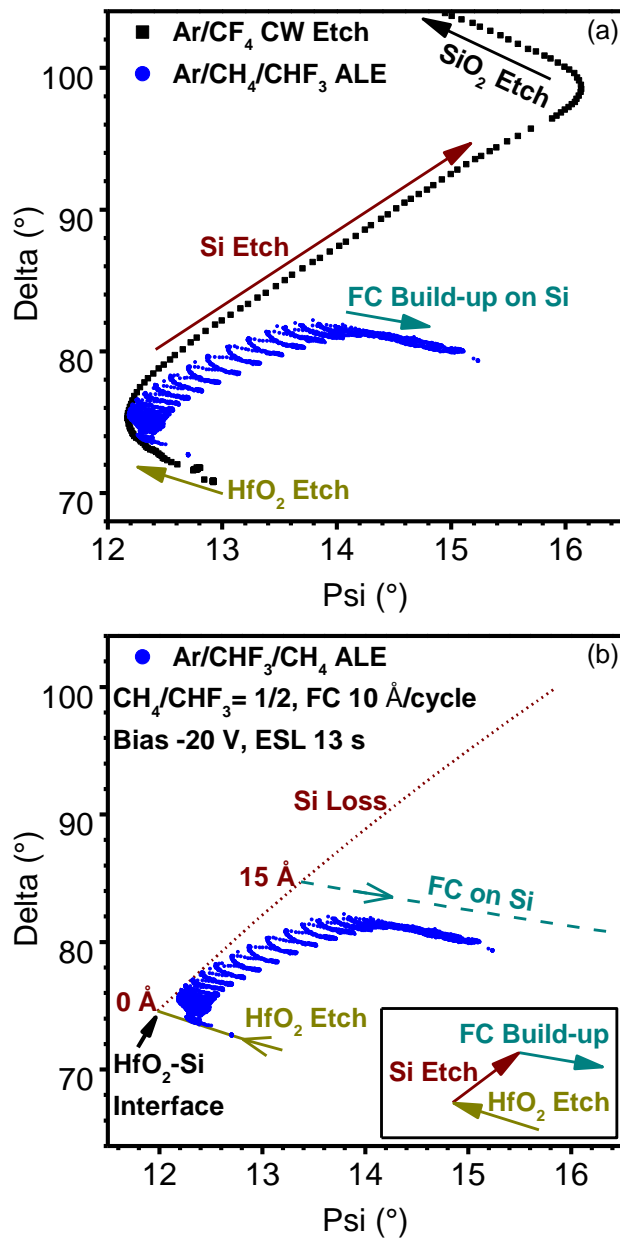


Fig. 3.11. (Color online) (a) The *in situ* ellipsometry data of Ar/CF₄ etchback on a sample (with a film scheme of 3 nm annealed HfO₂/5 nm Si/30 nm SiO₂ on a Si substrate) and a CH₄/CHF₃-based ALE process with the optimal processing parameters on the identical scheme sample. (b) Ellipsometric modeling of the etching of the top HfO₂ and underlying Si films. The dashed line

describes the formation of a FC passivation layer with a corresponding 1.5 nm Si loss before a Si etching stop occurs.

To evaluate the evolution of the ALE process on the annealed sample, the thickness change of the HfO₂ and Si layers at the end of the etching step was studied, as shown in Figure 12(a). Plasma ignition with a 10 mTorr Ar carrier gas occurs prior to the first processing cycle, likely sputtering away some surface impurities and/or HfO₂-like materials. The processing from the 1st to 13th cycle, then, delivers a steady EPC of 0.7 Å per cycle until depleting the top HfO₂ layer and reaching an interface between HfO₂ and the underlying Si layers, i.e. just etch and no over etch (0% OE). Since an etching process typically requires a certain degree of OE to ensure surface cleanliness, various degrees of OE of 0%, 20%, 50%, and 100% have been indicated and provide a measure of the corresponding Si losses. The 100% OE indicates that another 13 cycles were performed with the specimen after reaching the interface. Significantly, the Si etching stop developed after a 100% OE with a 13.7 Å Si thickness loss, and any further processing cycles did not contribute to extra Si loss.

The detailed etching profiles of the 4th to 6th cycles during the HfO₂ etching was superimposed on the profile of the 17th to 21st cycles during the underlying Si etching in order to evaluate the phenomenon of substrate-dependent deposition with a CH₄/CHF₃ mixture. The plot of this etching profile is shown in Figure 3.12(b). In the HfO₂ etching region, the precursors were deposited on the top of HfO₂ during the injection step, but the deposition underwent a desorption reaction during the purge step. The attained thickness of the deposition on HfO₂ at the end of the purge step is less than 2 Å, which facilitates the removal of the HfO₂ layer by utilizing low energy Ar⁺ ion bombardment. In comparison, the deposited film continuously builds up on top of

the Si during the purge step, attaining a thickness on the surface of more than 10 Å. A thick deposited FC film buffers the Si layer from Ar⁺ ion bombardment during the etching step and contributes to the formation of a passivation layer. The substrate-selective deposition through a CH₄/CHF₃ mixture on HfO₂ and Si surfaces realizes the ALE selectivity.

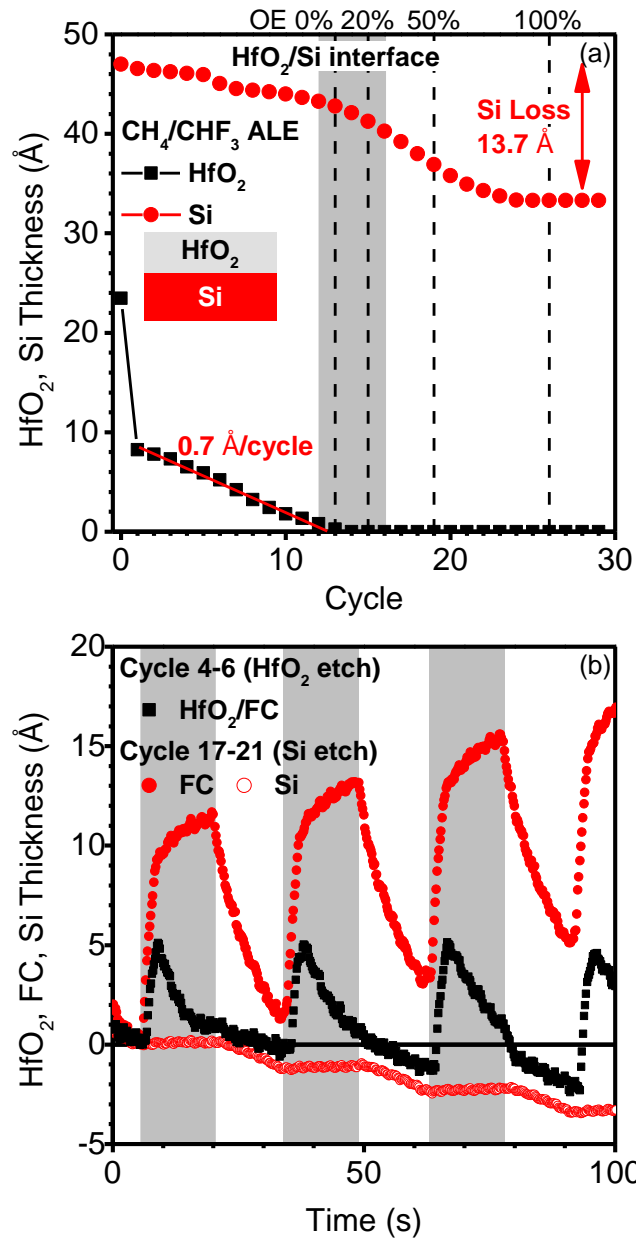


Fig. 3.12. (Color online) (a) HfO₂ and Si thickness at the end of each ALE cycle using a CH₄/CHF₃-based ALE process. (b) The profile of the HfO₂ and FC thickness in the 4th to 6th cycles of the HfO₂ etching region was superimposed on the profile of the FC and Si thickness in the 17th to 21st cycles of the Si etching region.

XPS spectra of Hf4f, Si2p, C1s, O1s and F1s were also obtained to establish if the sample surface has any residual HfO₂ remaining at just etch (0% OE). The detailed data is shown in Figure 3.13. After processing, the Hf-O peaks in the Hf4f and O1s spectra disappeared, and a greater intensity of elemental Si is observed in the Si2p spectra. The transformation of the peak intensities indicates that the substrate surface has no HfO₂ remaining in respect to more exposure of the underlying Si. A few HfO_xF_y peaks, observed in the Hf4f, O1s and F1s spectra, are considered to be an etching byproduct on the surface. The thickness of the HfO_xF_y layer can be calculated using angle-resolved attenuation modeling, which utilizes an attenuation of Si2p photoelectrons by the top HfO₂ or HfO_xF_y layer. The attenuation equation¹²⁵

$$d_{HfO_2} = \lambda \left[\frac{\cos \varphi \cos \varphi'}{(\cos \varphi - \cos \varphi')} \right] \ln \left(\frac{I_{Si2p}}{I'_{Si2p}} \right) \quad (1)$$

was used, with the electron inelastic mean free path (IMFP) in the HfO₂ film λ equal to 21.7 Å.¹²⁶ The calculated thickness of the unprocessed HfO₂ layer in a pristine sample is ~29 Å, whereas that of the HfO_xF_y etching byproduct on the substrate at the end of the etching process (0% OE) is ~7 Å. The processed sample surface typically also shows etching byproducts, including carbon and SiOF intermixing layers. The intermixing layer dramatically affects the Si2p intensity and reduces the accuracy of the calculated byproduct thickness using the attenuation model. The real thickness of the HfO_xF_y byproduct on Si is expected to be thinner

than the calculated value. The XPS spectra show that the CH₄/CHF₃-based ALE process can substantially remove the annealed HfO₂ layer with an initial thickness of ~29 Å.

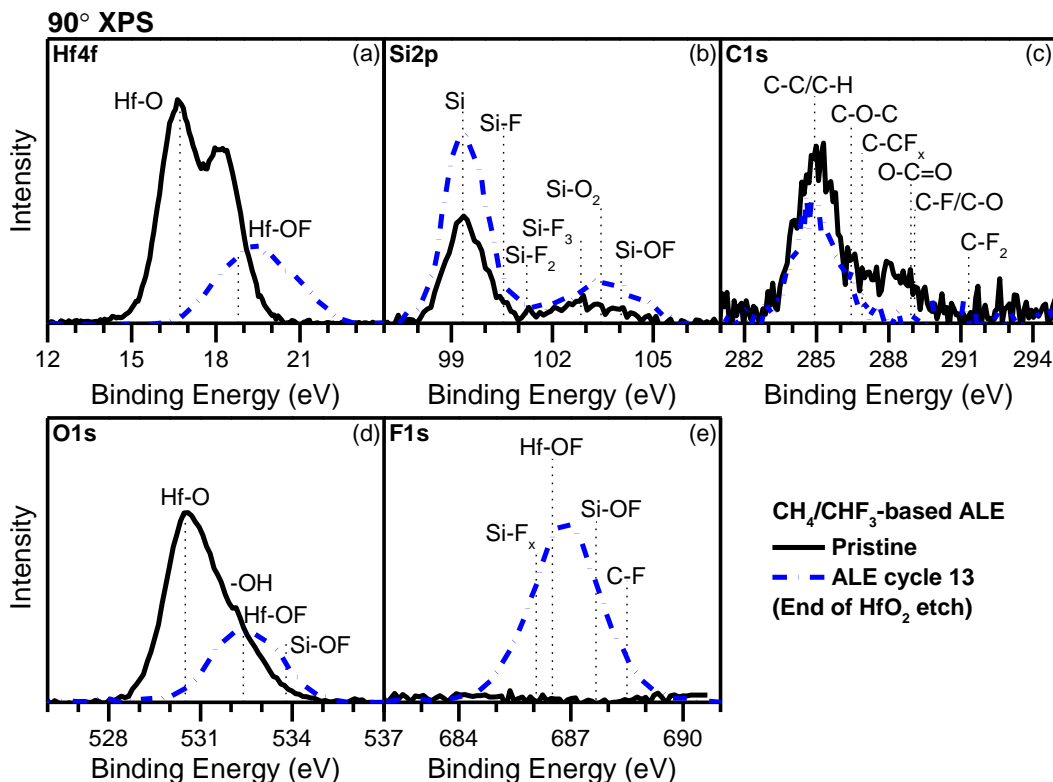


Fig. 3.13. (Color online) XPS spectra comparing a pristine sample with a treated sample by a CH₄/CHF₃-based ALE process after 13 cycles at the end of the HfO₂ etching region (no over-etching). The spectra include (a) Hf4f, (b) Si2p, (c) C1s, (d) O1s and (f) F1s.

3.3.3 Discussion

A comparison of the deposition behavior of HFC films on HfO₂ and Si surfaces shows that a CH₄/CHF₃ mixture exhibits substrate-dependent deposition, but a CH₄/C₄F₈ mixture does not. The current work shows that the CH₄/CHF₃-based ALE process can etch annealed HfO₂ with selectivity to Si. To understand this difference, it is necessary to investigate the mechanism

of substrate-selective deposition, particularly the plasma dissociated radical and surface interactions. This section will begin with a review of dissociated radicals from C_4F_8 and CHF_3 gases and the effect of CH_4 additives. Then, a surface reaction model based on XPS analysis is proposed to explain the different process outcomes seen for the various precursor sets that were examined for Si and HfO_2 . A summary of our experimental results with implications for the field of ASD will be discussed in the final part of this section.

We postulate that the dissociated species of C_4F_8 and CHF_3 gases during the precursor injection step regulate surface reactions, in particular, F, CF, CF_2 and CF_3 radicals, resulting in surface fluorination and/or FC deposition. CF_x ($x = 1-3$) radical densities in plasma control the deposition yield on the substrate surface, so a higher radical density likely contributes to a higher deposition yield.^{9, 127, 128} Schaepkens *et al* estimated CF and CF_2 radical densities using the apparatus used in the current work for C_4F_8 and CHF_3 plasmas by employing infrared diode laser absorption spectroscopy (IRLAS).¹¹⁷ In their work, C_4F_8 plasma produced CF and CF_2 radical densities with partial pressures of 0.065 mTorr and 2.475 mTorr, respectively. They used a flow rate of 10 sccm, chamber process of 13 mTorr, and inductive power of 600 W. In comparison, the CHF_3 plasma produced CF and CF_2 radical densities with partial pressures of 0.041 mTorr and 0.99 mTorr, respectively, under the same inductive power and gas flow rate as the above-mentioned C_4F_8 plasma but at a reduced chamber pressure of 10 mTorr. Since the partial pressure of a dissociated radical is proportional to the radical density, we can infer that the average CF and CF_2 radical densities in the C_4F_8 plasma are higher than that those in the CHF_3 plasma. Similar to Schaepkens's experiments, Miyata *et al* also estimated the CF_x ($x = 1-3$) radical density in electron cyclotron resonance (ECR) plasmas with C_4F_8 and CHF_3 gases by

IRLAS.¹²⁹ They found results consistent with Schaepkens that the CF and CF₂ radical densities in the C₄F₈ plasma under a roughly similar processing condition are on the range of 10¹¹-10¹² cm⁻³ and 10¹²-10¹³ cm⁻³, respectively. The CHF₃ plasma dissociated to produce lower CF and CF₂ radical densities than those produced in the C₄F₈ plasma as well. Additionally, the CF₃ radical density in the C₄F₈ plasma at the microwave power of 200 W increased to be on the order of 10¹³ cm⁻³, whereas that in the CHF₃ plasma was on the order of 10¹² cm⁻³.¹²⁹ The radical density difference between these two plasmas is possibly a result of the dissociation cross-section of C₄F₈ being larger than that of CHF₃.^{129, 130} This difference leads to the C₄F₈ plasma showing a higher degree of dissociation. As a result, the C₄F₈ plasma provides a relatively high density of CF_x (x = 1-3) radicals onto the substrate surface.

The above-mentioned radical density measurements were conducted without a carrier gas. Since our studies of the ALE processing sequence, including the deposition step, uses a 50 sccm Ar carrier gas, the use of carrier gas may cause a deviation from these radical density measurements. Li *et al* compared the chemical composition of the deposition films from C₄F₈ and C₄F₈/80% Ar plasmas by using XPS.¹³¹ The C1s spectra revealed that the Ar carrier gas contributed to a small reduction of the C-F₂ intensity along with a slight increase in C-CF_n/C-O intensities for a 300 nm thick deposition film. Metzler *et al* studied the FC deposition yield using Ar/C₄F₈ and Ar/CHF₃ on Si and SiO₂ in an ALE sequence.^{5, 7} Their results showed that under the same amount of precursor injected in a cycle, an Ar/C₄F₈ gas chemistry deposits a film three to five times thicker than an Ar/CHF₃ gas chemistry. Ar carrier gas in ALE sequences results in a slight impact on the composition of the deposited film, but it does not affect the relative behavior differences between C₄F₈ and CHF₃ plasmas.

An additional factor affecting surface reactions is the adsorption of F radicals which results in surface passivation via surface fluorination reactions. Hebner *et al* measured the SiF radical density in inductively driven discharges containing C₄F₈ and CHF₃ gases through laser-induced fluorescence (LIF).¹³² This approach allowed the researchers to measure the number of F radicals interacting with the Si wafer and forming SiF etching byproducts. The relative SiF density generated by CHF₃ was four times more than that generated by C₄F₈ under the processing conditions of 200 W coil power, 10 mTorr pressure, and no substrate bias. These findings suggested that the C₄F₈ plasma tends to form a FC polymerization layer due to a relatively high CF_x (x = 1-3) radical density. The CHF₃ plasma, on the other hand, produces a high density of F radicals fluorinating the substrate surface.

A key issue concerning the effect of adding CH₄ to Ar/C₄F₈ and Ar/CHF₃ plasmas concerns the question of whether or not CH₄ can serve as a fluorine scavenger in an ALE sequence and may remove fluorinated HfO₂. The electron impact in plasma induces CH₄ dissociation, producing hydrogen and hydrocarbon (HC) radicals, such as H, CH, CH₂, CHF₃ and C₂H₅.¹³³⁻¹³⁶ The dissociated H species easily react with the F radicals originating from FC and HFC precursors to form HF products. Therefore, the relative concentration of CF_x (x = 1-3) radicals is significantly increased with a 50% CH₄ addition to C₄F₈ and CHF₃ plasmas.¹³⁷ For the deposition film, the substrate bias power is related to the C/H ratio.¹³⁸⁻¹⁴⁰ Fox-Lyon *et al* showed that in an Ar/CH₄ plasma a high substrate bias power provides the carbon-rich deposition film.^{141, 142} Since our ALE sequences do not apply any bias during the deposition step, CH₄ additives result in a hydrogen-rich deposition film. These hydrogen-rich depositions enable a removal pathway of fluorinated HfO₂ by forming HfCH_x⁺ (x = 0-4) and HfH_xF⁺ (x = 0-2) volatile

products.¹¹⁵ Without these products, using a -15 V substrate bias power in the etching step does not meet the energy threshold of sputtering annealed HfO₂ and/or fluorinated HfO₂.

To understand the behavior of CH₄/C₄F₈ and CH₄/CHF₃ mixtures on HfO₂ and Si, it is necessary to establish a plasma-surface interaction model that includes the major dissociated radicals. The XPS spectra in Figures 3.8 and 3.9 are consistent with reactants that determine the result of the surface reactions. When using a CH₄/CHF₃ mixture, fluorination of HfO₂ takes place during the Ar/CHF₃/CH₄ deposition step and produces a chemically stable compound, fluorinated HfO₂. On the other hand, Si produces volatile SiF_x with incoming F, and thus allows fluxes of FC and HC species to deposit HFC films on the Si surface. In the case of a CH₄/C₄F₈ mixture, the XPS spectra in Figure 8 suggest a low degree of fluorination of the underlying HfO₂ and Si layers, which enables the primary flux of FC and HC species to deposit on both surfaces. Figure 3.14 summarizes the surface reaction for HfO₂ and Si with the CH₄/CHF₃ and CH₄/C₄F₈ mixtures in an ALE process.

In accordance with our experimental results, many studies suggest that a fluorinated surface hinders the adsorption of a fluorine-containing precursor.^{106, 143, 144} For example, a pre-treatment consisting of a NF₃ plasma on a SiO₂ film suppresses the deposition of tungsten hexafluoride (WF₆) nucleation seeds in a tungsten chemical vapor deposition (W-CVD) process.¹⁴³ In a W-ALD process, Kalanyan *et al* found that adding H₂ during the WF₆ step process promoted the fluorination of SiO₂ due to the formation of HF gas. The fluorinated SiO₂ layer reinforced the deposition selectivity of Si over SiO₂.¹⁴⁴ However, the approach of using fluorination passivation on the non-growth area should consider the volatility and chemical

stability of the fluorinated surface in order to minimize the undesirable adsorption of nucleation seeds.⁸⁹

One of the shortcomings of substrate-selective deposition is that the selectivity is gradually degraded as the number of nucleation sites on the non-growth area increases.¹¹² An inherent deposition selectivity is based on the nucleation rate differences on various substrates, where non-growth areas have an incubation time for the adsorption of the nucleation seed.^{145, 146} When the number of seeding site reaches the point where it overcomes the energy barrier of growth on the non-growth area, the growth reaction starts to take place, and the deposition is no longer material selective. A similar mechanism is indicated in the case of an Ar/CH₄/CHF₃ mixture interacting with the HfO₂ surface. Figure 3.7 shows that after seven cycles, the deposited thickness on HfO₂ at the end of the injection step is dramatically increased, suggesting that a greater number of carbon nucleation sites on the HfO₂ surface in the later cycles enables adsorption of HFC reactants. This change results in a loss of material selectivity in an ALE process.

To reinforce deposition selectivity, research on AS-ALD has introduced the concept of a super-cycle that introduces an etching step to enhance selective deposition by restoring surface conditions for the non-growth areas. For example, selective epitaxial growth (SEG) of Si by chemical vapor deposition (CVD) uses an etchant gas, typically HCl, added to the precursor mixture to remove undesired nucleation seeds on SiO₂ non-growth areas.¹⁴⁷⁻¹⁵⁰ It is essential for future studies to identify a way to restore an incubation time on the non-growth area, which reinstates the etching selectivity for ALE.

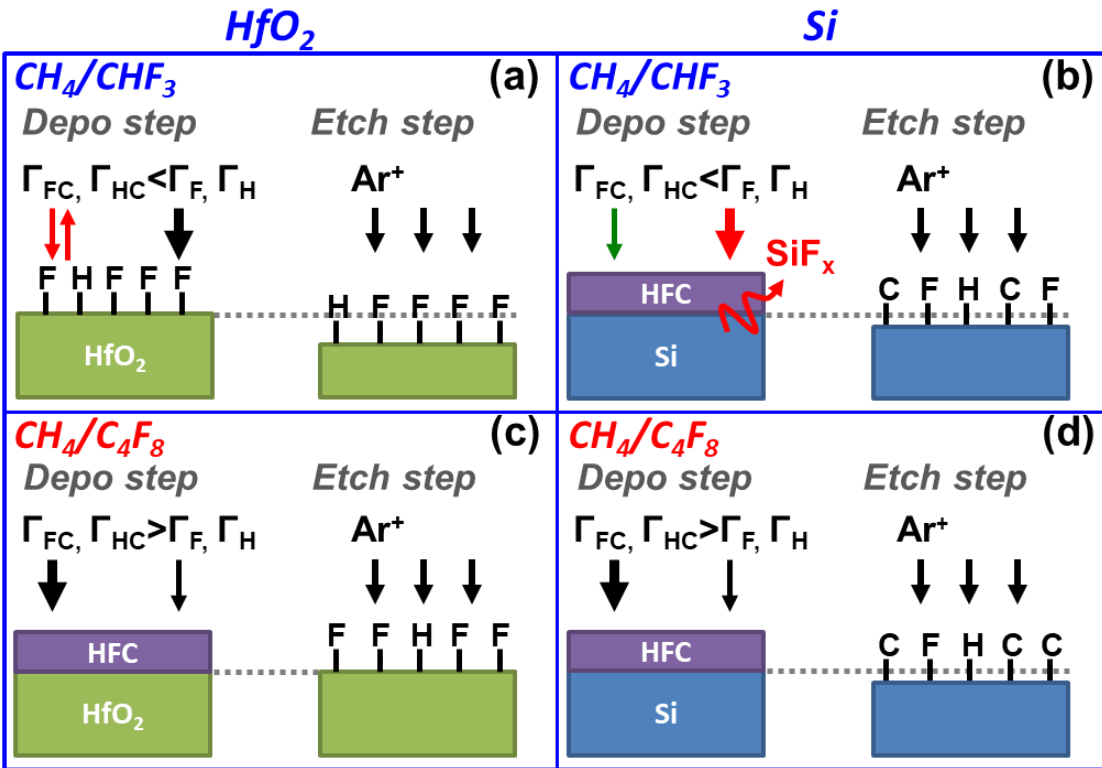


Fig. 3.14. (Color online) illustrates the surface reaction using CH₄/CHF₃ and CH₄/C₄F₈, respectively, on HfO₂ and Si, which is consistent with the XPS data shown in Figure 8 and 9. (a) A CH₄/CHF₃ mixture during the deposition step generates a high flux of fluorine, resulting in a highly fluorinated HfO₂ surface which temporarily suppresses the FC deposition. The following step utilizing low energy Ar⁺ ion bombardment facilitates the etching of fluorinated HfO₂. (b) For Si, a mixture of CH₄/CHF₃ is able to deposit a ~10 Å film due to silicon functioning as a reducing agent to remove excess reactive fluorine. In the etching step, the deposited film buffers Si layers from the ion bombardment, with some H, C, and F remaining on top of the Si. (c) and (d) A CH₄/C₄F₈ mixture deposits a comparable thickness (~10 Å) on both HfO₂ and Si surfaces due to a high flux of FC and HC species carrying a similar reactivity to both materials. In the etching step, low energy Ar⁺ ion bombardment sputters the deposited film and prompts the ion-enhanced fluorination of underlying materials. As a result, a CH₄/CHF₃ mixture on HfO₂ and Si is able to provide a substrate-dependent deposition.

3.4 Summary and Conclusions

This work studied the deposition behaviors of two precursor mixtures, CH₄/C₄F₈ and CH₄/CHF₃, injected into a steady Ar plasma on HfO₂ and Si surfaces. The results of *in situ* ellipsometry and XPS measurements show that at the end of the purge step, the CH₄/C₄F₈ mixture produces deposited films on both HfO₂ and Si of comparable thickness. In contrast, the use of CH₄/CHF₃ mixtures shows substrate-selective deposition between HfO₂ and Si. The deposited film generated by CH₄/CHF₃ on HfO₂ desorbs during the purge step, with negligible HFC film deposition remaining on the HfO₂ surface at the end of the purge step. For Si, the CH₄/CHF₃ mixture deposits a FC film with a thickness of more than 10 Å after the purge step.

To understand the deposition behavior difference, a surface reaction model based on XPS analysis of the surface conditions was proposed. This model postulates that the CH₄/C₄F₈ mixture produces a high density of CF_x (x =1-3) and CH_y radicals, which leads to a comparable deposition thickness on HfO₂ and Si surfaces. In contrast, the CH₄/CHF₃ mixture generates a higher density of F radicals and a lower density of FC precursors. These F radicals enable the fluorination reaction on the HfO₂ surface, which suppresses the adsorption of FC and HC species. On the Si surface, the effect of F radicals is mitigated by the formation of volatile SiF_x products, so the FC and/or HC film can deposit freely. The deposition behavior difference between the CH₄/C₄F₈ and CH₄/CHF₃ mixtures reveals that the chemical structure of the precursor used in ALE sequences can dictate substrate-selective deposition.

Based on substrate-selective deposition with the integration of low energy Ar⁺ ion bombardment, an innovative ALE process with a CH₄/CHF₃ mixture allows us to develop an etching selectivity of annealed HfO₂ relative to Si. We optimized the processing parameters,

including a higher F amount in the injection step, an increased bias RF voltage, and a reduction of the ESL, for a greater EPC of HfO₂. The resulting process is able to etch through a ~29 Å annealed HfO₂ film with the formation of a passivation layer on Si. The measured Si thickness loss is less than 13.7 Å before the Si etching stop occurs. The XPS spectra are consistent with the results observed by *in situ* ellipsometry at the interface between the fully depleted top HfO₂ and just exposed underlying Si. The developed CH₄/CHF₃-based ALE process can substantially remove the annealed HfO₂ layer with an initial thickness of 29 Å.

The implementation of substrate-selective deposition with a combination of low energy Ar⁺ ion bombardment allows for realizing selective ALE. The deposition becomes inherently less selective with the adsorption of nucleation seeds on the etching area, which degrades the performance of an ALE process. It is important for future studies to focus on an approach that restores the surface state to reestablish etching selectivity.

3.5 Acknowledgments

Substrates were produced in Microelectronics Research Laboratory (MRL) at T. J. Watson Research Center in Yorktown Heights, NY. The authors gratefully acknowledge the financial support of this work by Semiconductor Research Corporation (2017-NM-2726). We thank Dr. A. Knoll, Dr. P. Luan, A. Pranda and Y. Li for helpful discussions and collaboration. The authors also thank H.C. Chen from Taiwan Semiconductor Manufacturing Company, H. Cottle, A. Metz and A. Raley from Tokyo Electron Limited, and J. Tan and S. Odunuga from Intel for valuable suggestions on this work.

Chapter 4: SiO₂ Surface Evolution under CF₄/O₂ Remote Plasma and Co-Introduction of Remote Plasma and Electron Beam

Manuscript in preparation

K. Y. Lin, C. Preischl, C. F. Hermanns, D. Rhinow, H.-M. Solowan, T. Hofmann, B Michael, K. Edinger, and G. S. Oehrlein

K.Y. Lin contributed to the design and conduction of the research, to the analysis of the experimental results, and to the writing of the manuscript.

All authors discussed the results, commented on and made changes to the manuscript.

ABSTRACT

Electron-based surface activation of surfaces functionalized by remote plasma appears like a flexible and novel approach to atomic scale etching and deposition. Relative to plasma-based dry etching which uses ion bombardment of a substrate to cause controlled material removal, electron-beam induced etching (EBIE) is expected to reduce surface damage, including atom displacement, surface roughness, and undesired material removal. One of the issues with EBIE is the limited number of chemical precursors that can be used to functionalize materials. In this work we demonstrate a new configuration that was designed to leverage the possibility for flexible surface functionalization using a remote plasma source, and combining this with an

electron beam (EB) source the purpose of which is to remove the chemically reacted surface layer through electron-stimulated desorption (ESD). This article describes an experimental configuration consisting of a remote plasma source and an electron flood gun for enabling electron beam-induced etching of SiO₂ with Ar/CF₄/O₂ precursors. We evaluated the parametric dependency of the processing parameters of the flood gun, including electron energy and emission current (EC), and of the remote plasma source, including radiofrequency (RF) source power and flow rate of CF₄/O₂, to SiO₂ etching rate (ER). Additionally, two prototypical processing cases were demonstrated, by simultaneously or temporally assembling the remote plasma treatment and the electron beam irradiation steps, to validate the performance in etching applications, such as photomask repair and atomic layer etching (ALE) of SiO₂. Surface characterization results that provided mechanistic insights on these processes are also presented and discussed.

4.1 Introduction

Plasma etching utilizes the ion-neutral synergy effect to achieve pattern transfer on a substrate, and is extensively used in semiconductor manufacturing.^{11, 111, 151-153} As the feature size of transistors has shrunk to the sub-10 nm scale, the conventional continuous-wave (CW) plasma process no longer meets the processing requirements, including profile control and etching selectivity. The recent development of plasma-enhanced atomic layer etching (ALE) that temporally separates a deposition step and an ion bombardment step can improve etching selectivity, such as Si over SiO₂^{3, 4, 33, 74} and SiO₂ over Si₃N₄^{5, 30, 76, 77, 154, 155}. Several works in the literature present detailed reviews of the recent developments in plasma-enhanced ALE.^{12, 14-16, 87, 155} However, plasma intrinsically develops a sheath potential on a substrate, resulting in inevitable material losses and defect formation. C₄F₈-based ALE, for example, develops a -15 V sheath potential on the substrate, leading to SiO₂ and Si losses at the beginning of the deposition step.⁷ Other studies have identified that defects can be created on Si and soft materials exposed to Ar plasma, including atom displacement^{33, 156-158} and the formation of another surface layer that decreases pattern transfer fidelity.¹⁵⁹⁻¹⁶¹ Therefore, the direct plasma is not ideal for high fidelity pattern transfer. There is a need to utilize an alternative approach enabling desorption of a reacted layer without damage.

Exploiting an electron beam (EB) in combination with a flux of chemical precursors for material etching is a feasible approach for mitigating plasma damage because the mass of electrons is orders of magnitude smaller than the mass of ions. Electron beam-induced etching (EBIE) is based on EB irradiation of the surface which has physically or chemically adsorbed chemical etchants to promote electron-simulated desorption (ESD).^{19, 66, 162-164} Coburn and

Winters demonstrated that the combination of EB and XeF₂ removes SiO₂ and Si₃N₄.⁵⁷ Other studies investigated different precursors for EBIE of metals¹⁶⁵⁻¹⁶⁷, carbon¹⁶⁸⁻¹⁷⁰, germanium¹⁷¹,¹⁷², and Si-based materials^{20, 57, 66, 173-176}. A comprehensive review of the development in EBIE is listed.^{21-23, 177, 178} One challenge is that the limited number of chemical precursors that can be used for surface functionalization in EBIE as compared to the number of available etchants that are combined for “plasma chemical etchants” in plasma etching to achieve selective material removal. There are two limiting factors: 1) few precursors can adsorb and cover the substrate surface,²⁰ and 2) the adsorbates can form volatile etching products under EB irradiation.²¹⁻²³ Additionally, gas-phase hydrocarbon impurities in the reactor may participate in surface reactions and stop desorption of etching products.^{21-23, 177} To achieve damage-free pattern transfer and expand available etchants in EBIE, we evaluated a new approach that integrates a remote plasma source with an electron flood gun. As shown in Fig 4.1, a remote plasma source is used to generate a flux of neutrals, especially radicals, for surface functionalization, and a flood gun is used to emit an electron flux that stimulates the removal of the modified layer. By using a remote plasma it is possible to improve the surface adsorption of gas-phase precursors on a specimen and directly regulate the chemistry of surface functionalization, e.g. by changing the relative gas flow rates of CF₄ and O₂. The flood gun and remote plasma can be employed simultaneously or separately. With the assistance of remote plasma, this experimental configuration can offer more available etchants for EBIE.

This article begins with a description of co-introduction of EB and remote plasma for SiO₂ etching, and then describes screening experiments aimed at evaluating the dependence of SiO₂ etching rate (ER) on processing parameters. Both plasma etching and EBIE have a

comprehensive understanding of SiO_2 etching, which is used as a basis for examining our concept. We explore the parametric dependencies on flood gun and remote plasma operating variables of the SiO_2 ER. *In situ* ellipsometry is used to monitor surface modification and etching. We also study a sequential treatment that involves remote plasma-based surface treatment and subsequent EB irradiation, and characterize the surface chemistry evolution. Since the EB only irradiates a portion of the sample, whereas the remote plasma modifies the whole surface, a comparison of the surface area portions with and without electron irradiation can be used to clarify the influence of EB bombardment on surface chemistry. For this we employ small area and angle-resolved XPS analyses for surfaces with different electron fluxes. The characterization results provide a fundamental understanding of the new experimental configuration.

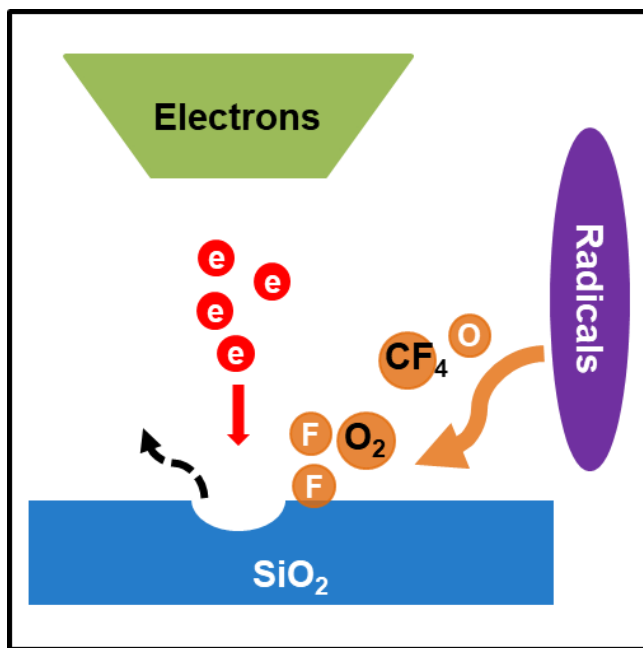


FIG. 4.1. (Color online) Schematic diagram of the concept of co-introduction of radicals and electrons onto a SiO_2 surface to enable a novel etching process.

4.2 Experimental

The experiments were conducted in a vacuum reactor, comprised of a flood gun on the top of the chamber and an electron cyclotron wave resonance (ECWR) remote plasma source on the side (Fig. 4.2(a)). The base pressure of the reactor before a process is at 1×10^{-7} Torr, and the reactor pressure with precursor injection is raised to 1.8 mTorr. The flood gun used is a commercial Kimball Physics EGA-1012 Electron Gun with a standard yttria-coated disc cathode. The cathode at room temperature can be exposed to atmospheric gases without damage, and the minimum vacuum to run this cathode is 10^{-5} Torr. A differential pump unit (DPU) was designed and installed to improve the vacuum level in the flood gun chamber. The DPU bottom was attached to a custom-made pressure-limited aperture (PLA), establishing a pressure ratio between the reactor (1×10^{-3} Torr) and the flood gun chamber (1×10^{-6} Torr) of about 1000. The remote plasma source consists of a COPRA DN160 ECWR plasma source running at 13.56 MHz radiofrequency (RF) with a neutralization plate.¹⁷⁹ The neutralization plate was made by electrically grounding an aluminum plate covered with Kapton tape and a 4-inch diameter quartz plate at the center to mitigate plasma erosion. The neutralization plate is to filter out the ions generated by the ECWR plasma source, allowing only neutrals to diffuse into the reactor. Prior studies have presented a detailed description of this remote plasma source^{180, 181} and the characterization of etching results on Si-based materials¹⁸²⁻¹⁸⁵. The ECWR effect requires an additional static magnetic field, exploiting the interaction of an electromagnetic wave with plasma.¹⁷⁹ Most experiments were conducted at a 400 W RF source power and 1.8 mT static magnetic fields to the ECWR system. A 200-second pretreatment that introduced both flood gun

and remote plasma was applied to each sample for removing adventitious carbon and surface contamination before a processing step. Typical processing parameters were for the remote plasma use of an Ar/CF₄/O₂ flow rate of 10/1/4 SCCM, and for the flood gun use of 1000 eV electrons at 0.5 mA emission current (EC) and a 100 V control grid. The sample holder is made of electrically grounded stainless steel with the backside cooled by circulating water at 10 °C.

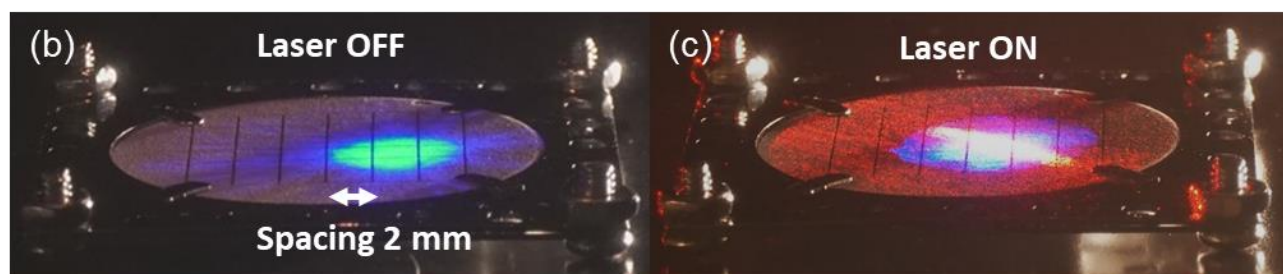
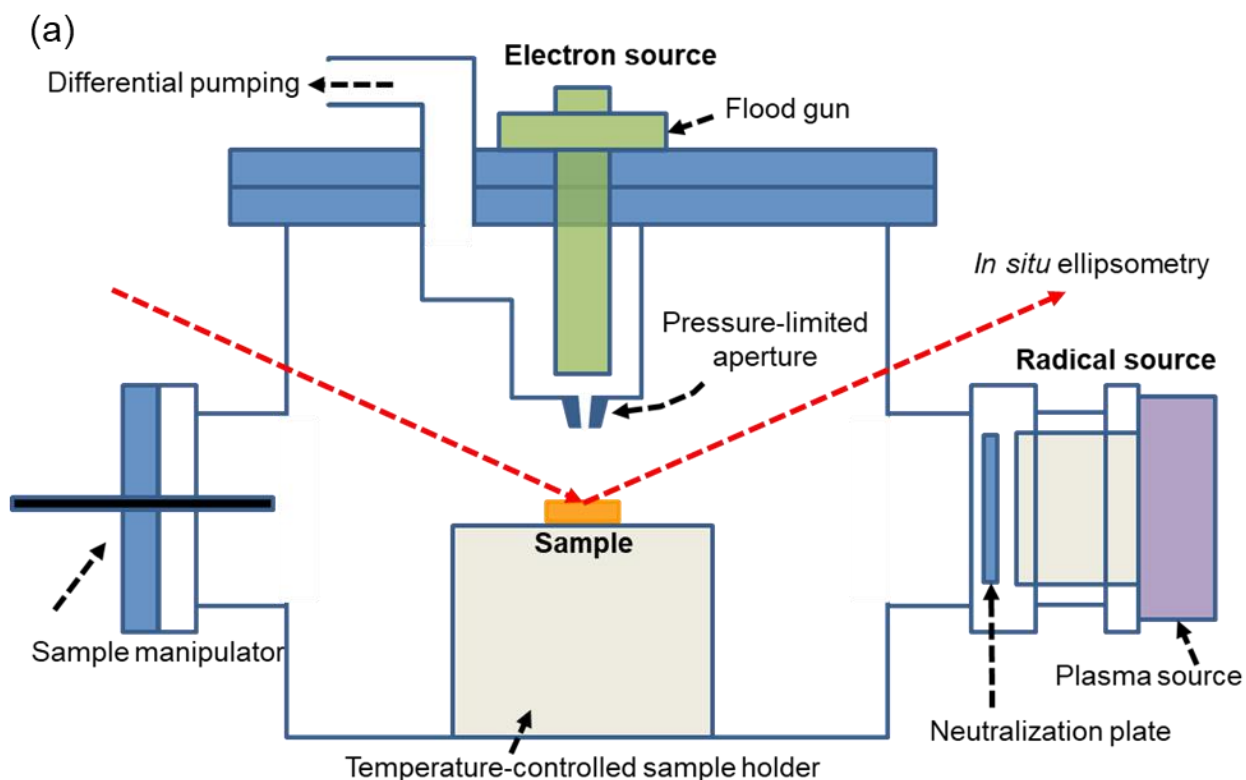


FIG. 4.2. (Color online) (a) Schematic diagram of the apparatus integrated an electron source and a radical source. Picture of the calibration phosphor screen under (b) a 1000 eV electron beam with the control grid voltage of 100 V and (c) the electron beam and *in situ* ellipsometry laser.

The flood gun consists of a cathode, a control grid, and an anode for independent control of electron energy, EC, and beam convergence angle. The voltage between cathode and anode regulates the electron energy, ranging from 5 eV to 1000 eV. Cathode temperature governs the flux of emitted electrons, where EC is proportional to working temperature. A high working temperature, however, accelerates the evaporation rate of the yttria coating and reduces the filament lifetime. The maximum EC under 1000 eV electron energy can emit a current up to 1.5 mA. Our experiments employed a 0.5 mA or lower EC to extend the lifetime of the flood gun. Calibration of the beam diameter on a substrate was done by utilizing a customized phosphor screen with 2 mm spacing grids from Kimball Physics. The in-vacuum length of the firing unit was adjusted for meeting a 38.3 mm working distance from the flood gun outlet to a substrate, so a 1000 eV EB with the maximum grid voltage, 100 V, produced a ~5.5 mm beam diameter on the calibration screen (Fig. 4.2(b)). In the case of studying the dependency of electron energies on etching performance, the control grid voltage was adjusted accordingly to keep the spot size constant. Beam current was measured using a Faraday cup connected to a picoammeter. Our experimental setup with the installation of a PLA provides the ratio between beam current and EC of about 70%. Most of the experiments employed 1000 eV electron energy with a 0.5 mA EC and a 100 V grid voltage, generating a current density of 1.5 mA/cm² (9.4×10^{15} cm⁻² s⁻¹).

In situ ellipsometry with a He-Ne laser operating at a wavelength of 632.8 nm mounted on the reactor allowed us to study surface modification and etching in real-time.³⁸ The

ellipsometry laser was aligned using the calibration phosphor screen to a location where a 1000 eV focused electron beam was irradiated, as shown in Fig. 4.2(c). Therefore, the ellipsometer can collect the psi-delta value of the area treated by remote plasma, electron beam, and its combination. The sampling rate of the ellipsometer was set to 5 Hz (0.2 seconds per point) for all experiments.

XPS analyses have been performed at the end of a processing step to measure surface chemistry evolution under the influence of electron bombardment. The samples were transferred under vacuum to a Vacuum Generators ESCALAB MK II surface analysis system for XPS measurements. Small area XPS measurement with the diameter of analysis area of 5-6 mm was used to probe surface portions interacting with and without an electron flux with the remote plasma.¹⁸⁶ High resolution scans of the Si2p, C1s, O1s, N1s, and F1s spectra were obtained at 20 eV pass energy at an electron take-off angle of 20° (shallow probing depth \approx 20-30 Å) and 90° (deep probing depth \approx 80 Å) with respect to the sample surface. The spectra were fitted using the least square fitting after Shirley background subtraction.^{39, 40}

4.3 Results and Discussion

4.3.1 Remote Plasma on SiO₂ and Poly-Si

The characterization of the SiO₂ and poly-Si ER on remote plasma operating parameters provided a foundation, including the flux of reactive neutrals, before moving to the study of etching processes involving the co-introduction of remote plasma and EB. Operating conditions were 10 SCCM Ar flow rate, variable CF₄/O₂ gas mixtures with a total CF₄ and O₂ gas flow rate of 5 SCCM, a source power of 400 W, and 1.8 mT DC magnetic fields. The reactor chamber was

held at 1.8 mTorr with the presence of the DPU and PLA. Ar is used as a carrier gas to dilute the concentration of gas-phase reactants to minimize erosion of the yttria-coating disc in the flood gun.

SiO₂ and poly-Si ERs under remote plasma as a function of variation of CF₄/O₂ flow rates are shown in Fig 4.3. CF₄/O₂ remote plasma delivers the maximum F flux at 20% O₂ and has been explained by CF₄ oxidation reactions.^{181, 182, 184, 185} The operating conditions with more than 20% O₂ increased the partial pressure of reactive oxygen species, leading to surface oxidation as a primary surface reaction. Since poly-Si etching is a spontaneous, chemically driven reaction, the Si ER directly mirrors the flux of fluorine reactants from the remote plasma source and peaks at 20% O₂. The operating condition at more than 20% O₂ resulted in a decreased poly-Si ER. SiO₂ etching, in contrast, is mainly an energy-driven reaction, e.g. by ion or electron bombardment. No SiO₂ ER was observed for all oxygen concentrations.

The minimum effective F flux from remote plasma can be estimated using the measured poly-Si ER induced by fluorination of silicon. We assume that one silicon atom reacts with four fluorine atoms for the production of a silicon tetrafluoride (SiF₄) molecule with unit reaction probability. This provides the minimum effective F flux in the range between $6 \times 10^{12} \text{ cm}^{-2} \text{ s}^{-1}$ to $5 \times 10^{14} \text{ cm}^{-2} \text{ s}^{-1}$. Other groups¹⁸⁷⁻¹⁹¹ have measured the reaction probability that shows an inverse dependence with F flux, from 0.03 at a F flux of $10^{12} \text{ cm}^{-2} \text{ s}^{-1}$ to 0.001 at a F flux of $10^{20} \text{ cm}^{-2} \text{ s}^{-1}$. Assuming these measured reaction probabilities near 0.01 for our conditions, we can estimate that for Ar/CF₄/O₂ remote plasma a F flux between $6 \times 10^{14} \text{ cm}^{-2} \text{ s}^{-1}$ to $5 \times 10^{16} \text{ cm}^{-2} \text{ s}^{-1}$ is provided for our conditions.

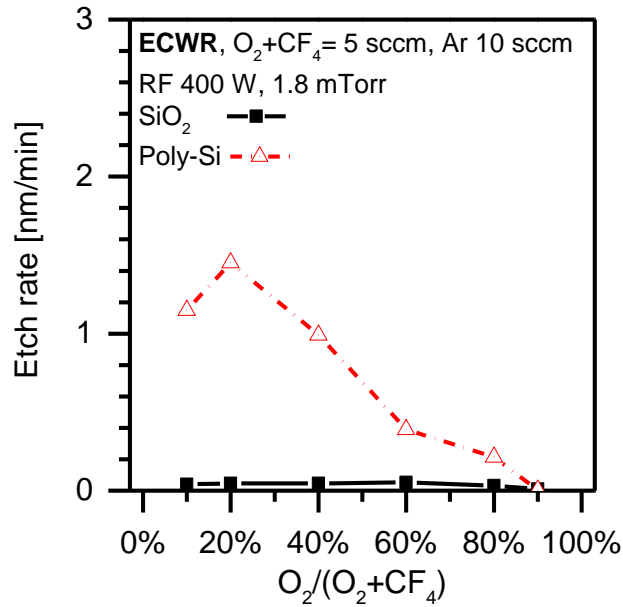


FIG. 4.3. (Color online) The etching rate of SiO₂ and poly-Si using remote plasma with various CF₄/O₂ flow rates.

4.3.2 Co-introduction of Electron Beam and Remote Plasma for SiO₂ Etching

After evaluating the SiO₂ and poly-Si ER for remote plasma only, the work moved to screen the dependence of SiO₂ ER on processing parameters when EB and 40% O₂ remote plasma were applied simultaneously. We examined four processing parameters, i.e. EC and electron energy of the electron flood gun, and the RF source power and flow rate of CF₄/O₂ of the remote plasma source. Since the electron beam diameter is regulated by the electron energy and control grid voltage, the grid voltage was adjusted accordingly for the experiment with different electron energies to keep the beam diameter unchanged. Investigating the first two processing parameters is commonly found in electron beam-induced processes.^{21, 22, 66, 166, 192} Plasma etching often examines the effect of source plasma and precursor chemistry toward the

effect of material modification and etching.¹¹ A study of the parametric dependency provides a better understanding of this new experimental configuration.

The result of varying ECs and electron energies is shown in Fig. 4.4. The operating condition of remote plasma was kept at a 400 W source power, 1.8 mT magnetic fields, and a gas flow rate Ar/CF₄/O₂ of 10/3/2 SCCM, respectively. SiO₂ ER is positively correlated to the applied EC in the range from 0.005 mA to 0.3 mA. As the applied EC was higher 0.3 mA, SiO₂ ER did not get further increased but suppressed. We postulate that the ER profile in Fig. 4.4(a) may be related to the transition from electron-limited to mass transport-limited regimes.¹⁹² In the electron-limited regime, the electron flux on a substrate regulates surface reactions, including the dissociation rate of adsorbates. When the electron flux was higher than a certain threshold, the SiO₂ ER was limited by transport of gaseous reactants to the surface, such as the replenishment rate of adsorbates, the average residence time of the neutral species, and the desorption rate of etching products. Our flood gun does not have a function of controlling the dwell time. Electrons continuously impinge on the substrate surface, which dramatically degrades the replenishment rate of adsorbates.^{66, 166, 192}

Fig. 4.4(b) summarizes the impact of reducing electron energy from 1000 eV to 300 eV on SiO₂ ER. The figure shows that the SiO₂ ER decreases with applied electron energy, where 300 eV electron energy produced a faster ER than 1000 eV. The possible ways of electron-adsorbate interaction include electron attachment, neutral dissociation, and dissociative ionization.^{164, 193} The probability that a pathway takes place depends on the energy dependence of the corresponding cross-section. Typically, at an electron energy of about 100 eV the cross-section for dissociation ionization^{66, 194-198} reaches a maximum. This may explain the observation

that 300 eV electrons are more efficient for energy deposition to adsorbates than 1000 eV electrons. The experimental result of screening the parametric dependency in the flood gun against SiO₂ ER is consistent with what has been found in studies of EBIE of SiO₂.^{21, 66}

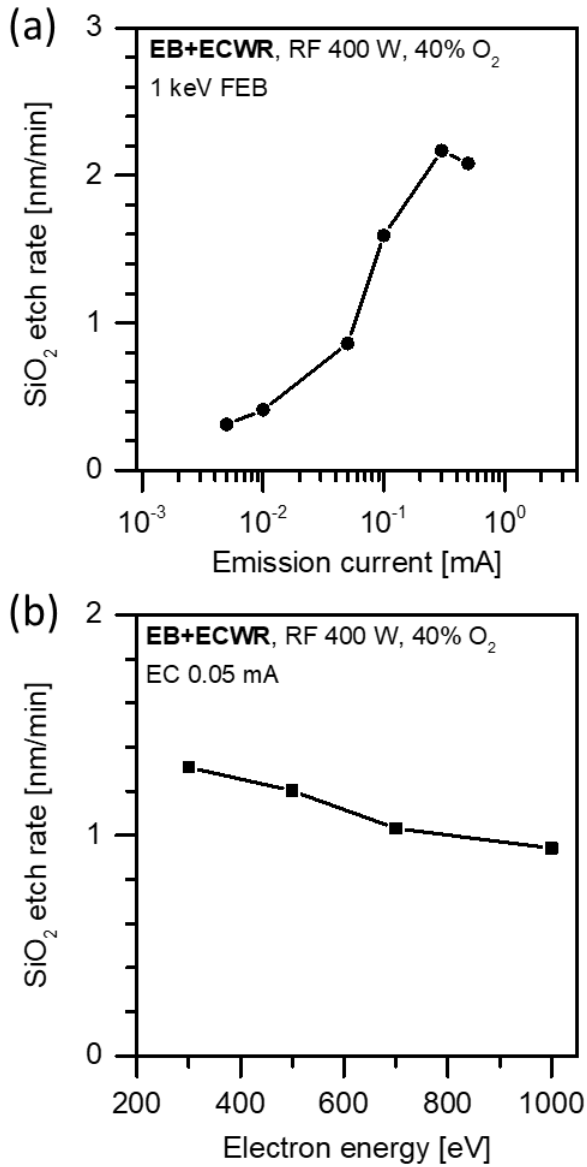


Fig. 4.4. (Color online) The SiO₂ etch rate as a function of (a) emission current and (b) electron energy.

Next, we explored the effect of remote plasma processing parameters on SiO₂ ER. The operating condition of the flood gun was kept at 1000 eV electron energy, a 0.5 mA EC, and the control grid of 100 V. A summary of the dependence of SiO₂ ER on RF source power and CF₄/O₂ flow rates of the remote plasma source is shown in Fig. 4.5. RF power is used to control the energy input into the ECWR plasma source, where a high RF power enhances the dissociation rate of injected precursor gases,¹⁹⁹⁻²⁰² and thus controls the number of radicals in the reactor. Fig 4.5(a) shows that a variation of RF power with an EC below 0.05 mA did not lead to significant ER difference. A higher EC of 0.5 mA produced a noticeable ER dependence on RF power. We postulate that the SiO₂ ER profile in Fig 4.5(a) can be explained by energy-limited (electron flux) and mass transport-limited (radical flux) regimes. When EC was at 0.05 mA or below, the SiO₂ removal was limited by the electron flux, and RF power that controls the dissociation rate of the remote plasma does not affect the SiO₂ ER. For higher electron currents, the etching rate became mass transport-limited. At that point, the RF power that controls the flux of dissociated neutrals in a reactor showed a positive relationship to the measured SiO₂ ER.

Fig 4.5(b) investigates SiO₂ ER under various ECs and flow rates of CF₄/O₂ for co-introduction of remote plasma and EB. The SiO₂ ER measured for remote plasma only has been included for reference. Fig. 4.5(b) indicates that the EB induces SiO₂ etching. For example, for remote plasma only (green line), no SiO₂ etching was seen. For the combination of 1000 eV EB with a 0.01 mA EC and 40% O₂ remote plasma a ~0.4 nm/min SiO₂ ER was produced. The flow rate of CF₄/O₂ that regulates the chemistry of precursors into the reactor significantly influences the etching result. As compared to operating in O₂-rich conditions, a CF₄-rich gas mixture delivered a faster SiO₂ ER. A high EC emphasized the ER difference due to changes in the

precursor chemistry of the remote plasma. The observed ER trends can be explained by a fluorination reaction since the main flux of neutrals from the remote plasma source controls the composition of adsorbates on the SiO₂ surface.^{181, 185} The EB simultaneously energized the adsorbates and enhanced the desorption of SiO_xF_y etching products.^{163, 203} In contrast, the O₂-rich remote plasma produced less fluorine flux to the reactor so that the probability of surface fluorination and electron-stimulated desorption was limited. These data demonstrate that precursor chemistry produced by the remote plasma source plays an important role for the SiO₂ ER during co-introduction of remote plasma and EB fluxes.

Fig 4.5(b) demonstrates a new processing window for this experimental configuration that consists of a remote plasma source and a flood gun. The conventional EBIE requires a dedicated synthesis procedure to prepare a precursor for evaluating its etching performance on a material.^{21, 22, 177} Some precursors are reactive and short-lived, adding another level of complexities. This new experimental approach provides a platform where reactive species can be generated using a plasma source in a vacuum chamber. The adsorbate chemistry can be simply controlled by precursor chemistry, mixtures of stable process gases and relative flow rates. The use of a vacuum chamber extends the lifetime of excited reactants and helps to manage the use of environmentally harmful substances. The co-introduction of particle fluxes from remote plasma and EB enables SiO₂ etching. This approach can serve as the basis to develop novel processes for advanced etching applications, such as photomask repair and anisotropic pattern transfer.

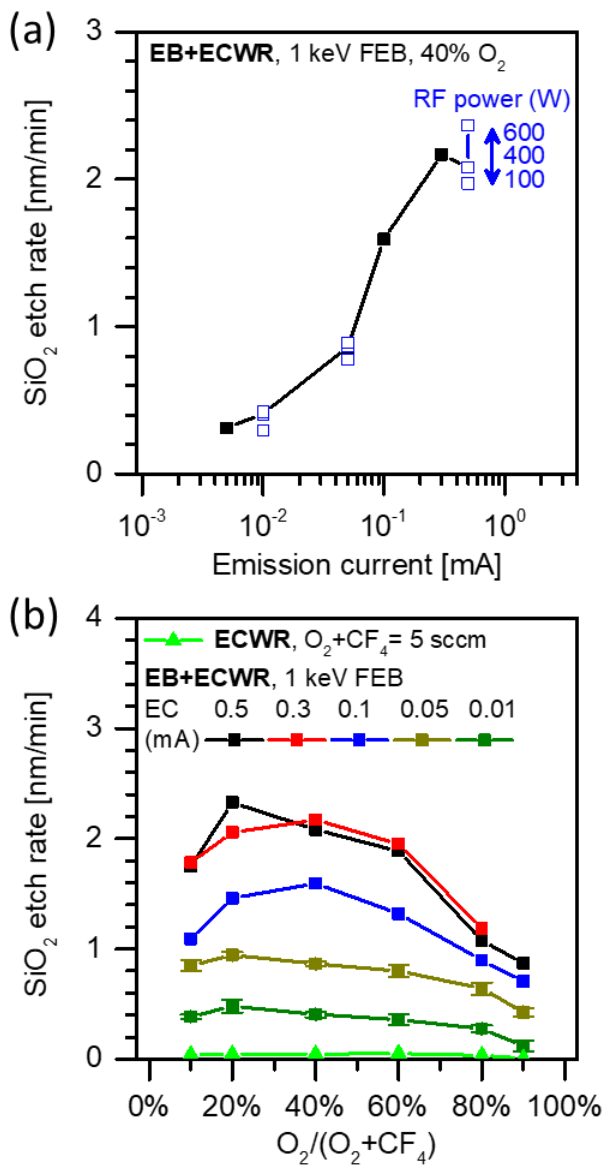


FIG. 4.5. (Color online) The etching rate of SiO₂ as a function of (a) RF power and (b) CF₄/O₂ flow rate.

4.3.3 Prototypical Processing Development

After screening the influence of the operating parameters of the ECWR source and EB source on SiO₂ ER, the development of two prototypical processes was investigated: 1) steady-state etching of SiO₂ during co-introduction of particle fluxes from remote plasma and EB sources and 2) ALE of SiO₂ enabled by sequential treatments consisting of a remote plasma surface treatment step followed by EB irradiation. Remote plasma was used for surface functionalization. We employed O₂-rich precursor chemistry with an Ar/CF₄/O₂ flow rate of 10/1/4 SCCM, respectively. The processing parameters of the flood gun were kept at 1000 eV electron energy, 0.5 mA EC (0.35 mA beam current), and a control grid voltage of 100 V. The experimental result elucidates the development of this new experimental configuration, which outperforms in comparison with conventional EBIE.

The first case studied a three-step process that consists of 100-second remote plasma treatment, another 100-second treatment that consisted of co-introduction of particles from the remote plasma and EB sources, and finally 100-second EB irradiation of the surface in the presence of Ar/CF₄/O₂ without remote plasma power. This is shown in Fig 4.6(b). The purpose of this process sequence was to identify the functionality of each component by following the real-time SiO₂ ER evolution. The first step consisting of Ar/CF₄/O₂ remote plasma exposure only for 100 seconds did not lead to any SiO₂ ER. This is consistent with the experimental result shown in Fig 4.3. The second step consisted of simultaneous introduction of Ar/CF₄/80% O₂ remote plasma and 1000 eV focused EB (FEB) using 0.5 mA EC. This treatment resulted in significant SiO₂ etching. The SiO₂ ER promptly went up from 0 to 1.3 nm/min during the first 20 seconds of exposure, and then stabilized at ~1.0 nm/min for the remaining 80 seconds of

exposure using these conditions. We postulate that the cause of the initial rate elevation might be similar to the finding in the study of Ar^+ and XeF_2 on Si by Coburn and Winters.^{57, 204} The SiO_2 surface after exposure to the initial remote plasma was functionalized by excess reactants, which caused a higher rate of material removal upon EB irradiation. The SiO_2 ER stabilized at a lower value once the flux of the incoming reactants and electrons reached a steady-state (Fig 4.6(a)). The last step utilized EB and $\text{Ar}/\text{CF}_4/\text{O}_2$ gases, where the electron-molecule interactions were analogous to the conventional EBIE. The SiO_2 ER sharply dropped to less than 0.1 nm/min within the first 20 seconds of this treatment. This indicates that the EB is highly inefficient with regard to dissociating the CF_4/O_2 gases and is required for SiO_2 etching. It also is consistent with the difficulty that has been found in conventional EBIE that many potential precursors are ineffective etchants. The experimental result of the three-step process revealed these key points: 1) remote plasma energizes the admitted precursors and provides reactive neutrals for surface modification, and 2) etching reaction only takes place at surface area portions that are simultaneously exposed to both remote plasma and EB.

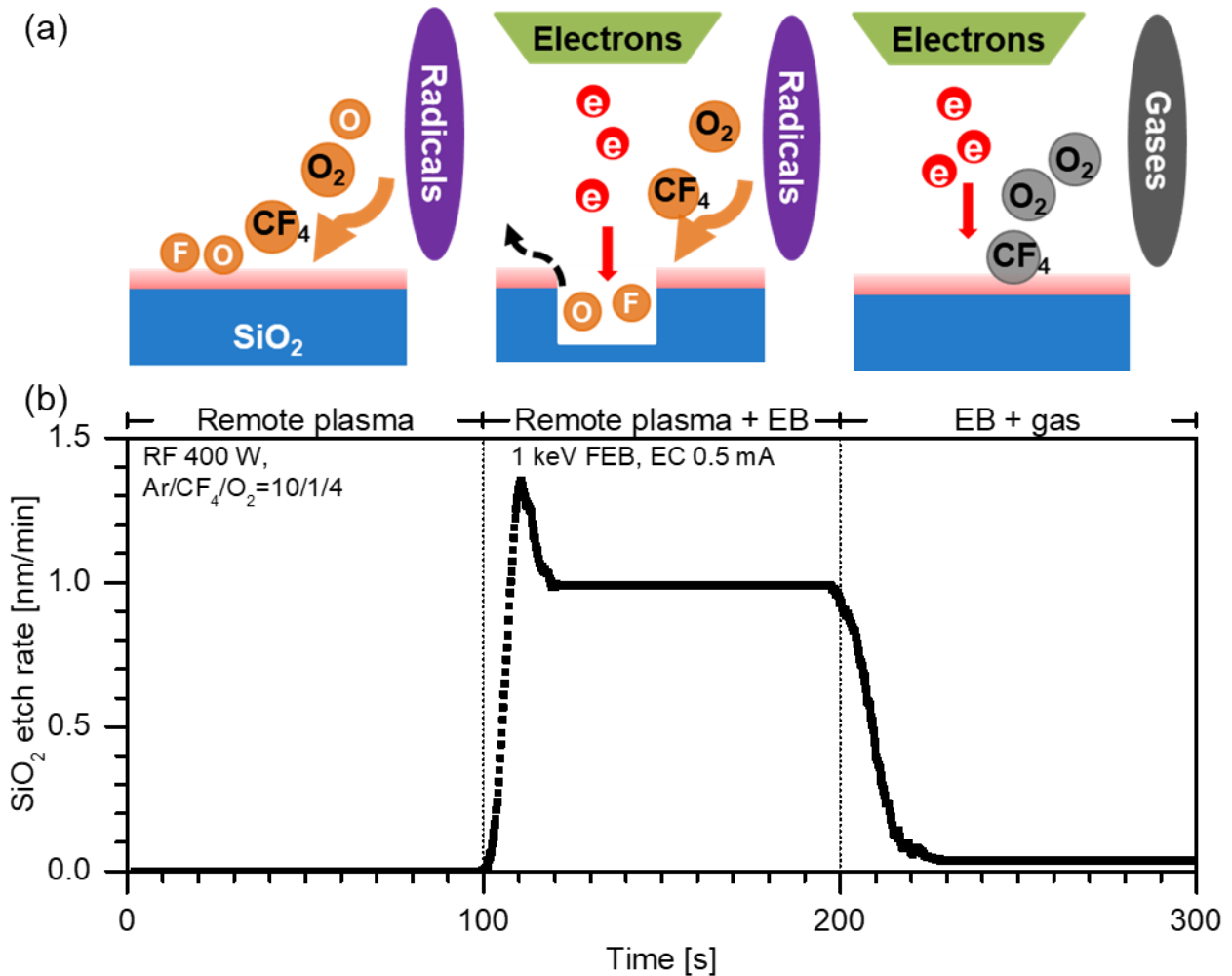


FIG. 4.6. (Color online) (a) Schematic diagram of the surface reaction for different exposure conditions. (b) The measured SiO₂ etching rate for these exposures using standard conditions.

The next approach is aimed at establishing ALE of SiO₂ by a sequence of a remote plasma treatment step followed by EB irradiation for surface activation. An example of such a sequential process consisted of a 100-second remote plasma treatment (Step 1) followed by 70-second EB irradiation (Step 2). The operating condition of the remote plasma source and flood gun was kept the same as described in the above example. A 100-second transition between these

two steps was used to evacuate residual gases in the reactor and restore the vacuum level to the low 10^{-6} Torr range. The concept of this processing sequence was to utilize Ar/CF₄/O₂ remote plasma for the fluorination of SiO₂, with the goal of lowering the energy threshold of desorbing etch products. The subsequent EB irradiation step deposited energy onto the modified layer and promoted an etching reaction.

Fig 4.7(a) shows *in situ* ellipsometry measurement and a model that describes SiO₂ etching and electron beam-induced deposition. Modeling of the psi-delta evolution was used to interpret the surface modification and film thickness changes. The complex index of refraction (n-ik) of SiO₂ and the build-up layer for the modeling was fixed at $1.42-0.00i^{205}$ and $2-0.03i^{206}$, respectively. The red dots presented the initial 100-second remote plasma treatment. This did not produce SiO₂ etching and kept the psi-delta values unchanged. A 1000 eV focused EB with an EC of 0.5 mA was employed for surface irradiation at a processing time of 220 second for 70 seconds. The blue and orange dots in Fig 4.7(a) describe the initial 15-second exposure and subsequent 55-second EB exposure, respectively. The ellipsometric model suggests that the beginning 15-second promoted two surface reactions simultaneously, i.e., SiO₂ etching and deposition, since the psi-delta trajectory followed the combination of these two vectors. The following 55-second EB exposure yielded a deposition reaction. An ellipsometric model was used to measure the detailed thickness change of SiO₂ and build-up.

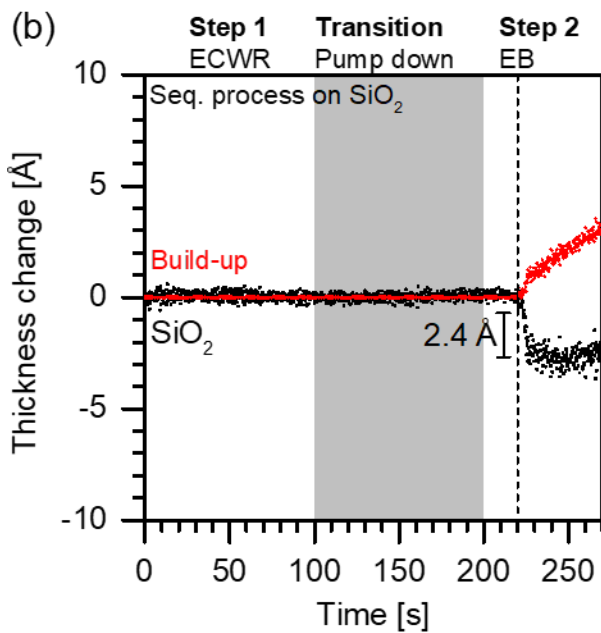
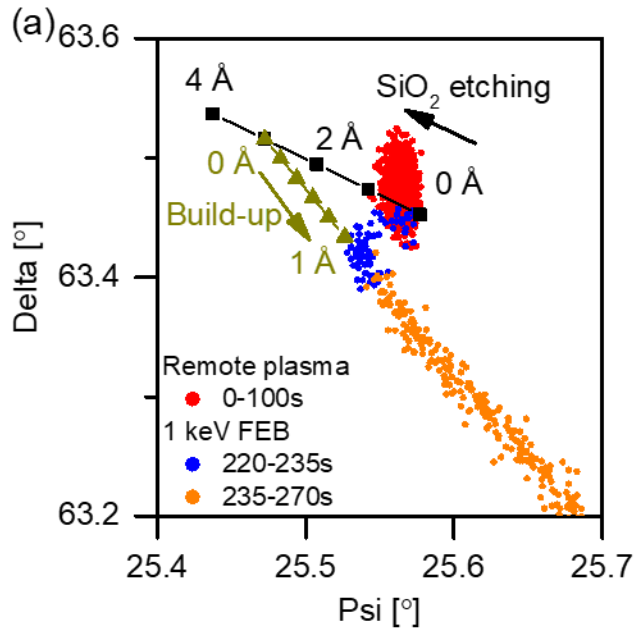


FIG. 4.7. (Color online) (a) A two-layer ellipsometric model that describes SiO_2 etching and subsequent electron beam-induced build-up and the experimental result of a procedure consisting of remote plasma and an electron beam. (b) Corresponding thickness change profile of SiO_2 and build-up.

The thickness profile of this sequential process interpreted using a two-layer ellipsometric model is shown in Fig 4.7(b). We did not observe any SiO₂ loss during the 100-second remote plasma treatment and the following pump-down transition. In the step introducing a 1000 eV focused EB, SiO₂ etching behaved in a self-limited manner where only the first 10-second produced about ~2.4 Å removal thickness. Extending EB processing duration did not remove more SiO₂ but contributed to a thicker build-up. The deposition is possibly due to the re-deposition of gas-phase etching products²⁰⁷ or the dissociation of residual gaseous species in the reaction chamber, e.g. gas-phase hydrocarbon from pump fluid¹⁷⁷. The thickness profile (Fig. 4.7(b)) supports the ALE concept, realized by temporally combining a remote plasma treatment step and an EB irradiation step. More importantly, with the assistance of a remote plasma source, EB bombardment can be used to activate material removal.

4.3.4 Process Characterization

Two prototypical cases exemplify the potential of the new experimental configuration for pattern transfer applications. Here we characterize the surface chemistry for the different processing steps, including EB irradiation, Ar/CF₄/O₂ remote plasma treatment, and the combination of these. The understanding of the surface modifications provides insights for future development. The following discusses three conditions aimed at clarifying etching mechanisms: 1) an EB irradiated on untreated SiO₂ with three exposure times, 2) a sequential treatment consisting of remote plasma treatment followed by an EB step, and shown in Fig 4.7. Finally, 3) the simultaneous interaction of the particle fluxes from the remote plasma and EB sources with the SiO₂ surface, and shown in Fig. 4.6. These processes allow us to explore the effect of an

electron flux to SiO₂, the surface layer modification by Ar/CF₄/O₂ remote plasma, and the electron-neutral synergy. Since the electron flux from the flood gun only covers a portion of the SiO₂ specimen (EB diameter ~5.5 mm), small area XPS analysis was used to compare the chemical composition of this area with different locations on the sample away from the EB outlet. Angle-resolved XPS analyses at take-off angles of 20° and 90° relative to the surface were also used to examine the surface and more bulk-sensitive chemical evolution of SiO₂ after these treatments. Therefore, for each sample, we probed three locations, including the area under the EB outlet, 3 mm away from the area under the outlet, and 10 mm away from the area under the outlet. In each case, photoelectrons were acquired at take-off angles of 20° and 90°. This approach allowed us to explore the effect of electron dose and chemical composition with respect to depth, and obtain an understanding of the spatial profile of characteristic elements. *In situ* ellipsometry was used to initially characterize surface modifications and etching for these treatments. Combining the result of the two measurements enabled us to obtain a more detailed understanding of the real-time surface reactions.

EB and Untreated SiO₂ Interactions

The *in situ* ellipsometric results for three EB experiments with different exposure times of untreated SiO₂ are shown in Fig 4.8(a). The operating conditions were 1000 eV focused EB using 0.5 mA EC and a reactor pressure of 1×10^{-7} Torr. We evaluated three exposure times: 0 seconds (untreated SiO₂), 30 seconds, and 200 seconds. The black dot describes that a 30-second EB irradiating on untreated SiO₂ increased the psi value from 62.9° to 63.7° with a slight increase of delta value. The orange dots describe a 200-second EB exposure of untreated SiO₂,

where the first 30-second shows the identical psi-delta trajectory as the previous run. The following 170 seconds resulted in the psi-delta data moving to the upper-left corner. Two ellipsometric models that describe the reduction of SiO_2 and sequentially the modification of the surface SiO_x layer were superimposed on the experimental results for reference. The complex index of refraction ($n-ik$) of SiO_2 ($1.42-0.00i$) and the modification layer ($1.47-0.2i$) for the modeling was also applied. Randolph's work⁶⁶ presented the concept that an electron flux induced the oxygen reduction in SiO_2 . Following this idea, we postulate that SiO_2 undergoes the formation of oxygen vacancies and a thinning reaction from SiO_2 to SiO_x during electron bombardment. The agreement of the ellipsometric model and experimental results during 30-second EB irradiation of SiO_2 , suggesting that the SiO_2 thickness decreased by a few Å. After application of more than 30-second EB exposure, the psi-delta trajectory deviated from the SiO_2 thinning line and instead indicated the modification of this surface SiO_x layer. The optical property of this modification layer is very different from the underlying SiO_2 layer, where the value of delta significantly changed from 293° to 294° during the sequential 170-second EB exposure. This deviation implies that EB further modified the surface layer to produce an extinction coefficient (k) for light adsorption. Fig. 4.8(b) summarizes the profile of the overall thickness change. The initial 30-second EB irradiation is consistent with 6 Å thinning, and during the following 170-seconds modification took place with the film thickness restored close to the initial. Based on the ellipsometric result, the chemical composition of the surface layer clearly shows differently from untreated SiO_2 . *In situ* ellipsometry captured two distinct reactions for EB exposure of untreated SiO_2 .

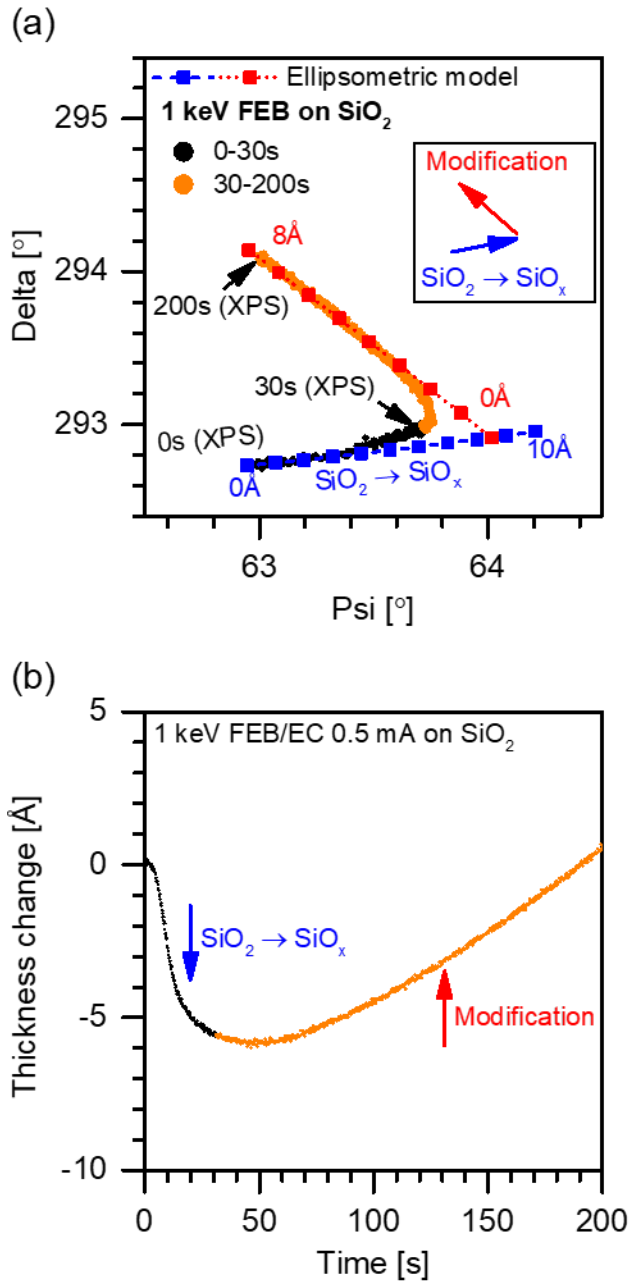


FIG. 4.8. (Color online) (a) *In situ* ellipsometry results after 1000 eV focused electron beam irradiates SiO₂ with the duration of 200 seconds and an ellipsometric model that describes the reduction of SiO₂ thickness. (b) Overall thickness change profile.

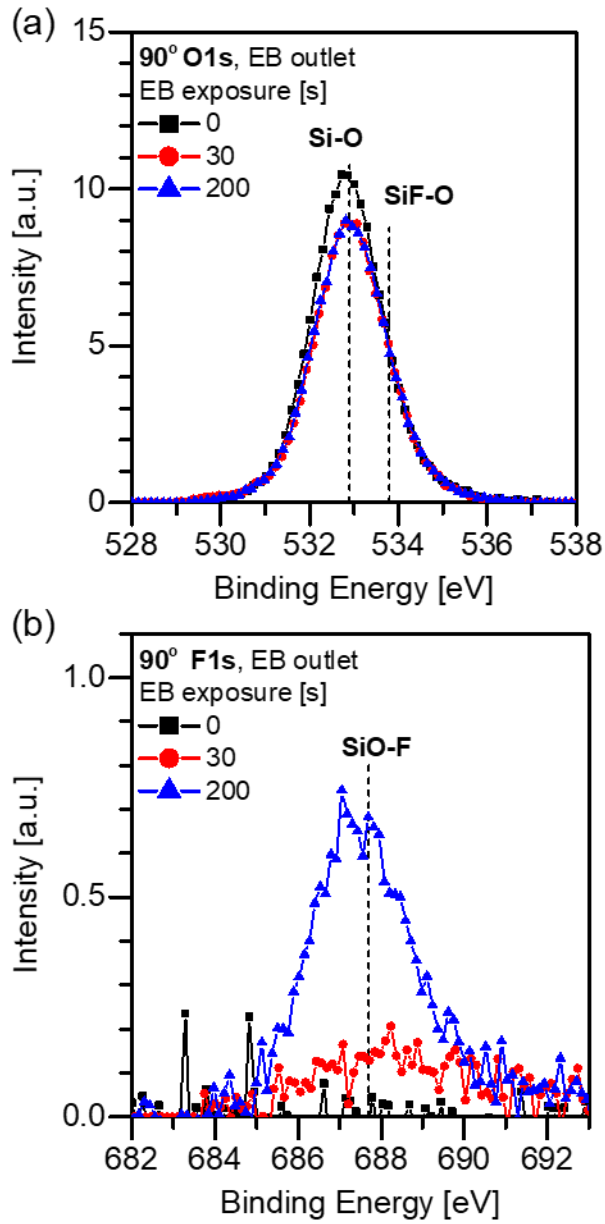


FIG. 4.9. (Color online) XPS spectra of (a) O1s and (b) F1s with various EB exposure times on SiO₂.

To validate the interpretation of the *in situ* ellipsometry measurement with this kind of model, XPS analysis was used to examine SiO₂ surfaces subjected to the EB exposure. The

intensity of characteristic elemental peaks of SiO₂ were examined for three EB exposure times, i.e., 0 seconds, 30 seconds, and 200 seconds. The time evolution of the O1s and F1s spectra is summarized in Fig 4.9(a) and (b). Fig 4.9(a) shows that the untreated SiO₂ sample had the highest oxygen intensity when compared to the other samples after EB exposure. A 30-second EB decreased the Si-O intensity, and a longer exposure time of 200 seconds did not result in a further decrease. The time evolution of the F1s spectra is displayed in Fig 4.9(b) and indicates formation of SiO-F bonding during EB exposure time. The uptake of F by the SiO₂ surface is plausible, given the fact that the reactor chamber had been exposed to prior fluorocarbon-based remote plasma treatments. The fluorine species adsorbed on the reactor walls provide a finite fluorine pressure in the gas phase.²⁰⁸⁻²¹⁰ This residual fluorine can become attached to reactive sites produced on the SiO₂ surface during EB bombardment.

Fig 4.10 provides an overview of the time evolution of characteristic elemental XPS peak areas measured for an experimental geometry employing a photoelectron take-off angle of 90°. The C1s intensity does not show a noticeable change during the EB exposure time extended from 30 seconds to 200 seconds, implying that the carbon build-up during this time interval was not significant. The O1s intensity only decreased during the initial 30 seconds and subsequently stabilized. The F1s intensity was proportional to the EB exposure time. The XPS result indicates oxygen loss and therefore changes in Si-O bonding during the initial 30 seconds EB bombardment. The XPS results of SiO₂ for different EB exposure times are consistent with the changes of the *in situ* ellipsometry measurements. Both of these measurements confirm that a flux of 1000 eV electrons leads to the formation of oxygen vacancies in SiO₂.

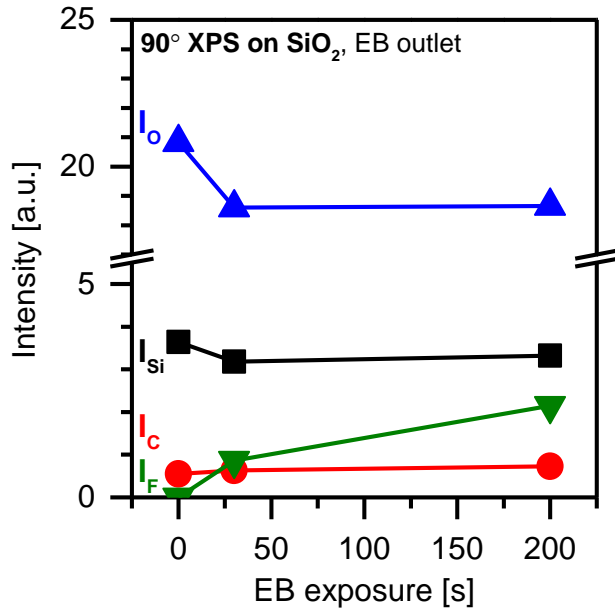


FIG. 4.10. (Color online) Summary of XPS spectra with various EB exposure times on SiO₂.

Sequential Treatment Consisting of Remote Plasma and Subsequent EB Exposure

After the surface characterization identified the reactions induced in SiO₂ by EB bombardment, we studied the processing sequence depicted in Fig 4.7(c). It consisted of an Ar/CF₄/O₂ remote plasma step followed by EB exposure. We also measure the surface chemical composition by XPS at the end of each step. The exposure time was reduced to 5 seconds to minimize electron beam-induced deposition during the EB step. The other flood gun parameters (1000 eV focused EB with a 0.5 mA EC) were unchanged.

Fig 4.11 summarizes the O1s and F1s spectra measured for the SiO₂ area directly under the EB outlet at two photoelectron take-off angles after a 100-second remote plasma and the sequential 5-second EB, respectively. Fig 4.11 (a) and (b) show that the sequential EB led to an increased oxygen intensity but a decrease in the fluorine intensity, implying that the surface

underwent a defluorination reaction as a result of the electron flux. Such a defluorination reaction has also been seen in plasma-based ALE as a result of ion bombardment.^{5, 8, 75} The 90° photoelectron take-off angle spectra monitored a deeper region of SiO₂ and displayed the opposite trend as what the surface spectra showed. This suggests that the SiO₂ bulk underwent a higher degree of fluorination and reduced oxygen intensity after 5-second EB, consistent with what we observed in Fig 4.9. The electron flux reduces SiO₂ to SiO_x (x<2) and allows fluorine to adsorb to reactive sites thus formed in SiO_x. Angle-resolved XPS analysis identified that the surface reactions behaved differently from the bulk after a 5-second EB irradiation on the modified SiO₂.

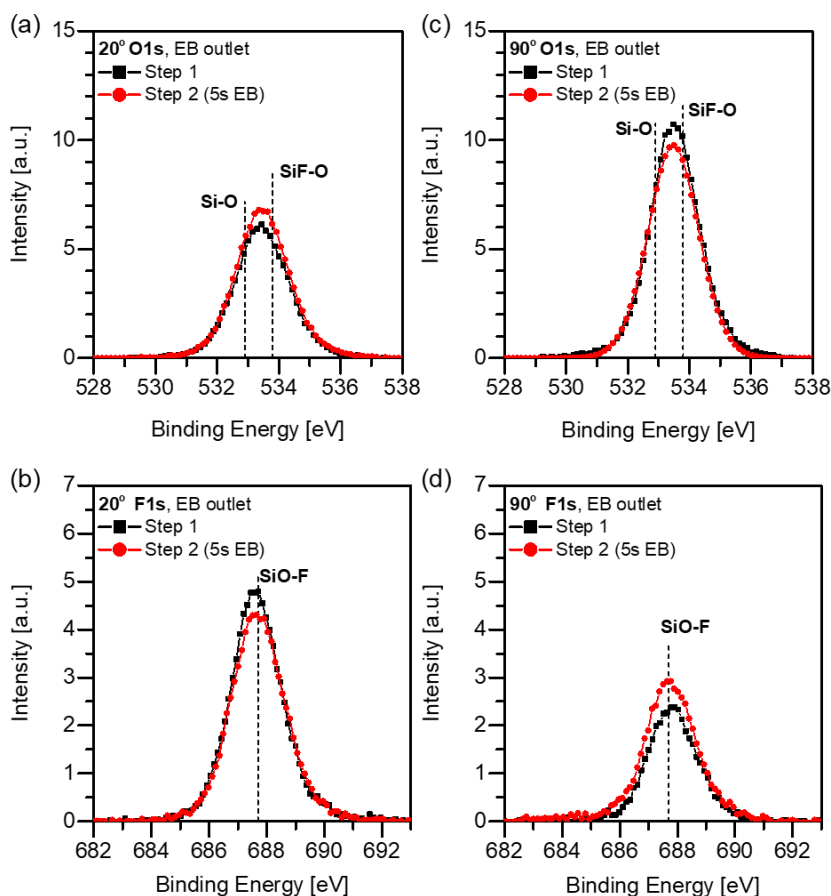


FIG. 4.11. (Color online) XPS spectra of using a 20° take-off angle for (a) O1s and (b) F1s photoelectrons and using a 90° take-off angle for (c) O1s and (d) F1s photoelectrons for the procedure of Fig.8(a), respectively.

We also measured the surface areas on the SiO₂ samples that received a lower EB flux, or no electron flux as a reference. This allows to differentiate the EB effect relative to SiO₂ surfaces after the same remote plasma treatment. Three locations were probed: the area under the EB outlet, 3 mm away from the area under the outlet, and 10 mm away from the area under the outlet. While the EB diameter is around 5.5 mm on a substrate, the area under the EB outlet and 3 mm away from the area under the outlet can provide the chemistry information with regard to high and low electron doses. The position at 10 mm away from the area under the outlet is representative of SiO₂ that has only been treated by remote plasma.

Fig 4.12 summarizes the lateral chemistry evolution for the different processing steps of the procedure depicted in Fig 4.7(c). We observed an increased fluorine peak for the surface portion directly under the EB outlet after the remote plasma treatment. This could be due to two factors: firstly, the surface close to the PLA increased the mean free path of reactants. Secondly, before processing, a sample pretreatment, which comprised 80% O₂ remote plasma and 1000 eV focused EB with a 0.15 mA EC for 200 seconds, was used to remove surface contamination and adventitious carbon. Such a pretreatment might locally deposit fluorine into SiO₂. While each sample had the same preparation procedure, the intensity difference among the processing steps still delivered the crucial information.

Fig 4.12(a) shows that the surface under the EB outlet after a sequential 5-second EB exposure showed increased O intensity and reduced F intensity relative to the remote plasma

treated surface. The intensity difference of the O and F spectra between the two steps became smaller as the position being analyzed moved to positions that had received less electron flux. In contrast, Fig 4.12(b) shows the chemistry evolution of the deeper region of SiO₂. A 5-second EB exposure on an area under the EB outlet resulted in a significant decrease of the O intensity with an increased F intensity; additionally, the intensity difference of the spectra decreased as the analysis location moved to the 10 mm lateral position which is characteristic of remote plasma only. The spectral changes for the three lateral positions represent the impact of the electron flux to the surface and bulk reactions. The surface underwent a defluorination reaction, whereas the deeper region received more fluorine uptake and showed a decreased oxygen intensity.

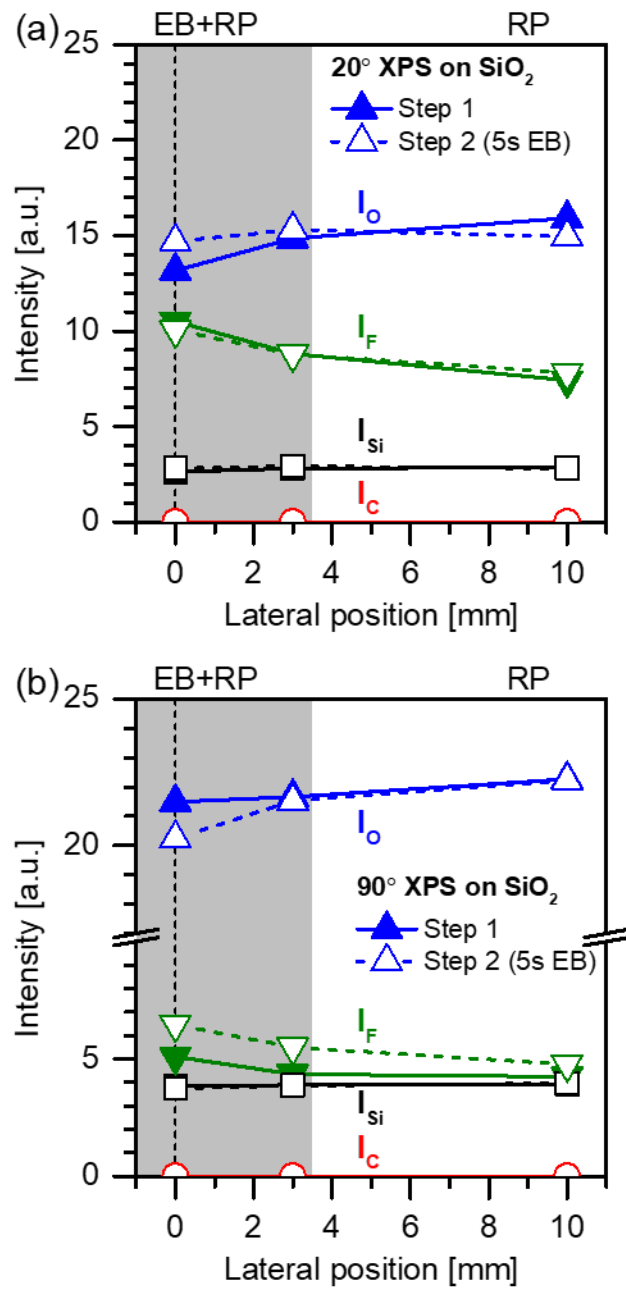


FIG. 4.12. (Color online) Summary of the characteristic spectra (Si2p, C1s, O1s, and F1s) of SiO₂ in the procedure of Fig. 4.7(c). Two take-off angles are used including (a) 20° and (b) 90°.

Co-introduction of Remote Plasma and EB on SiO₂

The last part of the characterization was focused on probing surface chemistry evolution by comparing the state after remote plasma treatment and the one obtained subsequently when fluxes from remote plasma and EB source were co-introduced. This is schematically shown by the procedure depicted in Fig. 4.6(b). The operating conditions for remote plasma were a flow rate of Ar/CF₄/O₂ of 10/1/4 SCCM, a 400 W RF source power, and 1.8 mT static magnetic field. The processing parameters of the flood gun were 1000 eV electron energy, 0.5 mA EC, and 100 V control grid voltage. We employed a similar XPS analysis method as used in the previous section to evaluate the spatial distribution of characteristic elements.

Figure 4.13(a) and (b) summarize the O1s and F1s spectra using a photoelectron take-off angle of 20°. The data were acquired for SiO₂ surfaces at the end of a 80% O₂ remote plasma treated, and at the end of the remote plasma/EB co-introduction step, respectively. By XPS analysis the area under the EB outlet was characterized. The surface after the remote plasma/EB co-introduction process showed a slightly increased O intensity with a noticeable reduction of the F intensity. In contrast, Fig 4.13(c) and (d) present the O1s and F1s spectra obtained at an photoelectron take-off angle of 90° for the same procedure. The co-introduction step contributed to a reduced O intensity with an increased F intensity. There is no peak shift after the co-introduction process. The surface chemistry tendencies for SiO₂ surface and bulk regions is similar to what we observed in the previous section.

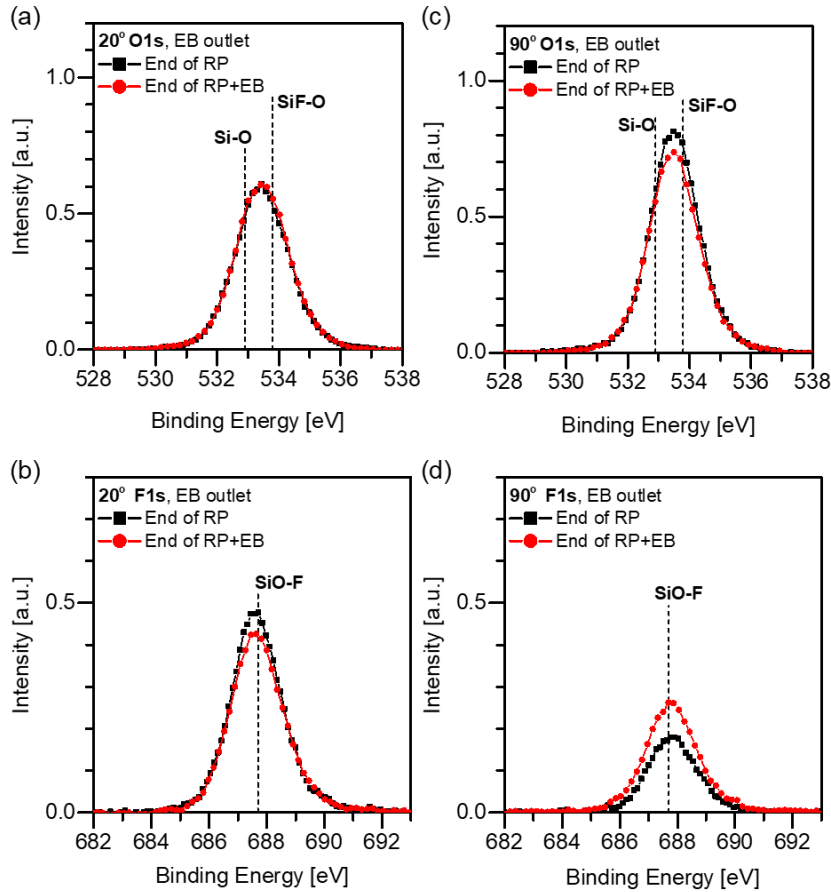


FIG. 4.13. (Color online) XPS spectra of SiO_2 at the end of remote plasma and simultaneous remote plasma/EB process for the procedure shown in of Fig. 4.6(b), respectively. The O1s (a) and F1s (b) photoelectron spectra were taken at a 20° take-off angle, whereas the O1s (c) and F1s (d) spectra were taken at a 90° take-off angle.

We also studied the effect of an electron flux on the chemistry profile transformation of SiO_2 by probing different sample positions. In the surface profile in Fig 4.14(a), the O intensity difference between the remote plasma treatment and the remote plasma/EB co-introduction process is positively related to the applied electron flux. The F spectra correlate with the electron dose, where the area under a high electron flux leads to a reduced F intensity. For comparison, the XPS result using a photoelectron take-off angle of 90° is shown in Fig 4.14(b). The area for a

high electron dose showed a reduction of the O1s intensity and increased F 1s intensity after the co-introduction step. The F 1s intensity sharply dropped as the lateral position moved from 0 to 10 mm.

The surface chemistry evolution difference between surface and bulk SiO₂ during the co-introduction step supports our finding that multiple reactions take place concurrently. The comparison of different probing positions at a photoelectron take-off angle of 20° suggests that the remote plasma/EB co-introduction promotes defluorination of the treated SiO₂ surface. The degree of defluorination strongly depends on the incoming electron flux. This response agrees with what we observed for the two prior characterization cases. The bulk behaves differently from the surface. The applied electron flux positively correlates to the degree of fluorination. The cause of a decreased O 1s intensity at the area under the EB outlet could be due to two factors: 1) the fluorination reaction modified SiO₂ by converting it to SiO_xF_y, or 2) EB bombardment gave rise to oxygen vacancies. Fig 4.14(a) and (b) provide a comprehensive overview of the spatial, chemical transformation for the case of remote plasma and EB co-introduction of SiO₂.

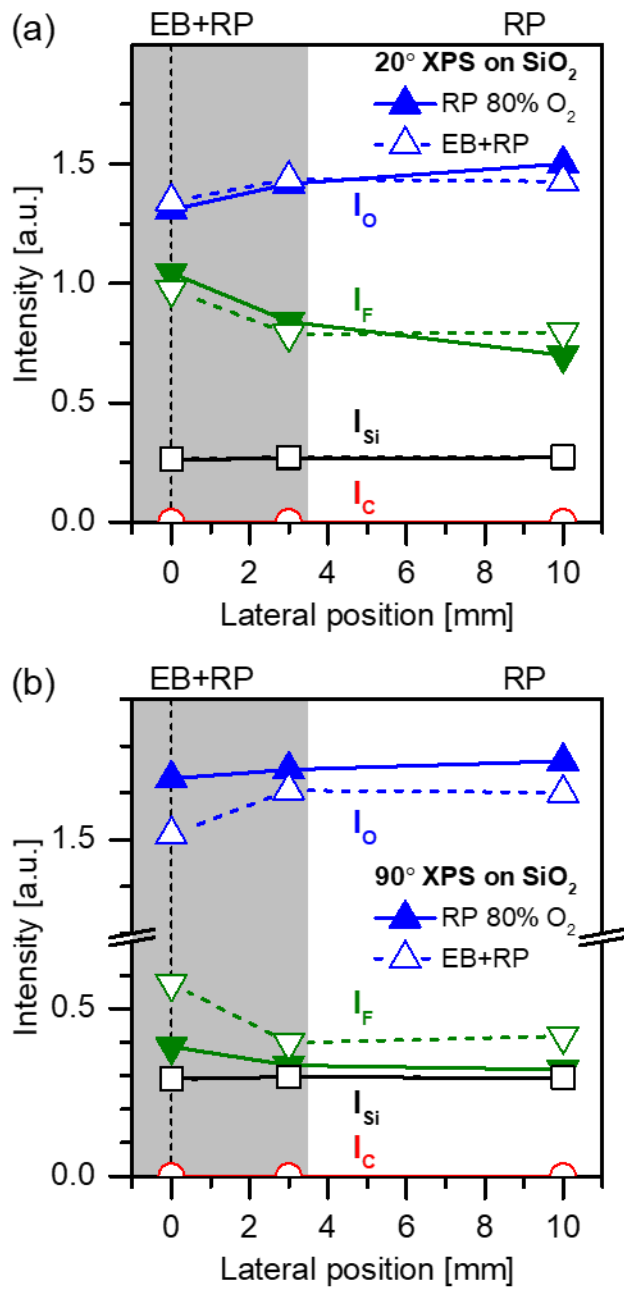


FIG. 4.14. (Color online) Summary of the characteristic spectra for the procedure shown in Fig. 6(b). Photoelectron take-off angles of (a) 20° and (b) 90° were used.

To summarize our findings for the three surface treatments characterized here, the schematic diagram shown in Fig 4.15 can be used to illustrate the observed interactions. When an EB irradiates an untreated SiO_2 surface, the oxygen intensity decreased after 30-second and 200-second EB exposures (see Fig 4.15(a)). This finding agrees with the idea that EB induces oxygen vacancies in SiO_2 and previously postulated by Randolph et al.⁶⁶. The non-stoichiometric Si-O sites thus formed appear highly reactive when interacting with incident reactants, e.g. fluorine from the reactor walls. Additionally, the XPS spectra showed fluorine uptake during EB exposure of the SiO_x layers.

The second case discussed a sequential treatment that consisted of an Ar/ CF_4 / O_2 remote plasma treatment followed by an EB step (Fig 4.15(b)). The remote plasma modified the SiO_2 surface by developing a fluorinated surface layer. During the subsequent EB step, the surface showed desorption of some of the fluorinated layer, whereas the deeper SiO_2 region still exhibited formation of oxygen vacancies.

The last case studied was the remote plasma/EB co-introduction process (Fig 4.15(c)). Here the SiO_2 surface exhibited evidence of multiple reactions, including the uptake of oxygen and fluorine adsorbates and electron-estimated desorption. The surface characterization results obtained with a 90° photoelectron take-off angle suggests that EB promotes the desorption of oxygen from SiO_2 on the one hand, and adsorption of fluorine from remote plasma on the other. The SiO_2 responses seen for the three cases are consistent with each other.

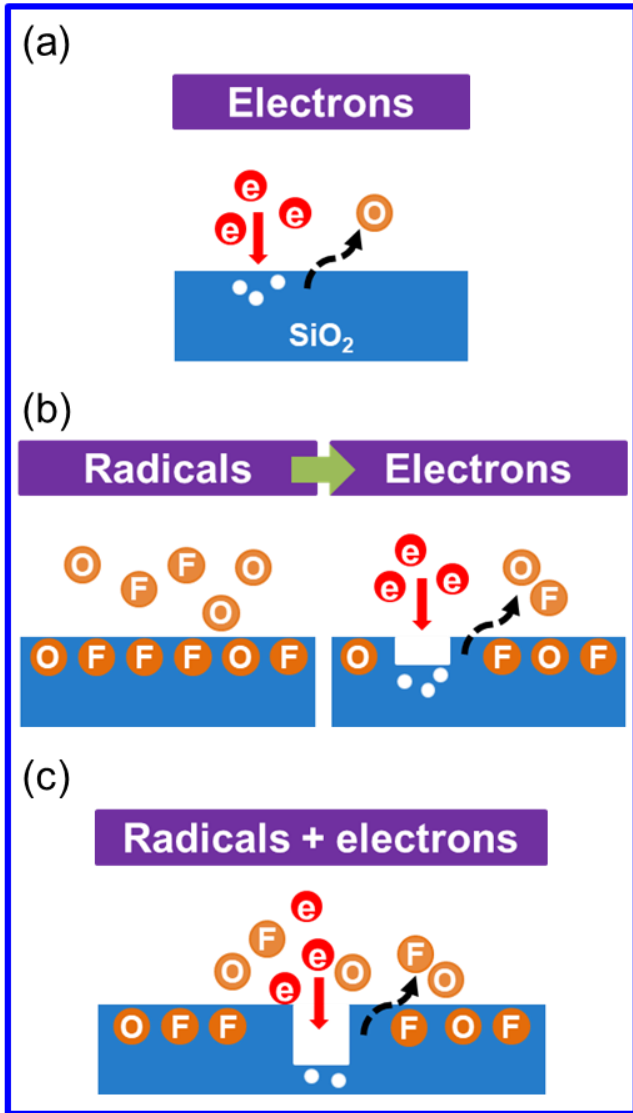


FIG. 4.15. (Color online) A schematic diagram that describes surface reaction under three different processing modes including (a) EB irradiation on SiO₂, (b) EB irradiation on modified SiO₂, and (c) the co-introduction of electrons and radicals.

4.4 Summary and Conclusions

This work developed a new experimental configuration that integrates a remote plasma source and a flood gun for enabling EBIE of SiO₂ with Ar/CF₄/O₂ remote plasma generated radicals to enable atomic scale etching of SiO₂. The dependence of SiO₂ etch rate on electron flood gun parameters shows that as the EC varies from 0.01 mA to 0.3 mA, the SiO₂ ER scales primarily with the electron flux. When the applied EC was above 0.3 mA, the SiO₂ ER was controlled by the chemical species flux produced by the remote plasma source. Here the SiO₂ etching rate depends on the replenishment rate of adsorbates, the residence time of precursors, and the desorption rate of etching products is primarily controlled by the EB. The process parameters of the remote plasma source covered an RF source power range from 100 W to 600 W. This range did not affect the SiO₂ ER for an electron current below 0.05 mA, but once the electron current had been raised to 0.5 mA, operation of the remote plasma source at 600 W source power produced a higher SiO₂ ER than a 100 W power condition. Since the RF source power controls the degree of CF₄ and O₂ dissociation of the plasma, a high source power provides more reactive neutrals and enhances SiO₂ ER for conditions for which the electron current is sufficiently high. The composition of the F and O radical fluxes can be adjusted by adjusting the CF₄/O₂ flow rate into the ECWR source. The flexibility of adjusting the composition of incident species fluxes and resulting SiO₂ surface chemistry has been demonstrated. The SiO₂ ER peaks at 20% O₂, where the CF₄ oxidation reaction generates the maximum fluorine flux to the SiO₂ surface. By increasing the partial pressure of oxygen decreases the SiO₂ ER because of reduced fluorine atom arrival and re-oxidation of SiO₂.

We developed two prototypical processing cases for etching applications. The first case consists of a sequence of a 100-second remote plasma, followed by 100-second co-introduction of remote plasma and EB, and, lastly, 100-second EB with Ar/CF₄/O₂ only. SiO₂ ER only takes place during the co-introduction step, which validates the importance of a remote plasma source and the concept that electrons activate material removal. The second case studied consisted of a sequence of 100-second Ar/CF₄/O₂ remote plasma treatment and subsequent 70-second EB irradiation. The remote plasma treatment did not lead to SiO₂ etching, but during the following EB irradiation step 2.4 Å SiO₂ were removed in a self-limited manner. The results of these two prototypical processing cases demonstrates the promising etching capability.

The last section characterized the surface chemistry evolution for three different processing sequences using both *in situ* ellipsometry and XPS. The first sequence examined untreated SiO₂ for three EB exposure times. The experimental result revealed that a 30-second EB exposure decreased the oxygen content of SiO₂, likely due to the formation of oxygen vacancies. When the EB exposure time was extended to 200 seconds, this did not lead to further oxygen intensity changes. We also observed EB-induced fluorine uptake from residual fluorine in the vacuum chamber. In this case the surface fluorine intensity increased with the EB exposure time. The second sequence studied involved the surface chemistry transformation for sequential treatments involving remote plasma treatment and EB irradiation. XPS analysis was performed in a spatially resolved fashion after each processing step. The EB step of a SiO₂ surface modified by 80% O₂ remote plasma showed defluorination of the SiO₂ surface. Deeper laying SiO₂ regions still showed fluorine uptake and reduced oxygen intensity as a result of EB bombardment. Finally, the SiO₂ surface chemistry for remote plasma/EB co-introduction was

examined. The spatial composition profiles varied in a fashion that was consistent with the prior results.

The new experimental configuration comprising a remote plasma source and an electron flood gun source has demonstrated extraordinary etching performance. This approach opens up a novel processing approach for atomic scale semiconductor processing. Future studies need to explore the capability of etching different materials, including leveraging the ability to selectively functionalize different materials, and thus achieve materials etching selectivity, along with understanding the corresponding surface reaction mechanisms.

4.5 Acknowledgments

The authors gratefully acknowledge the financial support of this work by ZEISS SMT GmbH. We thank Dr. P. Luan, Dr. C. Li, Dr. A. Pranda, Y. Li, M. Hinshelwood, S.J. Chung, and P. Mercedes for helpful discussions and collaboration. The authors also thank T. Weimar, N. Ballew, and Dr. D. Schamdel from Energy Research Facility at University of Maryland for the design and fabrication of the DPU and PLA units.

Chapter 5: Electron beam-induced etching of SiO₂, Si₃N₄, and poly-Si assisted by CF₄/O₂ remote plasma

Manuscript in preparation

K. Y. Lin, C. Preischl, C. F. Hermanns, D. Rhinow, H.-M. Solowan, T. Hofmann, B. Michael, K. Edinger, and G. S. Oehrlein

K.Y. Lin contributed to the design and conduction of the research, to the analysis of the experimental results, and to the writing of the manuscript.

All authors discussed the results, commented on and made changes to the manuscript.

ABSTRACT

Electron-stimulated desorption (ESD) of the surfaces functionalized by remote plasma is a flexible and novel approach for material removal. In comparison to plasma dry etching which uses the ion-neutral synergistic effect to control material etching, electron beam-induced etching (EBIE) uses an electron-neutral synergistic effect. This approach appears promising for the reduction of plasma damage, including atomic displacement, along with the potential for greater control and lateral resolution. One challenge for EBIE is the limited number of chemical precursor molecules that can be used to produce functionalized materials suitable for etching under electron beam irradiation. In this work we studied a new experimental configuration that

utilizes a remote plasma source to functionalize surfaces in conjunction with electron beam irradiation by an electron flood gun. Etching rates (ER) of SiO_2 , Si_3N_4 , and poly-Si are reported in a broad survey of conditions. The parametric dependence on flood gun and remote plasma source operating parameters on these Si-based materials is evaluated. We also identified the processing parameters that enable realization of material selective removal, e.g. etching selectivity of Si_3N_4 over SiO_2 and poly-Si over SiO_2 . Additionally, surface characterization of etched materials is used to clarify the effects of co-introduction of particle fluxes from the remote plasma and flood gun sources on surface chemistry.

5.1 Introduction

Plasma etching utilizes the ion-neutral synergistic effect to achieve pattern transfer into a thin film material on a substrate, and is extensively used in semiconductor manufacturing.^{11, 111, 151-153} With device miniaturization, plasma-enhanced atomic layer etching (ALE) that temporally separates a surface functionalization step and an ion bombardment step has been developed for the improvement of etching performance, including profile control and etching selectivity.^{12, 14-16, 87, 155} However, plasma in contact with a material intrinsically develops a sheath potential on the material surface, which causes ion bombardment of the substrate and inevitably results in material sputtering by ions and defect formation in the material. Exploiting the electron-neutral synergistic effect by combining fluxes of chemical precursors and energetic electrons for electron beam-induced etching (EBIE) is a possible approach for mitigating plasma damage. One challenge is that there is only a small number of precursor molecules that can be used for EBIE. This is in contrast to the use of stable molecules unsuitable for EBIE that can be readily converted into reactive species in a plasma where these molecules are effectively dissociated. To achieve damage-free pattern transfer and expand available etchants in EBIE, we have developed a new experimental configuration that consists of a remote plasma source and an electron flood gun to utilize EBIE for mitigating plasma damage. A companion study has demonstrated the processing capability of this approach for etching SiO_2 .²¹¹ In that work results were described for simultaneous or sequential remote plasma treatment and electron beam (EB) irradiation.

This work uses the identical experimental configuration and explores the parametric dependence of the etching rate (ER) of SiO_2 , Si_3N_4 , and poly-Si on the electron flood gun and remote plasma source conditions. Material etching selectivity is one of the important criteria of

an etching process. Repair of defective deep ultraviolet (DUV) photomasks, for example, requires a precise, selective material removal for etching of Si_3N_4 with selectivity to SiO_2 .¹⁷⁷ There are many semiconductor process examples where etching selectivity of Si over SiO_2 is an important factor.^{63, 152, 153, 212} This article begins with the evaluation of SiO_2 , Si_3N_4 , poly-Si ER using Ar/ CF_4 / O_2 remote plasma only. A remote plasma source can be used to modify SiO_2 , Si_3N_4 , and poly-Si surfaces by the reactive particle fluxes generated, and the fluxes will depend on plasma power. The impact of the electron flood gun will depend on electron emission current and energy. *In situ* ellipsometry is used to monitor surface modifications and etching of SiO_2 , Si_3N_4 , and poly-Si for various combinations of the operating parameters. Subsequently, we identify for which conditions material etching selectivity of Si_3N_4 over SiO_2 or poly-Si over SiO_2 can be achieved. To mechanistically understand the chemical evolution of these Si-based materials as a function of particle exposure, we employ angle-resolved x-ray photoelectron spectroscopy (XPS) analysis of exposed/etched surfaces for different electron fluxes and precursor chemistries. The characterization results allow us to correlate the etching mechanisms of the Si-based materials with operating conditions.

5.2 Experimental

The experiments were conducted in a vacuum reactor, comprised of a flood gun on the top of the chamber and an electron cyclotron wave resonance (ECWR) remote plasma source on the side. The base pressure of the reactor before a process is at 1×10^{-7} Torr, and the reactor pressure with precursor injection is raised to 1.8 mTorr. The flood gun used is a commercial Kimball Physics EGA-1012 Electron Gun with a standard yttria-coated disc cathode. The

cathode at room temperature can be exposed to atmospheric gases without damage, and the minimum vacuum to run this cathode is 10^{-5} Torr. A differential pump unit (DPU) was designed and installed to improve the vacuum level in the flood gun chamber. The DPU bottom was attached to a custom-made pressure-limited aperture (PLA), establishing a pressure ratio between the reactor (1×10^{-3} Torr) and the flood gun chamber (1×10^{-6} Torr) of about 1000. The remote plasma source consists of a COPRA DN160 ECWR plasma source running at 13.56 MHz radiofrequency (RF) with a neutralization plate.¹⁷⁹ The neutralization plate was made by electrically grounding an aluminum plate covered with Kapton tape and a 4-inch diameter quartz plate at the center to mitigate plasma erosion. The neutralization plate is to filter out the ions generated by the ECWR plasma source, allowing only neutrals to diffuse into the reactor. Prior studies have presented a detailed description of this remote plasma source^{180, 181} and the characterization of etching results on Si-based materials¹⁸²⁻¹⁸⁵. The ECWR effect requires an additional static magnetic field, exploiting the interaction of an electromagnetic wave with plasma.¹⁷⁹ Most experiments were conducted at a 400 W RF source power and 1.8 mT static magnetic fields to the ECWR system. Typical processing parameters for the flood gun were 1000 eV electrons at 0.5 mA emission current (EC) and a 100 V control grid voltage. The sample holder is made of electrically grounded stainless steel with backside cooling achieved by circulating water at 10 °C. A more detailed description of the experimental configuration can be found in the prior chapter.²¹¹

The flood gun consists of a cathode, a control grid, and an anode for independent control of electron energy, EC, and beam convergence angle. The voltage between cathode and anode regulates the electron energy, ranging from 5 eV to 1000 eV. Cathode temperature governs the

flux of emitted electrons, where EC is proportional to working temperature. A high working temperature, however, accelerates the evaporation rate of the yttria coating and reduces the filament lifetime. The maximum EC under 1000 eV electron energy can emit a current up to 1.5 mA. Our experiments employed a 0.5 mA or lower EC to extend the lifetime of the flood gun. Calibration of the beam diameter on a substrate was done by utilizing a customized phosphor screen with 2 mm spacing grids from Kimball Physics. The in-vacuum length of the firing unit was adjusted for meeting a 38.3 mm working distance from the flood gun outlet to a substrate, so a 1000 eV EB with the maximum grid voltage, 100 V, produced a ~5.5 mm beam diameter on the calibration screen. In the case of studying the dependency of electron energies on etching performance, the control grid voltage was adjusted accordingly to keep the spot size constant. Beam current was measured using a Faraday cup connected to a picoammeter. Our experimental setup with the installation of a PLA provides the ratio between beam current and EC of about 70%. Most of the experiments employed 1000 eV electron energy with a 0.5 mA EC and a 100 V grid voltage, generating a current density of 1.5 mA/cm².

In situ ellipsometry with a He-Ne laser operating at a wavelength of 632.8 nm mounted on the reactor allowed us to study surface modification and etching in real-time.³⁸ The ellipsometry laser was aligned using the calibration phosphor screen to a location where a 1000 eV focused electron beam was irradiated. Therefore, the ellipsometer can collect the psi-delta value of the area treated by remote plasma, electron beam, and its combination. The sampling rate of the ellipsometer was set to 5 Hz (0.2 seconds per point) for all experiments.

XPS analyses have been performed at the end of selected treatments to evaluate surface chemistry evolution. The samples were transferred under vacuum using a specimen transfer

device to a Vacuum Generators ESCALAB MK II surface analysis system for XPS measurements. Small area XPS measurement was used to probe surface portions that concurrently interact with particles from the remote plasma but differ in electron beam exposure (diameter of analysis area $\sim 5\text{-}6\text{ mm}$).¹⁸⁶ High resolution scans of the Si2p, C1s, O1s, N1s, and F1s photoelectron spectra were obtained at 20 eV pass energy at an electron take-off angle of 20° (shallow probing depth $\approx 20\text{-}30\text{ \AA}$) and 90° (deep probing depth $\approx 80\text{ \AA}$) with respect to the sample surface. The spectra were fitted using least square fitting after Shirley background subtraction.^{39, 40}

5.3 Results and Discussion

5.3.1 Remote Plasma on SiO₂, Si₃N₄, and Poly-Si

The characterization of the SiO₂, Si₃N₄, and poly-Si ER on remote operating parameters provides a basis before studying etching processes involving co-introduction of remote plasma and EB. Operating conditions were 10 SCCM Ar flow rate, variable CF₄/O₂ gas mixtures with a total CF₄ and O₂ flow rate of 5 SCCM, 1.8 mT DC magnetic fields, and three RF source powers of 100 W, 400 W, and 600 W. The reactor chamber was held at 1.8 mTorr in the presence of the DPU and PLA. Ar is used as a carrier gas to dilute the concentration of gas-phase reactants to minimize erosion of the yttria-coating disc in the flood gun.

Fig 5.1 shows SiO₂, Si₃N₄, and poly-Si ERs under remote plasma as a function of varying the relative CF₄/O₂ flow rates and RF power. The CF₄/O₂ remote plasma produces the maximum fluorine flux at 20% O₂, which has been explained by CF₄ oxidation reactions.^{181, 182, 184, 185} No SiO₂ ER was observed for all oxygen concentrations and RF powers studied (see Fig

5.1(a)). Si_3N_4 etching only took place at a rate of up to ~ 0.2 nm/min for operating conditions of 600 W RF power and with the O_2 concentration ranging from 20% to 60% (Fig 5.1(b)). In contrast, the poly-Si ER peaked at 20% O_2 for the three RF powers examined (see Fig 5.1(c)). The results show that bond strength is a limiting factor for etching reactions, where a high bond strength material requires more energy to activate surface functionalization and material desorption. Poly-Si has a lower bond strength and is highly reactive. The Si ER can be used to provide a lower bound of the fluorine atom flux from the remote plasma source.

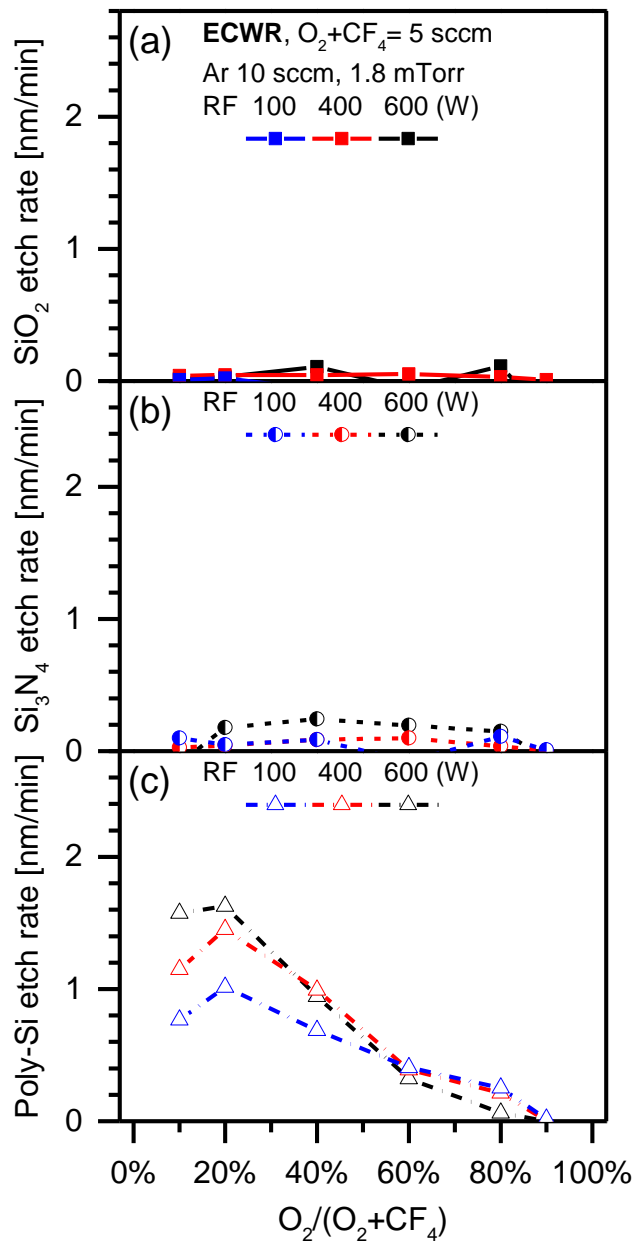


FIG. 5.1. (Color online) The etching rate of (a) SiO_2 , (b) Si_3N_4 , and (c) poly-Si using remote plasma with various relative CF_4/O_2 flow rates and RF powers.

The RF source power is used to control the energy input into the ECWR plasma source, and can be used to manage the degree of dissociation of injected precursors and thus the number

of excited particles in the reactor. Fig 5.1(c) shows that the poly-Si ER peaks at 20% O₂ and is further enhanced as the RF power increased from 100 W to 600 W. For O₂-rich operating conditions, a high RF power promotes the dissociation rate of oxygen in the remote plasma source and admits more oxygen-based neutrals to the reactor. The poly-Si forms an oxidized surface layer for these conditions which reduces the probability of reaction with gas-phase fluorine reactants. For example, the poly-Si ER at 80% O₂ with 600 W RF was lower than seen for 100 W and 400 W discharges, whereas for CF₄-rich plasma the opposite is the case. RF power can be used to regulate the number of exciting neutrals into the reactor for surface modification.

5.3.2 Simultaneous Exposure of Surfaces to Electron Beam and Remote Plasma Fluxes for SiO₂, Si₃N₄, and Poly-Si Etching

After the evaluation of SiO₂, Si₃N₄, and poly-Si etching using remote plasma only, we screened the dependence of ER of the same set materials on processing parameters when EB and remote plasma fluxes interacted simultaneously with surfaces. Similar to the previous chapter, we examined the influence of four process parameters, i.e., EC and electron energy of the electron flood gun, and the RF source power and CF₄/O₂ composition of the gas flow into the remote plasma source. Since the electron convergence angle is regulated by the electron energy and control grid voltage, the grid voltage was adjusted when studying the lowest electron energy by keeping the beam diameter on the substrate unchanged. A study of the parametric dependency provides a fundamental understanding of relative ER among these Si-based materials, which can be used to develop selective material removal.

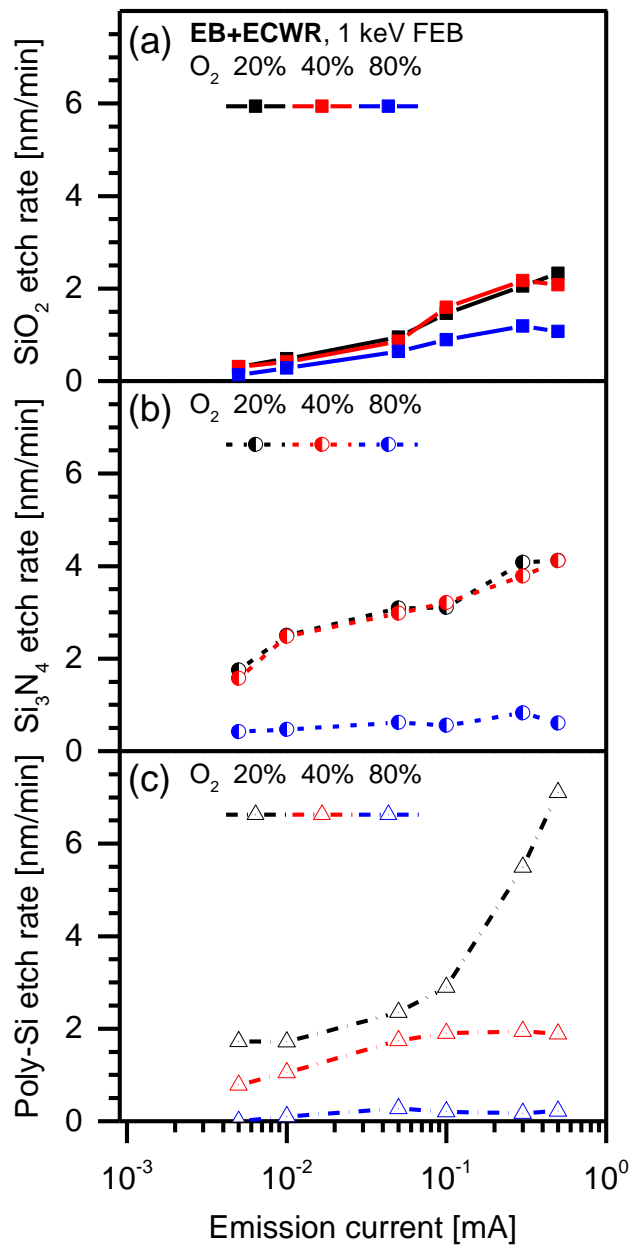


Fig. 5.2. (Color online) The etching rate of (a) SiO₂, (b) Si₃N₄, and (c) poly-Si as a function of electron emission current

Fig 5.2 presents the results of the SiO₂, Si₃N₄, and poly-Si ERs versus emission current and for three different CF₄/O₂ gas compositions. The operating conditions of the remote plasma

was kept at a 400 W source power, 1.8 mT magnetic field, 10 SCCM Ar, and a total CF₄ and O₂ flow rate of 5 SCCM, respectively. The operating parameters of the EB were 1000 eV with the control grid voltage of 100 V. The ER of SiO₂ and Si₃N₄ showed similar behavior, and for 20% O₂ and 40% O₂ comparable ER were seen when the EC was varied from 0.005 mA to 0.5 mA. For 80% O₂ in CF₄/O₂, the SiO₂ and Si₃N₄ ERs were significantly suppressed. The results of the poly-Si ER as a function of EC and for different oxygen concentrations in CF₄/O₂ are shown in Fig 5.2(c). The poly-Si ER strongly depends on both precursor chemistry and electron flux. For 20% O₂ in CF₄/O₂ and 0.5 mA EC, the poly-Si ER is boosted, whereas for O₂-rich operating conditions little etching is seen for all ECs.

Fig 5.3 summarizes the impact of reducing electron energy from 1000 eV to 300 eV on SiO₂, Si₃N₄, and poly-Si ER. The figure shows that both the SiO₂ and Si₃N₄ ER decrease with applied electron energy, whereas the poly-Si ER behaved opposite. We postulate that this trend is related to the combination of the bond strength of materials and the interaction cross-section of electrons with gas-phase reactants and adsorb reactive species. Typically, at an electron energy of about 100 eV, the cross-section for dissociative ionization^{66, 194-198} reaches a maximum. For the material with intermediate or high bond strength, such as SiO₂ and Si₃N₄, 300 eV electrons are more efficient in terms of depositing energy to adsorbates than 1000 eV electrons, and thus enable improved desorption of etching products for reduced electron energies. Poly-Si has a low bond strength and is strongly reactive with fluorine and oxygen atoms. Here 300 eV electrons are more efficient in driving oxidation reactions than desorption reactions. This may explain the observation that 300 eV electrons produce different ER profiles for SiO₂, Si₃N₄, and poly-Si.

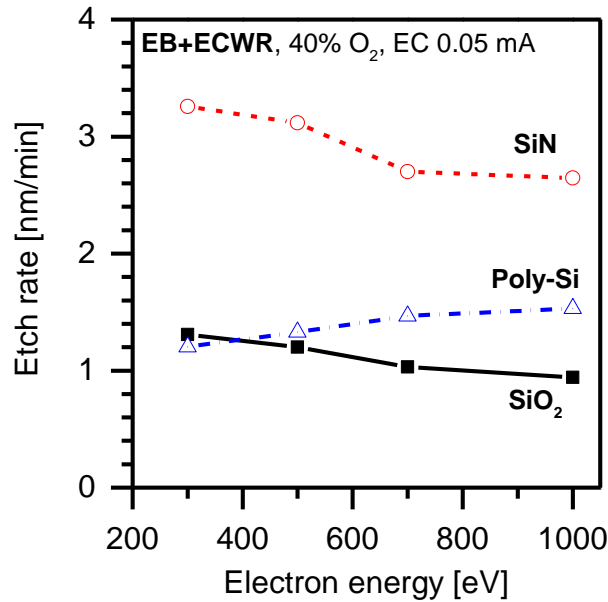


FIG. 5.3. (Color online) The etching rate of SiO₂, Si₃N₄, and poly-Si as a function of electron energy

Next, we explored the effect of remote plasma source operating parameters on SiO₂, Si₃N₄, and poly-Si ER. The operating parameters of the electron flood gun were kept at 1000 eV electron energy, a 0.5 mA EC, and a control grid voltage of 100 V. RF power is used to control the degree of dissociation rate of injected precursor gases and the number of reactive particles in the reactor. We have discussed the profile of the SiO₂ ER under various RF powers and ECs in the previous chapter.²¹¹ The Si₃N₄ and poly-Si ER show a stronger dependence on applied RF power of the remote plasma source, especially in the range between 100 W and 400 W. When more than 600 W RF power was applied to the remote plasma source, the enhancement of the Si₃N₄ and poly-Si ER became insignificant. The behavior may be related to the number of fluorine reactants generated by the remote plasma source. Fig. 5.1(c) shows the poly-Si ER for different oxygen concentrations and RF powers. The use of 400 W and 600 W RF power

produced similar ER for 40% O₂ in CF₄/O₂. It implies that the remote plasma source at a higher RF power does not generate more fluorine atoms in the etching reactor. In contrast, the use of 100 W RF power led to a lower Si ER, implying a lower fluorine atom flux from the remote plasma source that can react with the Si surface. The results of Figs. 5.4(b) and (c) show that only between 100 W and 400 W an increase of the RF power of the remote plasma source strongly enhances both Si₃N₄ and poly-Si ER.

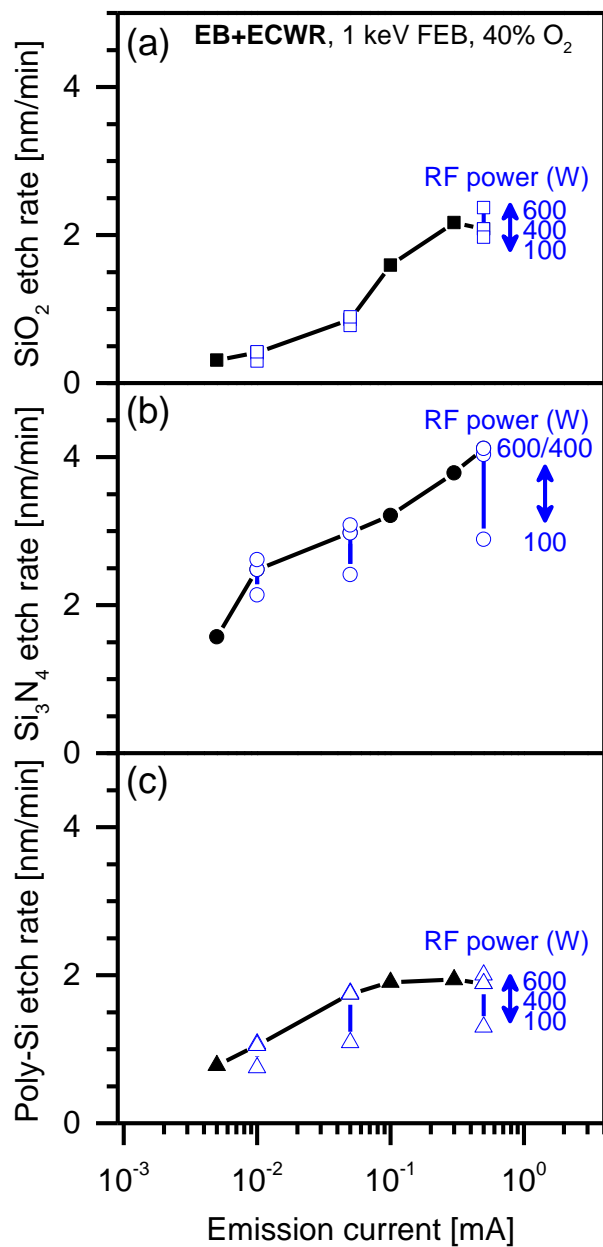


FIG. 5.4. (Color online) The etch rate of (a) SiO₂, (b) Si₃N₄, and (c) poly-Si as a function of emission current and RF power.

Fig 5.5 summarizes SiO₂, Si₃N₄, and poly-Si ERs for various ECs and relative CF₄/O₂ flow rates for simultaneous exposure of these materials to fluxes from the remote plasma and EB

sources. The ER measured for remote plasma source only has been included for reference. Figures 5.5(a) and (b) demonstrate that the co-introduction of particles from the EB and remote sources induces SiO₂ and Si₃N₄ etching. SiO₂ ER is less dependent on the precursor chemistry from the remote plasma, but more strongly depends on EC. For the more reactive Si₃N₄ and poly-Si materials, a stronger role of precursor chemistry for material removal can be seen. For these materials, CF₄-rich operating conditions provided a higher ER than the O₂-rich operating conditions.

Fig 5.5(c) also indicates that there is an effect of EB-induced dissociation that takes place for high EC on poly-Si. The results of using remote plasma only with various RF powers and relative CF₄/O₂ flow rates on poly-Si gives rise to a maximum flux of fluorine reactant, and thus ER, at an oxygen concentration of 20%. When the oxygen concentration is below 20%, fewer dissociated fluorine atomic species are produced because of the reduced importance of oxygen-induced CF₄ oxidization reactions. This reduces the poly-Si ER for these conditions. For co-introduction of remote plasma and EB, the poly-Si ER peaks at 10% O₂ for 0.5 mA EC. We postulate that this enhancement is because the EB is capable to dissociate fluorocarbon molecules through electron-gas and electron-adsorbate interactions and thus increases the poly-Si ER for these conditions.

The variation of SiO₂, Si₃N₄, and poly-Si ER with process parameters of the remote plasma source and electron flood gun has revealed a processing window for material selective removal. The etching selectivity of Si₃N₄ over SiO₂, for example, is an important criterion for DUV photomask repair application, where the EB needs to precisely remove the defective Si₃N₄ pattern without damaging the underlying SiO₂ substrate.¹⁷⁷ The remote plasma source alone can

be used for surface functionalization but did not cause Si_3N_4 and SiO_2 etching. This indicates that the ER for these materials can be strongly localized to the positions where the electron beam strikes the surface.

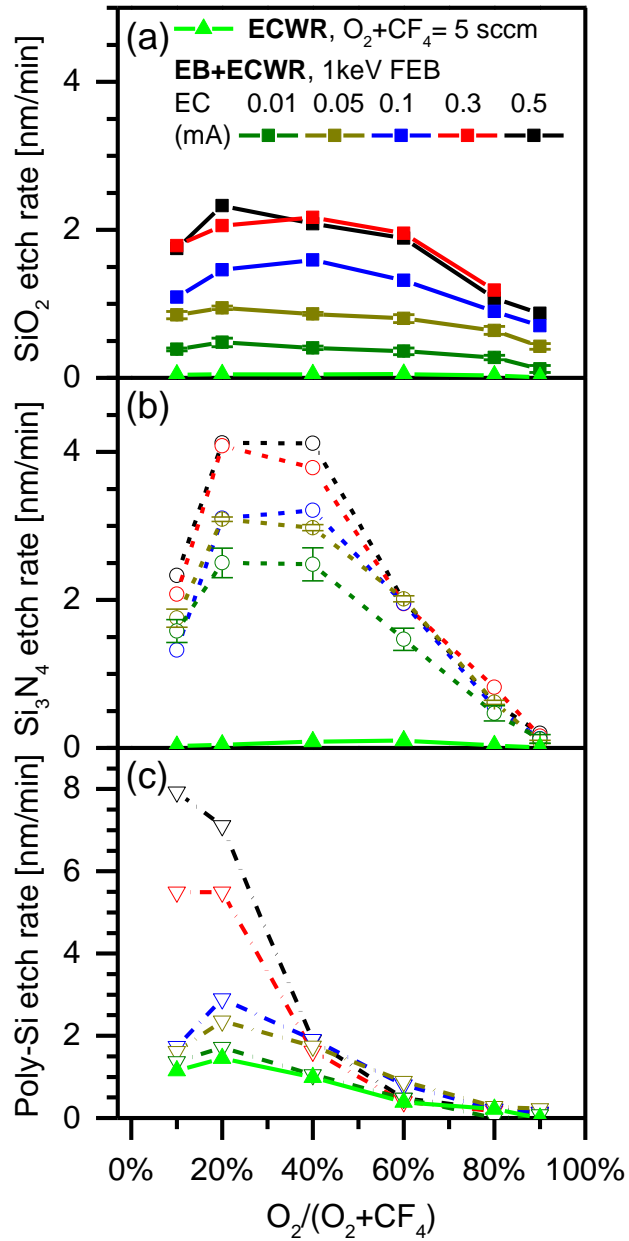


FIG. 5.5. (Color online) The etch rate of (a) SiO₂, (b) Si₃N₄, and (c) poly-Si as a function of emission current and relative CF₄/O₂ flow rate.

5.3.3 Etching Selectivity Development

The development of material etching selectivity by screening the operating variables of the remote plasma and EB sources is important for etching applications. The following discusses the use of combined fluxes from the remote plasma and EB sources for achieving etching selectivity of Si₃N₄ over SiO₂ and poly-Si over SiO₂ by varying CF₄/O₂ composition and EC. The other operating conditions were fixed, i.e. the flood gun was operated with a 1000 eV electron energy and a control grid voltage of 100 V; the remote plasma source RF power was kept at 400 W, 1.8 mT static magnetic fields, 10 SCCM Ar flow rate. The CF₄/O₂ gas flow was varied with the constraint of a total CF₄ and O₂ flow rate of 5 SCCM.

Fig 5.6(a) summarizes the etching selectivity of Si₃N₄ over SiO₂ with various ECs and relative CF₄/O₂ flow rates. When the applied EC ranges between 0.1 mA and 0.5 mA, the measured etching selectivity of Si₃N₄ over SiO₂ for all oxygen concentrations studied falls between 0.1 and 2. The CF₄-rich operating conditions slightly improved the etching selectivity. When the operating conditions were 40% O₂ and 0.01 mA EC, the etching selectivity of Si₃N₄ over SiO₂ has been significantly improved reaching a value of more than 6. The result of Figs. 5.5(a) and (b) clearly illustrates that SiO₂ etching is primarily dependent on the electron flux, whereas Si₃N₄ etching is governed by both electron flux and precursor chemistry. We may apply the CF₄-rich operating condition with a low electron flux on the substrate to promote Si₃N₄ etching but simultaneously to limit the SiO₂ ER.

The results on etching selectivity of poly-Si over SiO₂ with various ECs and relative oxygen concentrations are shown in Fig 5.6(b). The poly-Si ER is governed by both precursor chemistry and EC. The peak poly-Si ER is seen for an O₂ concentration of 10% and 0.5 mA EC. In contrast, SiO₂ ER is driven by the electron flux and shows a slight reduction for oxygen concentrations higher than 20%. By combining these factors it is possible to optimize the poly-Si/SiO₂ etch rate ratio. Figure 5.6(b) shows a maximum etching selectivity of poly-Si over SiO₂ at 10% O₂ with 0.5 mA EC. This result indicates that further improvements of the poly-Si/SiO₂ etching selectivity may be possible by using CF₄-rich operating conditions and an EC of more than 0.5 mA.

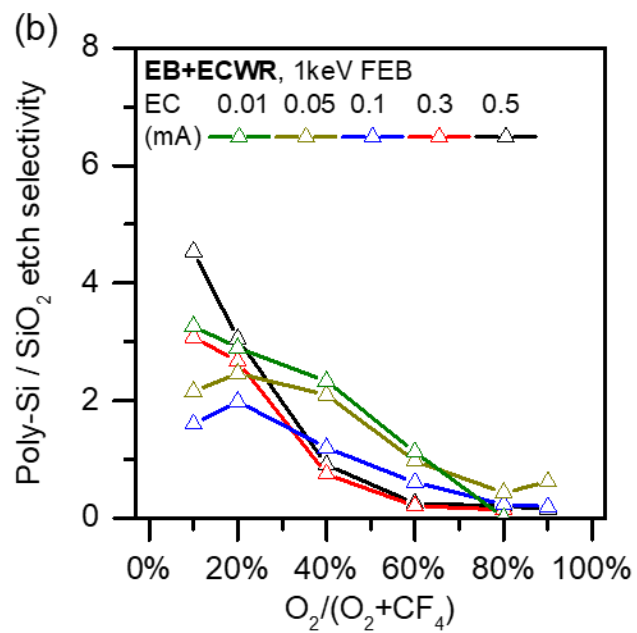
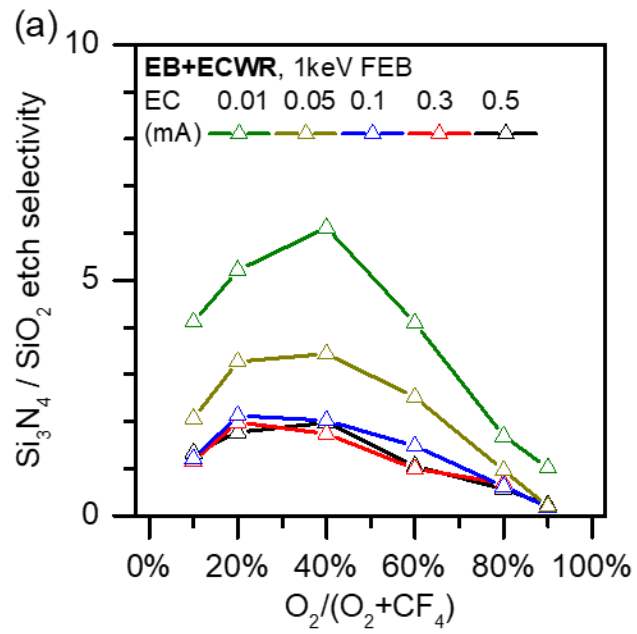


FIG. 5.6. (Color online) The etching selectivity of (a) Si_3N_4 to SiO_2 and (b) poly-Si to SiO_2 as a function of emission current and relative CF_4/O_2 flow rate.

5.3.4 Process Characterization

The development of etching selectivity of Si_3N_4 over SiO_2 and poly-Si over SiO_2 exemplifies the potential of etching processes based on the co-introduction of EB and remote plasma for selective material removal. Here we characterize the surface chemistry of SiO_2 , Si_3N_4 , and poly-Si for different ECs, including 0 mA, 0.01 mA, and 0.5 mA, and oxygen concentrations used for the CF_4/O_2 gas mixture excited in the remote plasma source (20% O_2 and 80% O_2). Each operating condition was applied for 100 seconds to the specimens to ensure that the reaction reached a steady state. Since the electron flux from the flood gun only covers a portion of the specimen (EB diameter ~ 5.5 mm), small area XPS analysis was used to measure the chemical composition of the area under the EB outlet, and compare this with surface portions that only received the neutral fluxes from the remote plasma source. Angle-resolved XPS analysis using take-off angles of 20° and 90° relative to the surface was used to compare the surface chemical evolution as a function of depth by distinguishing the more surface and more bulk sensitive analysis after each processing step. By summarizing these data, we gain insights on the effects of EC and precursor chemistry on these materials that are characterized by different reactivity with fluorine and oxygen atoms.

Figures 5.7(a) and (b) summarize the O1s and F1s spectra of poly-Si using a 20° photoelectron take-off angle. The operating condition of the flood gun was 1000 eV electron energy with three ECs of 0 mA, 0.01 mA, and 0.5 mA; the operating condition of the remote plasma source was 400 W RF power with 20% O_2 . Figure 5.7(a) shows that the poly-Si shows a higher oxygen intensity when the applied EC increases from 0 mA to 0.5 mA. The F1s spectra show that exposure to a high EC reduces the total fluorine intensity and shifts the peak from SiO -

F to Si-F bonding. We postulate that a surface defluorination reaction is driven by electron bombardment, which stimulates desorption of SiF_x-products. These kinds of defluorination reactions are known from plasma-based dry etching, where ion bombardment drives the surface reactions, including fluorination of Si-based materials and desorption of fluorinated etching products.^{5, 8, 40, 75} The desorption of fluorinated products leads to the reduction of the surface fluorine intensity. A higher degree of surface oxidation is found after the use of 0.5 mA EC, even when a low percentage of 20% O₂ is employed. This observation may be related to electron-induced dissociation of O₂. According to this, the EB deposits energy into gas-phase or surface adsorbed oxygen species and atomic oxygen thus produced gives rise to oxidation of the Si substrate. This idea is consistent with the variation of the poly-Si ER shown in Fig 5.5(c) for 0.5 mA EC, the poly-Si ER peaks at 10% O₂. A high EC for the combined EB/remote plasma process induces multiple surface reactions for poly-Si.

Figures 5.7(c) and (d) summarize the O1s and F1s spectra of poly-Si using a 90° photoelectron take-off angle. The O1s spectra show that the deeper region of poly-Si has a comparable, low oxygen intensity after treatments for which three EC were examined. This observation suggests that the EB-induced oxygen dissociation affects primarily the top surface of the Si substrate. A reduction of the F intensity has been observed for a 90° photoelectron take-off angle as compared to the highly surface sensitive measurement. This indicates that both the surface and deeper-lying regions of the poly-Si undergo defluorination reactions with the assistance of EB.

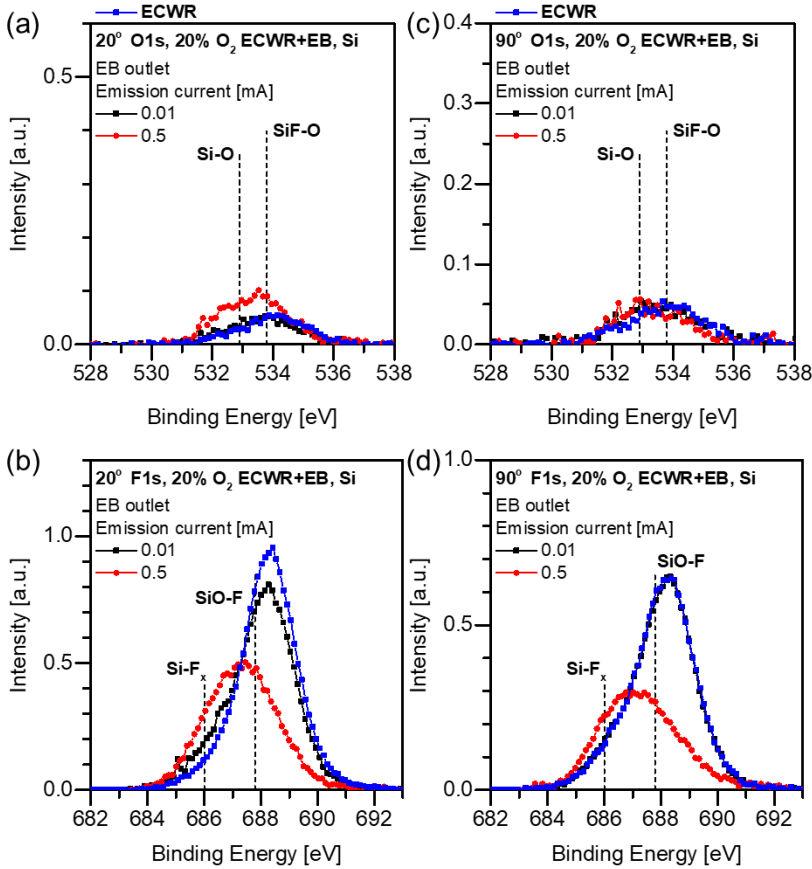


FIG. 5.7. (Color online) XPS spectra for treated poly-Si using 20° take-off angle for (a) O1s and (b) F1s photoelectrons and using 90° take-off angle for (c) O1s and (d) F1s photoelectrons. The operating conditions are 20% O₂ remote plasma and 1000 eV focused EB using emission currents of 0 mA, 0.01 mA, and 0.5 mA, respectively.

To identify the effect of precursor chemistry, XPS analysis was also used to measure poly-Si after the co-introduction process using 80% O₂ for ECs of 0 mA, 0.01 mA, and 0.5 mA. Figs. 5.8(a) and (b) show the O1s and F1s spectra of poly-Si using a 20° photoelectron take-off angle. The surface oxygen intensity increases for higher EC, and overall increases from 0.1 to 0.43. In contrast, the surface fluorine intensity is reduced slightly as the applied EC is increased. The surface spectra suggest that when the precursor chemistry changes from the CF₄-rich

condition to the O₂-rich condition, the main surface reaction shifts from fluorination to oxidation. The gas-phase reactants from the remote plasma source play an important role in the chemical composition of the surface reactive layers. The O1s and F1s spectra shown in Figs. 5.8(c) and (d) for a 90° take-off angle also exhibit a similar trend as what was shown for the more surface-sensitive spectra shown in Figures 5.8(a) and (b). The O₂-rich operating condition promotes oxidation reactions at the surface and to a more limited extent for the deeper-lying regions of poly-Si.

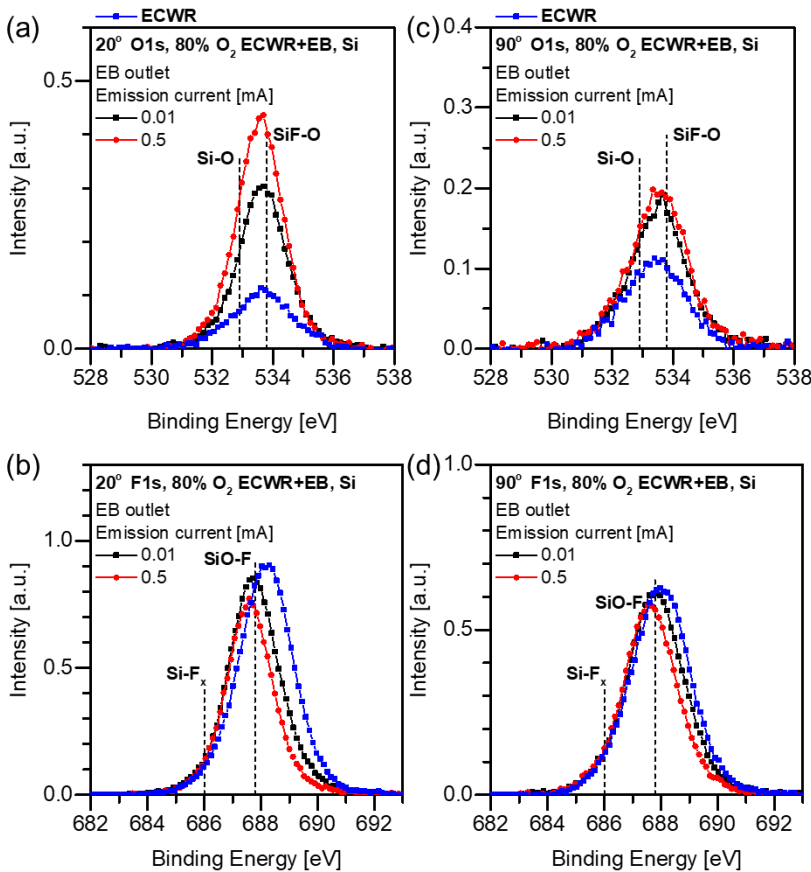


FIG. 5.8. (Color online) XPS spectra for treated poly-Si of using 20° take-off angle for (a) O1s and (b) F1s photoelectrons and using 90° take-off angle for (c) O1s and (d) F1s photoelectrons. The operating condition is combined remote plasma/EB exposure using a CF₄/80% O₂ remote

plasma and 1000 eV focused electrons at emission currents of 0 mA, 0.01 mA, and 0.5 mA, respectively.

We integrated the characteristic XPS peak areas of poly-Si for the three different conditions reported above. This summary is shown in Figs. 5.9(a) and (b), and provide an overview of the effect of electron flux and precursor chemistry on the surface and deeper-lying region of poly-Si. Increasing the EC from 0 mA to 0.5 mA results in a reduction of surface F intensity for both 20% O₂ and 80% O₂ remote plasma operating conditions. The surface oxygen uptake reaches a peak for the combination of 0.5 mA EC and 80% O₂. The area of the O1s and F1s peaks using a 90° take-off angle is shown in Fig 5.9(b). The evolution of the oxygen intensity in poly-Si exhibits a strong dependence on precursor chemistry and EC. Little change of the fluorine intensity is seen at 80% O₂ as the EC was increased. A comparison of these data with those obtained with Si₃N₄ and SiO₂ provides a better understanding of the impact of process parameters for combined remote plasma/EB source treatments on surface chemical composition.

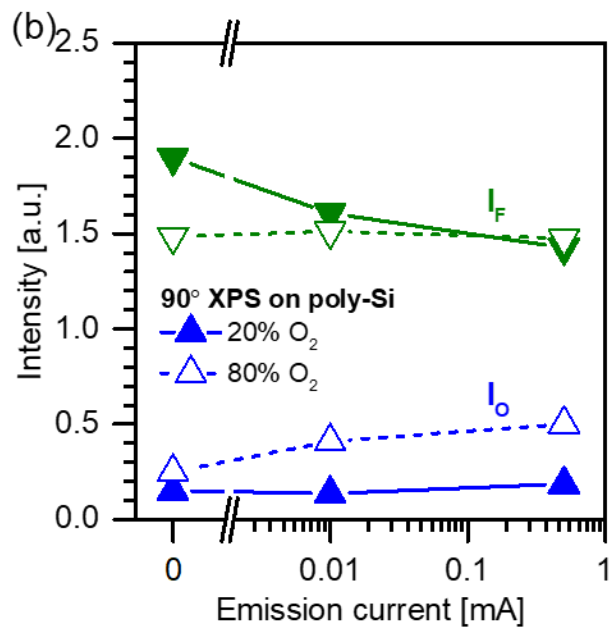
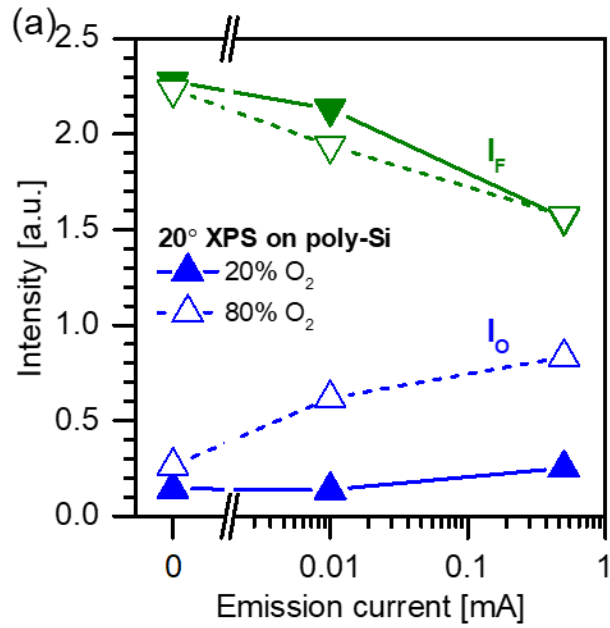


FIG. 5.9. (Color online) Integrated O1s and F1s peak areas obtained with poly-Si after combined remote plasma/EB source treatments using various electron emission currents and CF₄/O₂ ratios. Photoelectrons were collected at (a) 20° and (b) 90° take-off angles.

Integrated O1s and F1s peak areas obtained with Si₃N₄ after combined remote plasma/EB source treatments using various electron emission currents and CF₄/O₂ ratios are shown in Figs. 5.10(a) and (b) for 20° and 90° photoelectron take-off angles, respectively. As a result of EB exposure of Si₃N₄ subjected to remote plasma effluent, the surface (Fig 5.10(a)) experienced some degree of defluorination for both CF₄-rich and O₂-rich remote plasma conditions, with the major reduction of the F peak seen at fairly small electron beam currents. This may be related to the case with which fluorinated etching products can be desorbed from fluorinated Si₃N₄.¹ For 80% O₂ to the remote plasma source, the surface O intensity is noticeably increased, while the surface N intensity is reduced. This effect is most pronounced at 0.5 mA EC. On the other hand, for 20% O₂ to the remote plasma source little change in both O and N intensities is seen for all applied ECs. This observation suggests that for combined remote plasma/EB source treatments using O₂-rich and high EC conditions, nitrogen sites on the surface Si₃N₄ are replaced by oxygen with the assistance of EB.

Figure 5.10(b) shows the evolution of the deeper-lying region of Si₃N₄ for combined remote plasma/EB source treatment. The oxygen and nitrogen intensities depend less on applied EC but more on the composition of precursor chemistry. When 80% O₂ is used, the oxygen level is increased and nitrogen is reduced relative to conditions when 20% O₂ is employed. The fluorine intensity for surface and more bulk-sensitive measurements showed little change when a 0.01 mA EC was applied to the substrate. Overall, combined remote plasma/EB source treatments caused the surface chemical evolution of Si₃N₄ to depend strongly on the precursor chemistry of the remote plasma source.

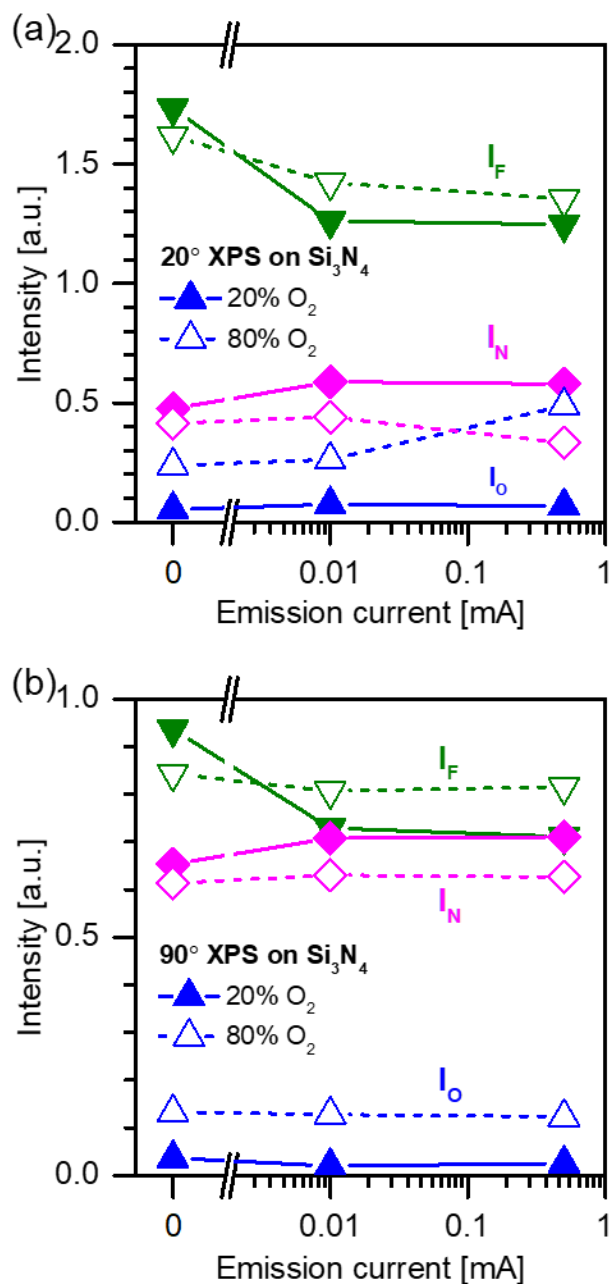


FIG. 5.10. (Color online) Integrated O1s and F1s peak areas obtained with Si₃N₄ after combined remote plasma/EB source treatments using various electron emission currents and CF₄/O₂ ratios. Photoelectrons were collected at (a) 20° and (b) 90° take-off angles.

Finally, the chemical evolution of SiO₂ after combined remote plasma/EB source treatments using take-off angles of 20° and 90°, respectively, is described. Figure 5.11(a) summarizes the surface oxygen and fluorine intensities versus EC and precursor chemistry, respectively. Overall, the elemental variations seen are weaker for SiO₂ than for Si₃N₄ and poly-Si, but there is defluorination evident as the applied EC is increased up to 0.5 mA for both 20% O₂ and 80% O₂ admitted to the remote plasma source.

Figure 5.11(b) shows the oxygen and fluorine intensities of SiO₂ when using a 90° photoelectron take-off angle for the combined remote plasma/EB process. For a 20% O₂ remote plasma chemistry, the oxygen and fluorine intensities show little dependence on the applied EC over the range from 0 mA to 0.5 mA. In contrast, for the 80% O₂ operating condition, a slightly higher fluorine intensity and the corresponding reduction of the oxygen intensity are seen as the EC was increased from 0 mA to 0.5 mA. This observation may be related to the SiO₂ surface being passivated by oxidation when using 80% O₂ remote plasma and a high EC of 0.5 mA. In this case, fluorine reactants from the adsorbate may only be able to diffuse to the deeper-lying regions of SiO₂ with the assistance of EB, thus increasing the fluorine intensity for those conditions. It is possible that this behavior is not seen for CF₄-rich remote plasma operating conditions since in that case the reactive surface species are rapidly removed by electron bombardment from the EB source.

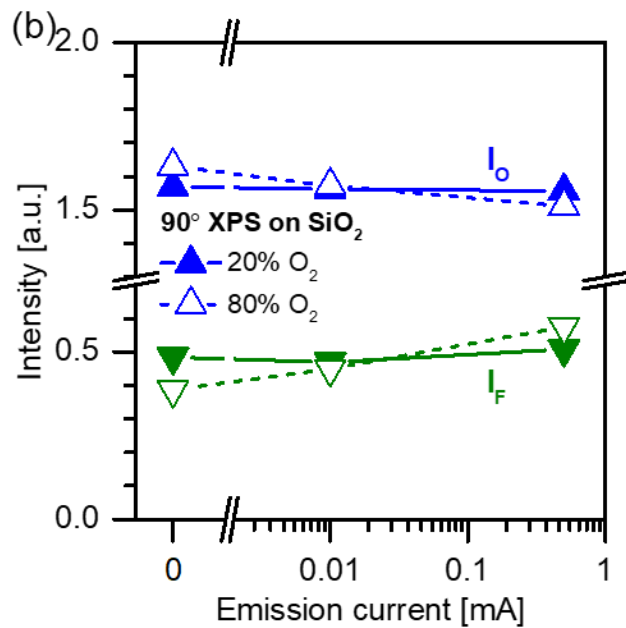
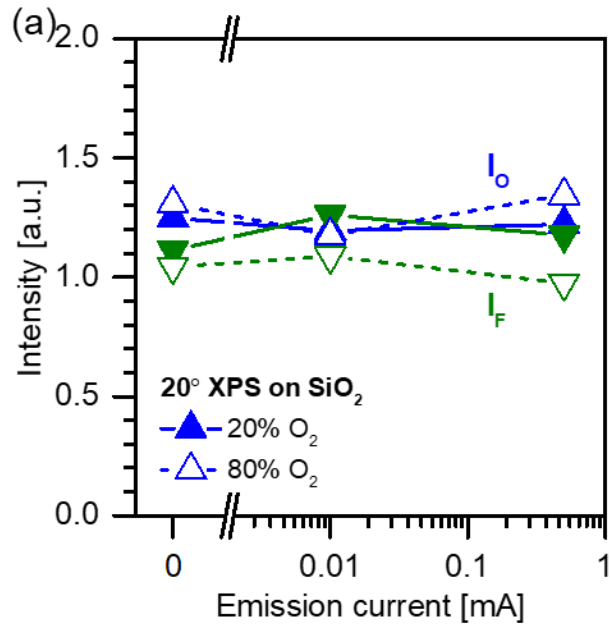


FIG. 5.11. (Color online) Integrated O1s and F1s peak areas obtained with SiO₂ after combined remote plasma/EB source treatments using various electron emission currents and CF₄/O₂ ratios. Photoelectrons were collected at (a) 20° and (b) 90° take-off angles.

5.4 Summary and Conclusions

This work described the use of a new experimental configuration that integrates a remote plasma source and an electron flood gun for enabling EBIE of SiO₂, Si₃N₄, and poly-Si with Ar/CF₄/O₂ remote plasma. The dependence of ER of Si-based materials on operating parameters of the flood gun and remote plasma source was evaluated. The SiO₂ ER is primarily dependent on the applied EC, where a high EC generally produces a faster ER than a low EC. For more reactive poly-Si, for which spontaneous etching rates in the remote plasma environment are high, the ER is governed by both precursor chemistry and electron flux. The survey of process parameters for poly-Si showed that the peak ER was seen for 10% O₂ to the remote plasma source and 0.5 mA EC. For Si₃N₄ which is of intermediate reactivity between SiO₂ and poly-Si, the ER is governed by both electron and fluorine fluxes. At 40% O₂ remote plasma composition and 0.01 mA EC, the Si₃N₄ ER increases from 0 nm/min to 2.5 nm/min. The behavior differences of SiO₂, Si₃N₄, and poly-Si ER relative to process parameters used opens a large window in which selective material removal is possible, and of practical use for DUV photomask repair applications where etching selectivity of Si₃N₄ over SiO₂ is required. Materials etching selectivity can be tailored by optimizing applied EC and relative oxygen concentration of the remote plasma gas mixture. A similar approach of optimizing the relative oxygen concentration and EC can also be used to improve the etching selectivity of poly-Si over SiO₂. The results of angle-resolved XPS analysis in which the chemical composition of the reacted layers was examined for different probing depths are also reported. The experimental results show that poly-Si exhibited large changes of the characteristic elemental peaks under the influence of precursor chemistry and EB. On the other hand, for unreactive SiO₂ only minor variations were seen.

5.5 Acknowledgments

The authors gratefully acknowledge the financial support of this work by ZEISS SMT GmbH. We thank Dr. P. Luan, Dr. C. Li, Dr. A. Pranda, Y. Li, M. Hinshelwood, S.J. Chung, and P. Mercedes for helpful discussions and collaboration. The authors also thank T. Weimar, N. Ballew, and Dr. D. Schamdel from Energy Research Facility at University of Maryland for the design and fabrication of the DPU and PLA units.

Chapter 6: Conclusions and Future Work

The investigations presented in this dissertation are relevant to future development of semiconductor processing applications. This work identified the surface evolution of FCs, HFCs, and a mixture of FCs and H₂ on Si-based materials in an ALE sequence, integrated substrate-selective deposition into an ALE sequence, and, for the first time, demonstrated EBIE of SiO₂, Si₃N₄ and Si with the assistance of Ar/CF₄/O₂ remote plasma.

In Chapter 2, we studied the potential of utilizing complex precursor chemistries in ALE for achieving etching selectivity of SiO₂ over Si and SiO₂ over Si₃N₄. The mixing of chemical precursor approach that is often used in CW plasma for improving etching selectivity of SiO₂ over Si did not succeed for ALE conditions. Instead, the C₄F₈/H₂ mixture degraded the etching selectivity due to interaction of residual hydrogen with the functionalized surface that suppressed the formation of a passivation layer. In contrast, C₃H₃F₃ delivered a reduced F/C ratio for deposited films and rapidly formed a passivation layer on Si. This work suggests that the structure and composition of HFC precursors in ALE offer significant advantages for achieving selective ALE.

In Chapter 3, a review of the works in area-selective atomic layer deposition inspired a concept that selective ALE can be developed by leveraging substrate-selective deposition. We studied the deposition yield difference between HfO₂ and Si by examining two sets of fluorocarbon plasmas, i.e., C₄F₈/CH₄ and CHF₃/CHF₄, in an ALE sequence. The C₄F₈/CH₄ mixture deposited a comparable thickness on both materials, whereas the CHF₃/CH₄ mixture only deposited on the Si surface. The results of XPS analysis confirmed this observation and showed that the CHF₃/CH₄ mixture could fluorinate HfO₂ without deposition. By optimizing the

processing parameters, the CHF_3/CH_4 -based ALE successfully removed a 3-nm HfO_2 layer with selectivity to Si. This work demonstrates the concept of selective ALE based on substrate-selective deposition.

Chapter 4 developed a new experimental configuration that combines a remote plasma source and an electron flood gun for EBIE of SiO_2 with $\text{Ar}/\text{CF}_4/\text{O}_2$ precursors. We have screened the parametric dependence on the electron flood gun and remote plasma source operating conditions to measure SiO_2 ER under simultaneous exposure to both sources. SiO_2 etching results obtained for various ECs and electron energies of the flood gun revealed that the SiO_2 ER was correlated to both electron flux and chemical reactant transport. The RF source power and CF_4/O_2 flow rate in the remote plasma source profoundly influenced the flux and chemistry of reactants to the reacting surface. Here, a 20% $\text{O}_2/\text{CF}_4/\text{Ar}$ remote plasma produced a rich fluorine flux to the reacting surface and accelerated SiO_2 ER. We also demonstrated two prototypical processing cases for concise SiO_2 etching and ALE of SiO_2 . The spatial distribution of characteristic elements after a processing sequence has been investigated to understand the surface and underlying reactions in SiO_2 .

Chapter 5 investigated the new experimental configuration that consists of an electron flood gun and a remote plasma source for EBIE of SiO_2 , Si_3N_4 , and poly-Si with $\text{Ar}/\text{CF}_4/\text{O}_2$ precursors. Following the similar approach as used in the previous chapter, we have surveyed the processing parameters of the remote plasma and EB sources using the co-introduction process to measure SiO_2 , Si_3N_4 , and poly-Si ERs. The profile of SiO_2 etching results with various ECs and relative CF_4/O_2 flow rates show that the SiO_2 ER is primarily dependent on the electron flux; in contrast, Si_3N_4 and poly-Si ERs are governed by both precursor chemistry and electron flux. By

optimizing the relative CF_4/O_2 flow ratio of the remote plasma source and the EC of the EB source, we exemplified that the co-introduction process can achieve etching selectivity of Si_3N_4 over SiO_2 and poly-Si over SiO_2 . The characterization of characteristic elements on poly-Si, Si_3N_4 , and SiO_2 after various operating conditions has been evaluated to understand the effect of precursor chemistry and electron beam.

Future Work

This work researched electronic material etching using ion- or electron-activated surface reaction and product desorption. We found that a combination of remote plasma surface functionalization and electron-stimulated desorption is possibly the most promising method for semiconductor etching applications. Going to the next step, we may consider three developments. Adding a residual gas analyzer (RGA) at downstream of the reactor monitors etching products in real-time. The current characterization method uses *in situ* ellipsometry and XPS analysis to clarify the surface modification and etching, but the desorption pathway of etching products has limited understanding. Additionally, RGA can directly measure the flux of neutrals generated from remote plasma, clarifying a correlation between gas-phase reactants and adsorbates.

Another item is to realize an ALE process by modularizing the remote plasma source that enables a pulsed injection of reactants into the reactor. An EB-enhanced ALE sequence consists of two steps: a remote plasma treatment step and sequentially an EB irradiation step. In the current experimental configuration, controlling the injection of neutrals from remote plasma is based on the source power ON and OFF, where plasma ignition is time-consuming. If the remote

plasma source can be retrofitted by installing an exclusive pump system and a shutter on the outlet of the remote plasma source, the injection of reactants can be managed by shutter ON and OFF without turning off plasma. A fast switch between remote plasma treatment and EB irradiation establishes cyclic processes for ALE. The last item is needed to understand the reaction pathways of etching product removal by comparing electron- and thermal-activated desorption. Miyoshi et al. presented ALE of Si_3N_4 in an etcher that consists of a remote plasma source and an infrared (IR) lamp.^{69, 70, 213-215} The HFC-based remote plasma produced the reactive neutrals that selectively modify the Si_3N_4 surface, forming an ammonium fluorosilicate layer $(\text{NH}_4)_2\text{SiF}_6$. A sequential IR annealing step heats the sample to a temperature for enabling desorption of ammonium fluorosilicate in a self-limited manner. Repeating these two steps can achieve the desired etching amount of Si_3N_4 with selectivity to SiO_2 .

Our system uses remote plasma for surface modification, but the etching step is done by EB irradiation. An early trial utilizing $\text{Ar}/\text{CH}_3\text{F}/\text{O}_2$ remote plasma with EB did not develop promising etching selectivity of Si_3N_4 over SiO_2 in comparison with $\text{Ar}/\text{CF}_4/\text{O}_2$ remote plasma with EB. If we can understand the difference of desorption pathways between EB and IR, it will expand the knowledge of surface modification through complex precursor chemistries and promote the realization of more selective ALE applications useful for both isotropic and anisotropic pattern transfer.

Bibliography

- ¹Y.-R. Luo, *Handbook of bond dissociation energies in organic compounds*. (CRC Press, Boca Raton, 2003).
- ²T. Matsuura, J. Murota, Y. Sawada, T. Ohmi, *Appl Phys Lett* **63**, 2803 (1993).
- ³S. D. Athavale, D. J. Economou, *Journal of Vacuum Science & Technology a-Vacuum Surfaces and Films* **13**, 966 (1995).
- ⁴S. D. Athavale, D. J. Economou, *J Vac Sci Technol B* **14**, 3702 (1996).
- ⁵D. Metzler, C. Li, S. Engelmann, R. L. Bruce, E. A. Joseph, G. S. Oehrlein, *J Chem Phys* **146**, 052801 (2017).
- ⁶D. Metzler, K. Uppireddi, R. L. Bruce, H. Miyazoe, Y. Zhu, W. Price, E. S. Sikorski, C. Li, S. U. Engelmann, E. A. Joseph, G. S. Oehrlein, *J Vac Sci Technol A* **34**, 01b102 (2016).
- ⁷D. Metzler, C. Li, S. Engelmann, R. L. Bruce, E. A. Joseph, G. S. Oehrlein, *J Vac Sci Technol A* **34**, 01b101 (2016).
- ⁸D. Metzler, R. L. Bruce, S. Engelmann, E. A. Joseph, G. S. Oehrlein, *J Vac Sci Technol A* **32**, 020603 (2014).
- ⁹M. Schaepkens, G. S. Oehrlein, *Journal of The Electrochemical Society* **148**, C211 (2001).
- ¹⁰A. Sankaran, M. J. Kushner, *Appl Phys Lett* **82**, 1824 (2003).
- ¹¹K. Nojiri, *Dry Etching Technology for Semiconductors*. (Springer International Publishing, New York, 2015).
- ¹²G. S. Oehrlein, D. Metzler, C. Li, *Ecs J Solid State Sc* **4**, N5041 (2015).
- ¹³J. Robertson, *The European Physical Journal Applied Physics* **28**, 265 (2004).
- ¹⁴C. T. Carver, J. J. Plombon, P. E. Romero, S. Suri, T. A. Tronic, R. B. Turkot, *Ecs J Solid State Sc* **4**, N5005 (2015).
- ¹⁵K. J. Kanarik, T. Lill, E. A. Hudson, S. Sriraman, S. Tan, J. Marks, V. Vahedi, R. A. Gottscho, *J Vac Sci Technol A* **33**, 020802 (2015).
- ¹⁶S. U. Engelmann, R. L. Bruce, M. Nakamura, D. Metzler, S. G. Walton, E. A. Joseph, *Ecs J Solid State Sc* **4**, N5054 (2015).
- ¹⁷P. Patnaik, *Handbook of inorganic chemicals*. (McGraw-Hill New York, 2003), vol. 529.
- ¹⁸J. H. Chen, W. J. Yoo, Z. Y. L. Tan, Y. Q. Wang, D. S. H. Chan, *J Vac Sci Technol A* **22**, 1552 (2004).
- ¹⁹T. E. Madey, J. T. Yates, *Journal of Vacuum Science and Technology* **8**, 525 (1971).
- ²⁰A. A. Martin, M. Toth, *ACS Appl Mater Interfaces* **6**, 18457 (2014).
- ²¹S. J. Randolph, J. D. Fowlkes, P. D. Rack, *Critical Reviews in Solid State and Materials Sciences* **31**, 55 (2007).
- ²²I. Utke, P. Hoffmann, J. Melngailis, *J Vac Sci Technol B* **26**, 1197 (2008).
- ²³M. Toth, *Appl Phys a-Mater* **117**, 1623 (2014).
- ²⁴B. Pfeiffer, *Journal of Applied Physics* **37**, 1624 (1966).
- ²⁵K. J. Kanarik, T. Lill, E. A. Hudson, S. Sriraman, S. Tan, J. Marks, V. Vahedi, R. A. Gottscho, *Journal of Vacuum Science & Technology A: Vacuum, Surfaces, and Films* **33**, 020802 (2015).
- ²⁶C. Li, R. Gupta, V. Pallem, G. S. Oehrlein, *J Vac Sci Technol A* **34**, 031306 (2016).
- ²⁷H.-J. Lee, H. Motomura, K. Tachibana, *Japanese Journal of Applied Physics* **37**, 4522 (1998).

- ²⁸F. Gaboriau, G. Cartry, M. C. Peignon, C. Cardinaud, *Journal of Vacuum Science & Technology B: Microelectronics and Nanometer Structures* **20**, 1514 (2002).
- ²⁹D. Metzler, C. Li, C. S. Lai, E. A. Hudson, G. S. Oehrlein, *Journal of Physics D-Applied Physics* **50**, 254006 (2017).
- ³⁰C. Li, D. Metzler, C. S. Lai, E. A. Hudson, G. S. Oehrlein, *J Vac Sci Technol A* **34**, 041307 (2016).
- ³¹Y. Ishii, K. Okuma, T. Saldana, K. Maeda, N. Negishi, J. Manos, *Japanese Journal of Applied Physics* **56**, 06hb07 (2017).
- ³²W. H. Kim, D. Sung, S. Oh, J. Woo, S. Lim, H. Lee, S. F. Bent, *J Vac Sci Technol A* **36**, 01b104 (2018).
- ³³S. Rauf, T. Sparks, P. L. G. Ventzek, V. V. Smirnov, A. V. Stengach, K. G. Gaynullin, V. A. Pavlovsky, *Journal of Applied Physics* **101**, 033308 (2007).
- ³⁴A. Agarwal, M. J. Kushner, *Journal of Vacuum Science & Technology A: Vacuum, Surfaces, and Films* **27**, 37 (2009).
- ³⁵T. E. F. M. Standaert, P. J. Matsuo, S. D. Allen, G. S. Oehrlein, T. J. Dalton, *Journal of Vacuum Science & Technology a-Vacuum Surfaces and Films* **17**, 741 (1999).
- ³⁶S. Engelmann, R. L. Bruce, T. Kwon, R. Phaneuf, G. S. Oehrlein, Y. C. Bae, C. Andes, D. Graves, D. Nest, E. A. Hudson, P. Lazzeri, E. Iacob, M. Anderle, *Journal of Vacuum Science & Technology B: Microelectronics and Nanometer Structures* **25**, 1353 (2007).
- ³⁷M. Kawakami, D. Metzler, C. Li, G. S. Oehrlein, *J Vac Sci Technol A* **34**, 040603 (2016).
- ³⁸H. Tompkins, E. A. Irene, *Handbook of ellipsometry*. (William Andrew, Norwich, NY, 2005).
- ³⁹S. W. Robey, G. S. Oehrlein, *Surface Science* **210**, 429 (1989).
- ⁴⁰T. E. F. M. Standaert, M. Schaepkens, N. R. Rueger, P. G. M. Sebel, G. S. Oehrlein, J. M. Cook, *Journal of Vacuum Science & Technology a-Vacuum Surfaces and Films* **16**, 239 (1998).
- ⁴¹M. Schaepkens, T. E. F. M. Standaert, N. R. Rueger, P. G. M. Sebel, G. S. Oehrlein, J. M. Cook, *Journal of Vacuum Science & Technology a-Vacuum Surfaces and Films* **17**, 26 (1999).
- ⁴²J. L. Vossen, J. H. Thomas, J. S. Maa, O. R. Mesker, G. O. Fowler, *Journal of Vacuum Science & Technology A: Vacuum, Surfaces, and Films* **1**, 1452 (1983).
- ⁴³K. Ninomiya, K. Suzuki, S. Nishimatsu, O. Okada, *Journal of Applied Physics* **58**, 1177 (1985).
- ⁴⁴N. Posseme, T. Chevolleau, O. Joubert, L. Vallier, P. Mangiagalli, *Journal of Vacuum Science & Technology B: Microelectronics and Nanometer Structures* **21**, 2432 (2003).
- ⁴⁵M. Sumiya, R. Bruce, S. Engelmann, F. Weilnboeck, G. S. Oehrlein, *Journal of Vacuum Science & Technology B: Microelectronics and Nanometer Structures* **26**, 1978 (2008).
- ⁴⁶C. D. Wagner, L. E. Davis, M. V. Zeller, J. A. Taylor, R. H. Raymond, L. H. Gale, *Surf Interface Anal* **3**, 211 (1981).
- ⁴⁷D. Humbird, D. B. Graves, *Journal of Applied Physics* **96**, 2466 (2004).
- ⁴⁸D. Humbird, D. B. Graves, X. F. Hua, G. S. Oehrlein, *Appl Phys Lett* **84**, 1073 (2004).
- ⁴⁹M. J. Kushner, *Journal of Applied Physics* **53**, 2923 (1982).
- ⁵⁰G. S. Oehrlein, H. L. Williams, *Journal of Applied Physics* **62**, 662 (1987).

- ⁵¹F. H. Bell, O. Joubert, G. S. Oehrlein, Y. Zhang, D. Vender, *Journal of Vacuum Science & Technology A: Vacuum, Surfaces, and Films* **12**, 3095 (1994).
- ⁵²T. Fukasawa, A. Nakamura, H. Shindo, Y. Horiike, *Japanese Journal of Applied Physics* **33**, 2139 (1994).
- ⁵³K. Kubota, H. Matsumoto, H. Shindo, S. Shingubara, Y. Horiike, *Japanese Journal of Applied Physics* **34**, 2119 (1995).
- ⁵⁴H. H. Doh, J. H. Kim, S. H. Lee, K. W. Whang, *Journal of Vacuum Science & Technology a-Vacuum Surfaces and Films* **14**, 2827 (1996).
- ⁵⁵G. S. Oehrlein, S. W. Robey, J. L. Lindstrom, K. K. Chan, M. A. Jaso, G. J. Scilla, *J Electrochem Soc* **136**, 2050 (1989).
- ⁵⁶H. Jansen, H. Gardeniers, M. Deboer, M. Elwenspoek, J. Fluitman, *J Micromech Microeng* **6**, 14 (1996).
- ⁵⁷J. W. Coburn, H. F. Winters, *Journal of Applied Physics* **50**, 3189 (1979).
- ⁵⁸H. F. Winters, J. W. Coburn, *Surface Science Reports* **14**, 162 (1992).
- ⁵⁹H. F. Winters, *Journal of Vacuum Science & Technology B: Microelectronics and Nanometer Structures* **3**, 1376 (1985).
- ⁶⁰H. F. Winters, *Journal of Vacuum Science & Technology B: Microelectronics and Nanometer Structures* **1**, 469 (1983).
- ⁶¹J. W. Coburn, H. F. Winters, *Annual Review of Materials Science* **13**, 91 (1983).
- ⁶²S. Salahuddin, K. Ni, S. Datta, *Nature Electronics* **1**, 442 (2018).
- ⁶³K. Ishikawa, K. Karahashi, T. Ishijima, S. I. Cho, S. Elliott, D. Hausmann, D. Mocuta, A. Wilson, K. Kinoshita, *Japanese Journal of Applied Physics* **57**, 06ja01 (2018).
- ⁶⁴N. Otsuka, Y. Oyama, H. Kikuchi, J.-I. Nishizawa, K. Suto, *Japanese Journal of Applied Physics* **37**, L1509 (1998).
- ⁶⁵H. Shin, W. Zhu, V. M. Donnelly, D. J. Economou, *Journal of Vacuum Science & Technology A: Vacuum, Surfaces, and Films* **30**, 021306 (2012).
- ⁶⁶S. J. Randolph, J. D. Fowlkes, P. D. Rack, *Journal of Applied Physics* **98**, 034902 (2005).
- ⁶⁷H. Nishino, N. Hayasaka, H. Okano, *Journal of Applied Physics* **74**, 1345 (1993).
- ⁶⁸Y. Lee, S. M. George, *ACS Nano* **9**, 2061 (2015).
- ⁶⁹K. Shinoda, M. Izawa, T. Kanekiyo, K. Ishikawa, M. Hori, *Applied Physics Express* **9**, 106201 (2016).
- ⁷⁰N. Miyoshi, H. Kobayashi, K. Shinoda, M. Kurihara, T. Watanabe, Y. Kouzuma, K. Yokogawa, S. Sakai, M. Izawa, *Japanese Journal of Applied Physics* **56**, 06hb01 (2017).
- ⁷¹S. M. George, Y. Lee, *ACS Nano* **10**, 4889 (2016).
- ⁷²W. J. Lu, Y. Lee, J. Murdzek, J. Gertsch, A. Vardi, L. S. Kong, S. M. George, J. A. Del Alamo, in *Int El Devices Meet.* (2018), pp. 39.01.01.
- ⁷³K. J. Kanarik, S. Tan, R. A. Gottscho, *J Phys Chem Lett* **9**, 4814 (2018).
- ⁷⁴A. Agarwal, M. J. Kushner, *J Vac Sci Technol A* **27**, 37 (2009).
- ⁷⁵R. J. Gasvoda, A. W. Van De Steeg, R. Bhowmick, E. A. Hudson, S. Agarwal, *ACS Appl Mater Interfaces* **9**, 31067 (2017).
- ⁷⁶K. Y. Lin, C. Li, S. Engelmann, R. L. Bruce, E. A. Joseph, D. Metzler, G. S. Oehrlein, *J Vac Sci Technol A* **36**, 040601 (2018).
- ⁷⁷C. M. Huard, S. Sriraman, A. Paterson, M. J. Kushner, *J Vac Sci Technol A* **36**, 06b101 (2018).

- ⁷⁸N. Kuboi, T. Tatsumi, J. Komachi, S. Yamakawa, *J Vac Sci Technol A* **37**, 051004 (2019).
- ⁷⁹R. J. Gasvoda, Y. G. P. Verstappen, S. Wang, E. A. Hudson, S. Agarwal, *J Vac Sci Technol A* **37**, 051003 (2019).
- ⁸⁰K. Takahashi, K. Ono, Y. Setsuhara, *J Vac Sci Technol A* **23**, 1691 (2005).
- ⁸¹R. M. Martin, J. P. Chang, *J Vac Sci Technol A* **27**, 209 (2009).
- ⁸²R. M. Martin, H. O. Blom, J. P. Chang, *J Vac Sci Technol A* **27**, 217 (2009).
- ⁸³N. Marchack, J. P. Chang, *Annu Rev Chem Biomol Eng* **3**, 235 (2012).
- ⁸⁴M. Hélot, T. Chevolleau, L. Vallier, O. Joubert, E. Blanquet, A. Pisch, P. Mangiagalli, T. Lill, *Journal of Vacuum Science & Technology A: Vacuum, Surfaces, and Films* **24**, 30 (2006).
- ⁸⁵P. Bodart, G. Cunge, O. Joubert, T. Lill, *Journal of Vacuum Science & Technology A: Vacuum, Surfaces, and Films* **30**, 020602 (2012).
- ⁸⁶A. Chen, *Solid-State Electronics* **125**, 25 (2016).
- ⁸⁷T. Faraz, F. Roozeboom, H. C. M. Knoop, W. M. M. Kessels, *Ecs J Solid State Sc* **4**, N5023 (2015).
- ⁸⁸A. Haider, P. Deminskyi, T. M. Khan, H. Eren, N. Biyikli, *J Phys Chem C* **120**, 26393 (2016).
- ⁸⁹P. C. Lemaire, M. King, G. N. Parsons, *J Chem Phys* **146**, 052811 (2017).
- ⁹⁰A. Marnett, M. J. M. Merkx, B. Karasulu, F. Roozeboom, W. Kessels, A. J. M. Mackus, *ACS Nano* **11**, 9303 (2017).
- ⁹¹E. Stevens, Y. Tomczak, B. T. Chan, E. A. Sanchez, G. N. Parsons, A. Delabie, *Chem Mater* **30**, 3223 (2018).
- ⁹²M. Leskela, M. Ritala, *Angew Chem Int Ed Engl* **42**, 5548 (2003).
- ⁹³R. Chen, H. Kim, P. C. McIntyre, D. W. Porter, S. F. Bent, *Appl Phys Lett* **86**, 191910 (2005).
- ⁹⁴E. Farm, M. Kemell, M. Ritala, M. Leskela, *Chemical Vapor Deposition* **12**, 415 (2006).
- ⁹⁵R. H. Ras, E. Sahramo, J. Malm, J. Raula, M. Karppinen, *J Am Chem Soc* **130**, 11252 (2008).
- ⁹⁶F. S. Minaye Hashemi, C. Prasittichai, S. F. Bent, *ACS Nano* **9**, 8710 (2015).
- ⁹⁷F. S. Minaye Hashemi, B. R. Birchansky, S. F. Bent, *ACS Appl Mater Interfaces* **8**, 33264 (2016).
- ⁹⁸F. S. M. Hashemi, S. F. Bent, *Advanced Materials Interfaces* **3**, 1600464 (2016).
- ⁹⁹R. G. Closser, D. S. Bergsman, L. Ruelas, F. S. M. Hashemi, S. F. Bent, *J Vac Sci Technol A* **35**, 031509 (2017).
- ¹⁰⁰M. H. Heyne, J. F. De Marneffe, A. Delabie, M. Caymax, E. C. Neyts, I. Radu, C. Huyghebaert, S. De Gendt, *Nanotechnology* **28**, 04LT01 (2017).
- ¹⁰¹A. Delabie, M. Caymax, B. Groven, M. Heyne, K. Haesevoets, J. Meersschant, T. Nuytten, H. Bender, T. Conard, P. Verdonck, S. Van Elshocht, S. De Gendt, M. Heyns, K. Barla, I. Radu, A. Thean, *Chem Commun (Camb)* **51**, 15692 (2015).
- ¹⁰²A. Marnett, B. Karasulu, M. A. Verheijen, A. J. M. Mackus, W. M. M. Kessels, F. Roozeboom, *Atomic Layer Deposition Applications 13* **80**, 39 (2017).
- ¹⁰³A. J. M. Mackus, in *Int Sym Vlsi Technol.* (Hsinchu, Taiwan, 2018), pp. 1.
- ¹⁰⁴A. J. M. Mackus, M. J. M. Merkx, W. M. M. Kessels, *Chem Mater* **31**, 2 (2019).
- ¹⁰⁵M. F. J. Vos, S. N. Chopra, M. A. Verheijen, J. G. Ekerdt, S. Agarwal, W. M. M. Kessels, A. J. M. Mackus, *Chem Mater* **31**, 3878 (2019).

- ¹⁰⁶R. Vallat, R. Gassilloud, O. Salicio, K. El Hajjam, G. Molas, B. Pelissier, C. Vallee, *J Vac Sci Technol A* **37**, 020918 (2019).
- ¹⁰⁷S. K. Song, H. Saare, G. N. Parsons, *Chem Mater* **31**, 4793 (2019).
- ¹⁰⁸R. Vallat, R. Gassilloud, B. Eychenne, C. Vallee, *J Vac Sci Technol A* **35**, 01b104 (2017).
- ¹⁰⁹H. B. R. Lee, S. F. Bent, *Nanopatterning by Area-Selective Atomic Layer Deposition*. N. Pinna, M. Knez, Eds., Atomic Layer Deposition of Nanostructured Materials (Blackwell Science Publ, Oxford, 2012), pp. 193.
- ¹¹⁰A. J. Mackus, A. A. Bol, W. M. Kessels, *Nanoscale* **6**, 10941 (2014).
- ¹¹¹K. Ishikawa, K. Karahashi, T. Ichiki, J. P. Chang, S. M. George, W. M. M. Kessels, H. J. Lee, S. Tinck, J. H. Um, K. Kinoshita, *Japanese Journal of Applied Physics* **56**, 06ha02 (2017).
- ¹¹²G. N. Parsons, *J Vac Sci Technol A* **37**, 020911 (2019).
- ¹¹³D. Shamiryan, M. Baklanov, M. Claes, W. Boullart, V. Paraschiv, *Chem Eng Commun* **196**, 1475 (2009).
- ¹¹⁴T. Sasaki, K. Matsuda, M. Omura, I. Sakai, H. Hayashi, *Japanese Journal of Applied Physics* **54**, 06gb03 (2015).
- ¹¹⁵K. Takahashi, K. Ono, *Journal of Vacuum Science & Technology A: Vacuum, Surfaces, and Films* **24**, 437 (2006).
- ¹¹⁶M. Omura, K. Furumoto, K. Matsuda, T. Sasaki, I. Sakai, H. Hayashi, *Plasma Sources Sci T* **26**, 065015 (2017).
- ¹¹⁷M. Schaepkens, I. Martini, E. A. Sanjuan, X. Li, G. S. Oehrlein, W. L. Perry, H. M. Anderson, *Journal of Vacuum Science & Technology A: Vacuum, Surfaces, and Films* **19**, 2946 (2001).
- ¹¹⁸D. Triyoso, R. Liu, D. Roan, M. Ramon, N. V. Edwards, R. Gregory, D. Werho, J. Kulik, G. Tam, E. Irwin, X. D. Wang, L. B. La, C. Hobbs, R. Garcia, J. Baker, B. E. White, P. Tobin, *Journal of the Electrochemical Society* **151**, F220 (2004).
- ¹¹⁹J. A. Murdzek, S. M. George, in *2019 International Symposium on VLSI Technology, Systems and Application (VLSI-TSA)*. (Hsinchu, Taiwan, 2019), pp. 1.
- ¹²⁰B. H. Lee, L. Kang, R. Nieh, W.-J. Qi, J. C. Lee, *Appl Phys Lett* **76**, 1926 (2000).
- ¹²¹J. Chastain, J. F. Moulder, *Handbook of X-ray photoelectron spectroscopy a reference book of standard spectra for identification and interpretation of XPS data*. (Physical Electronics, Inc., Eden Prairie, Minn., ed. [Reprint of the 1992 version], 1995).
- ¹²²D. Barreca, A. Milanov, R. A. Fischer, A. Devi, E. Tondello, *Surface Science Spectra* **14**, 34 (2007).
- ¹²³S. Agraharam, D. W. Hess, P. A. Kohl, S. a. B. Allen, *Journal of Vacuum Science & Technology a-Vacuum Surfaces and Films* **17**, 3265 (1999).
- ¹²⁴N. I. Baklanova, T. M. Zima, A. I. Boronin, S. V. Kosheev, A. T. Titov, N. V. Isaeva, D. V. Graschenkov, S. S. Solntsev, *Surface and Coatings Technology* **201**, 2313 (2006).
- ¹²⁵N. R. Rueger, J. J. Beulens, M. Schaepkens, M. F. Doemling, J. M. Mirza, T. E. F. M. Standaert, G. S. Oehrlein, *Journal of Vacuum Science & Technology a-Vacuum Surfaces and Films* **15**, 1881 (1997).
- ¹²⁶C. J. Powell, A. Jablonski, W. S. M. Werner, W. Smekal, *Appl Surf Sci* **239**, 470 (2005).
- ¹²⁷G. Cunge, J. P. Booth, *Journal of Applied Physics* **85**, 3952 (1999).

- ¹²⁸K. Teii, M. Hori, M. Ito, T. Goto, N. Ishii, *Journal of Vacuum Science & Technology a- Vacuum Surfaces and Films* **18**, 1 (2000).
- ¹²⁹K. Miyata, M. Hori, T. Goto, *Journal of Vacuum Science & Technology A: Vacuum, Surfaces, and Films* **14**, 2343 (1996).
- ¹³⁰T. Goto, *Adv Atom Mol Opt Phy* **44**, 99 (2001).
- ¹³¹X. Li, L. Ling, X. Hua, G. S. Oehrlein, Y. Wang, H. M. Anderson, *Journal of Vacuum Science & Technology A: Vacuum, Surfaces, and Films* **21**, 1955 (2003).
- ¹³²G. A. Hebner, *Journal of Applied Physics* **89**, 900 (2001).
- ¹³³K. Tachibana, M. Nishida, H. Harima, Y. Urano, *J Phys D Appl Phys* **17**, 1727 (1984).
- ¹³⁴L. E. Kline, W. D. Partlow, W. E. Bies, *Journal of Applied Physics* **65**, 70 (1989).
- ¹³⁵H. Kojima, H. Toyoda, H. Sugai, *Appl Phys Lett* **55**, 1292 (1989).
- ¹³⁶H. Sugai, H. Kojima, A. Ishida, H. Toyoda, *Appl Phys Lett* **56**, 2616 (1990).
- ¹³⁷S. Den, T. Kuno, M. Ito, M. Hori, T. Goto, P. O'keeffe, Y. Hayashi, Y. Sakamoto, *Journal of Vacuum Science & Technology A: Vacuum, Surfaces, and Films* **15**, 2880 (1997).
- ¹³⁸J. Robertson, *Surface and Coatings Technology* **50**, 185 (1992).
- ¹³⁹A. Grill, *Diamond and Related Materials* **8**, 428 (1999).
- ¹⁴⁰W. Zhang, A. Tanaka, K. Wazumi, Y. Koga, *Diamond and Related Materials* **11**, 1837 (2002).
- ¹⁴¹N. Fox-Lyon, G. S. Oehrlein, N. Ning, D. B. Graves, *Journal of Applied Physics* **110**, 104314 (2011).
- ¹⁴²N. Fox-Lyon, G. S. Oehrlein, V. Godyak, *Journal of Vacuum Science & Technology A: Vacuum, Surfaces, and Films* **32**, 030601 (2014).
- ¹⁴³K. M. Chang, S. W. Wang, C. H. Li, J. Y. Tsai, T. H. Yeh, *Jpn J Appl Phys I* **35**, 6555 (1996).
- ¹⁴⁴B. Kalanyan, P. C. Lemaire, S. E. Atanasov, M. J. Ritz, G. N. Parsons, *Chem Mater* **28**, 117 (2016).
- ¹⁴⁵A. A. Zinn, in *The Chemistry of Metal CVD*, T. T. Kodas, M. J. Hampden-Smith, Eds. (John Wiley & Sons, New York, NY, 1994), pp. 105.
- ¹⁴⁶A. Rockett, *The Materials Science of Semiconductors*. (Springer, Boston, MA, 2008).
- ¹⁴⁷T. Tatsumi, K.-I. Aketagawa, M. Hiroi, J. Sakai, *Journal of Crystal Growth* **120**, 275 (1992).
- ¹⁴⁸M. R. Goulding, *Materials Science and Engineering: B* **17**, 47 (1993).
- ¹⁴⁹J. T. Jfitch, *Journal of the Electrochemical Society* **141**, 1046 (1994).
- ¹⁵⁰P. A. Oneil, M. C. Ozturk, K. E. Violette, D. Batchelor, K. Christensen, D. M. Maher, *Journal of the Electrochemical Society* **144**, 3309 (1997).
- ¹⁵¹V. M. Donnelly, A. Kornblit, *J Vac Sci Technol A* **31**, 050825 (2013).
- ¹⁵²H. Xiao, *3D IC Devices, Technologies, and Manufacturing*. (SPIE, Bellingham, Washington, USA, 2016).
- ¹⁵³N. Loubet, T. Hook, P. Montanini, C. W. Yeung, S. Kanakasabapathy, M. Guillom, T. Yamashita, J. Zhang, X. Miao, J. Wang, A. Young, R. Chao, M. Kang, Z. Liu, S. Fan, B. Hamieh, S. Sieg, Y. Mignot, W. Xu, S. C. Seo, J. Yoo, S. Mochizuki, M. Sankarapandian, O. Kwon, A. Carr, A. Greene, Y. Park, J. Frougier, R. Galatage, R. Bao, J. Shearer, R. Conti, H. Song, D. Lee, D. Kong, Y. Xu, A. Arceo, Z. Bi, P. Xu, R. Muthinti, J. Li, R. Wong, D. Brown, P. Oldiges, R. Robison, J. Arnold, N. Felix, S. Skordas, J. Gaudiello, T. Standaert, H. Jagannathan, D. Corliss, M. H. Na, A. Knorr, T. Wu, D. Gupta, S. Lian, R. Divakaruni, T. Gow, C. Labelle, S. Lee, V. Paruchuri, H. Bu,

- M. Khare, paper presented at the 2017 Symposium on VLSI Technology, Kyoto, Japan, 5-8 June 2017 2017.
- ¹⁵⁴R. J. Gasvoda, Z. Zhang, E. A. Hudson, S. Agarwal, *J Vac Sci Technol A* **39**, 040401 (2021).
- ¹⁵⁵R. J. Gasvoda, Z. Zhang, S. Wang, E. A. Hudson, S. Agarwal, *J Vac Sci Technol A* **38**, 050803 (2020).
- ¹⁵⁶S. A. Vitale, B. A. Smith, *Journal of Vacuum Science & Technology B: Microelectronics and Nanometer Structures* **21**, 2205 (2003).
- ¹⁵⁷K. Eriguchi, Y. Takao, K. Ono, *Journal of Vacuum Science & Technology A: Vacuum, Surfaces, and Films* **29**, 041303 (2011).
- ¹⁵⁸E. J. C. Tinacba, M. Isobe, S. Hamaguchi, *J Vac Sci Technol A* **39**, 042603 (2021).
- ¹⁵⁹J. J. Végh, D. Nest, D. B. Graves, R. Bruce, S. Engelmann, T. Kwon, R. J. Phaneuf, G. S. Oehrlein, B. K. Long, C. G. Willson, *Journal of Applied Physics* **104**, 034308 (2008).
- ¹⁶⁰D. Nest, T.-Y. Chung, D. B. Graves, S. Engelmann, R. L. Bruce, F. Weirnboeck, G. S. Oehrlein, D. Wang, C. Andes, E. A. Hudson, *Plasma Processes and Polymers* **6**, 649 (2009).
- ¹⁶¹G. S. Oehrlein, R. J. Phaneuf, D. B. Graves, *J Vac Sci Technol B* **29**, 010801 (2011).
- ¹⁶²R. D. Ramsier, J. T. Yates, *Surface Science Reports* **12**, 243 (1991).
- ¹⁶³N. Vanhove, P. Lievens, W. Vandervorst, *Phys Rev B* **79**, 035305 (2009).
- ¹⁶⁴W. F. Van Dorp, in *Materials and Processes for Next Generation Lithography*, A. Robinson, R. Lawson, Eds. (Elsevier Cambridge, MA, 2016), pp. 115.
- ¹⁶⁵J. H. Noh, J. D. Fowlkes, R. Timilsina, M. G. Stanford, B. B. Lewis, P. D. Rack, *ACS Appl Mater Interfaces* **7**, 4179 (2015).
- ¹⁶⁶F. J. Schoenaker, R. Cordoba, R. Fernandez-Pacheco, C. Magen, O. Stephan, C. Zuriaga-Monroy, M. R. Ibarra, J. M. De Teresa, *Nanotechnology* **22**, 265304 (2011).
- ¹⁶⁷T. Bret, B. Afra, R. Becker, T. Hofmann, K. Edinger, T. Liang, P. Hoffmann, *J Vac Sci Technol B* **27**, 2727 (2009).
- ¹⁶⁸C. J. Lobo, A. Martin, M. R. Phillips, M. Toth, *Nanotechnology* **23**, 375302 (2012).
- ¹⁶⁹H. Miyazoe, I. Utke, J. Michler, K. Terashima, *Appl Phys Lett* **92**, 043124 (2008).
- ¹⁷⁰M. G. Lassiter, T. Liang, P. D. Rack, *J Vac Sci Technol B* **26**, 963 (2008).
- ¹⁷¹M. M. Shawrav, Z. G. Gokdeniz, H. D. Wanzenboeck, P. Taus, J. K. Mika, S. Waid, E. Bertagnolli, *Materials Science in Semiconductor Processing* **42**, 170 (2016).
- ¹⁷²P. Roediger, M. Mijic, C. Zeiner, A. Lugstein, H. D. Wanzenboeck, E. Bertagnolli, *J Vac Sci Technol B* **29**, 06FB03 (2011).
- ¹⁷³P. Roediger, G. Hochleitner, E. Bertagnolli, H. D. Wanzenboeck, W. Buehler, *Nanotechnology* **21**, 285306 (2010).
- ¹⁷⁴N. Vanhove, P. Lievens, W. Vandervorst, *J Vac Sci Technol B* **28**, 1206 (2010).
- ¹⁷⁵S. Matsui, K. Mori, *Appl Phys Lett* **51**, 1498 (1987).
- ¹⁷⁶S. Matsui, H. Watanabe, *Appl Phys Lett* **59**, 2284 (1991).
- ¹⁷⁷S. M. Ivo Utke, Phillip Russell, *Nanofabrication Using Focused Ion and Electron Beams*. (Oxford University Press, United Kingdom, 2012).
- ¹⁷⁸O. Ingólfsson, *Low-Energy Electrons: Fundamentals and Applications*. (Jenny Stanford Publishing, Boca Raton, 2019).
- ¹⁷⁹R. Hippler, J. Kredl, V. Vartolomei, *Vacuum* **83**, 732 (2008).

- ¹⁸⁰C. Li, V. Godyak, T. Hofmann, K. Edinger, G. S. Oehrlein, *J Vac Sci Technol A* **38**, 033001 (2020).
- ¹⁸¹C. Li, T. Hofmann, K. Edinger, V. Godyak, G. S. Oehrlein, *J Vac Sci Technol B* **38**, 032208 (2020).
- ¹⁸²J. J. Beulens, B. E. E. Kastenmeier, P. J. Matsuo, G. S. Oehrlein, *Appl Phys Lett* **66**, 2634 (1995).
- ¹⁸³B. E. E. Kastenmeier, P. J. Matsuo, J. J. Beulens, G. S. Oehrlein, *Journal of Vacuum Science & Technology A: Vacuum, Surfaces, and Films* **14**, 2802 (1996).
- ¹⁸⁴G. S. Oehrlein, P. J. Matsuo, M. F. Doemling, N. R. Rueger, B. E. E. Kastenmeier, M. Schaepkens, T. Standaert, J. J. Beulens, *Plasma Sources Sci T* **5**, 193 (1996).
- ¹⁸⁵P. J. Matsuo, B. E. E. Kastenmeier, J. J. Beulens, G. S. Oehrlein, *Journal of Vacuum Science & Technology A: Vacuum, Surfaces, and Films* **15**, 1801 (1997).
- ¹⁸⁶J. W. John F. Watts, in *An Introduction to Surface Analysis by XPS and AES*. (John Wiley & Sons, West Sussex, England, 2005).
- ¹⁸⁷C. J. Mogab, A. C. Adams, D. L. Flamm, *Journal of Applied Physics* **49**, 3796 (1978).
- ¹⁸⁸D. L. Flamm, V. M. Donnelly, J. A. Mucha, *Journal of Applied Physics* **52**, 3633 (1981).
- ¹⁸⁹Y. H. Lee, M. M. Chen, *Journal of Applied Physics* **54**, 5966 (1983).
- ¹⁹⁰D. Humbird, D. B. Graves, *Journal of Applied Physics* **96**, 791 (2004).
- ¹⁹¹P. Arora, T. Nguyen, A. Chawla, S.-K. Nam, V. M. Donnelly, *J Vac Sci Technol A* **37**, 061303 (2019).
- ¹⁹²M. G. Lassiter, P. D. Rack, *Nanotechnology* **19**, 455306 (2008).
- ¹⁹³E. Bohler, J. Warneke, P. Swiderek, *Chem Soc Rev* **42**, 9219 (2013).
- ¹⁹⁴L. G. Christophorou, J. K. Olthoff, M. V. V. S. Rao, *Journal of Physical and Chemical Reference Data* **25**, 1341 (1996).
- ¹⁹⁵L. G. Christophorou, J. K. Olthoff, *Journal of Physical and Chemical Reference Data* **28**, 967 (1999).
- ¹⁹⁶L. G. Christophorou, J. K. Olthoff, *Appl Surf Sci* **192**, 309 (2002).
- ¹⁹⁷J. W. Mcconkey, C. P. Malone, P. V. Johnson, C. Winstead, V. Mckoy, I. Kanik, *Physics Reports* **466**, 1 (2008).
- ¹⁹⁸S. Muhl, A. Pérez, *Thin Solid Films* **579**, 174 (2015).
- ¹⁹⁹K. Sasaki, Y. Kawai, K. Kadota, *Review of Scientific Instruments* **70**, 76 (1999).
- ²⁰⁰N. S. J. Braithwaite, *Plasma Sources Sci T* **9**, 517 (2000).
- ²⁰¹H. Singh, J. W. Coburn, D. B. Graves, *Journal of Vacuum Science & Technology A: Vacuum, Surfaces, and Films* **19**, 718 (2001).
- ²⁰²I. Chun, A. Efremov, G. Y. Yeom, K.-H. Kwon, *Thin Solid Films* **579**, 136 (2015).
- ²⁰³D. J. Oostra, A. E. De Vries, *Nuclear Instruments and Methods in Physics Research Section B: Beam Interactions with Materials and Atoms* **18**, 618 (1986).
- ²⁰⁴K.-Y. Lin, C. Li, S. Engelmann, R. L. Bruce, E. A. Joseph, D. Metzler, G. S. Oehrlein, *J Vac Sci Technol A* **38**, 032601 (2020).
- ²⁰⁵A. C. Adams, F. B. Alexander, C. D. Capio, T. E. Smith, *Journal of The Electrochemical Society* **128**, 1545 (1981).
- ²⁰⁶D. Metzler, F. Weilnboeck, S. Engelmann, R. L. Bruce, G. S. Oehrlein, *J Vac Sci Technol B* **34**, 041604 (2016).

- ²⁰⁷G. S. Oehrlein, J. F. Rembetski, *Ibm Journal of Research and Development* **36**, 140 (1992).
- ²⁰⁸A. Ermolieff, S. Marthon, F. Bertin, F. Pierre, J. F. Daviet, L. Peccoud, *Journal of Vacuum Science & Technology A: Vacuum, Surfaces, and Films* **9**, 2900 (1991).
- ²⁰⁹O. Joubert, G. Cunge, B. Pelissier, L. Vallier, M. Kogelschatz, E. Pargon, *Journal of Vacuum Science & Technology A: Vacuum, Surfaces, and Films* **22**, 553 (2004).
- ²¹⁰G. Cunge, B. Pelissier, O. Joubert, R. Ramos, C. Maurice, *Plasma Sources Science and Technology* **14**, 599 (2005).
- ²¹¹K. Y. Lin, C. Preischl, C. F. Hermanns, D. Rhinow, H.-M. Solowan, T. Hofmann, B. Michael, K. Edinger, G. S. Oehrlein, *SiO₂ Surface Evolution under CF₄/O₂ Remote Plasma and Co-Introduction of Remote Plasma and Electron Beam*, Manuscript in preparation.
- ²¹²H. Abe, M. Yoneda, N. Fujlwara, *Japanese Journal of Applied Physics* **47**, 1435 (2008).
- ²¹³K. Shinoda, N. Miyoshi, H. Kobayashi, M. Izawa, T. Saeki, K. Ishikawa, M. Hori, *J Vac Sci Technol A* **37**, 051002 (2019).
- ²¹⁴N. Miyoshi, K. Shinoda, H. Kobayashi, M. Kurihara, Y. Kouzuma, M. Izawa, *J Vac Sci Technol A* **39**, 052601 (2021).
- ²¹⁵N. Miyoshi, H. Kobayashi, K. Shinoda, M. Kurihara, K. Kawamura, Y. Kouzuma, M. Izawa, *J Vac Sci Technol A* **40**, 012601 (2022).